

South Dakota State University

Open PRAIRIE: Open Public Research Access Institutional Repository and Information Exchange

Electronic Theses and Dissertations

2020

Optimization-based Fast-frequency Support in Low Inertia Power Systems

Ujjwol Tamrakar
South Dakota State University

Follow this and additional works at: <https://openprairie.sdstate.edu/etd>



Part of the [Power and Energy Commons](#)

Recommended Citation

Tamrakar, Ujjwol, "Optimization-based Fast-frequency Support in Low Inertia Power Systems" (2020). *Electronic Theses and Dissertations*. 3754.
<https://openprairie.sdstate.edu/etd/3754>

This Dissertation - Open Access is brought to you for free and open access by Open PRAIRIE: Open Public Research Access Institutional Repository and Information Exchange. It has been accepted for inclusion in Electronic Theses and Dissertations by an authorized administrator of Open PRAIRIE: Open Public Research Access Institutional Repository and Information Exchange. For more information, please contact michael.biondo@sdstate.edu.

OPTIMIZATION-BASED FAST-FREQUENCY SUPPORT IN LOW INERTIA POWER
SYSTEMS

BY

UJJWOL TAMRAKAR

A dissertation submitted in partial fulfillment of the requirements for the

Doctor of Philosophy

Major in Electrical Engineering

South Dakota State University

2020

DISSERTATION ACCEPTANCE PAGE

Ujjwol Tamrakar

This dissertation is approved as a creditable and independent investigation by a candidate for the Doctor of Philosophy degree and is acceptable for meeting the dissertation requirements for this degree. Acceptance of this does not imply that the conclusions reached by the candidate are necessarily the conclusions of the major department.

Reinaldo Tonkoski

Advisor

Date

George Hamer

Department Head

Date

Dean, Graduate School

Date

ACKNOWLEDGEMENTS

I would like to express my sincere gratitude towards my research advisor Dr. Reinaldo Tonkoski for his guidance and valuable insights during my Ph.D. Without his guidance and persistent help, this dissertation would not have been possible. I would also like to thank all the committee members, Drs. Timothy M. Hansen, Marco Ciarca, David A. Copp, Tu Nguyen and the graduate faculty representative Dr. Anthony Durr for their active participation and interest in my work. I am especially thankful to Dr. David A. Copp for conceptualizing this work and all the valuable feedback which elevated the quality of this work. I am also thankful to Dr. David Galipeau who has been a mentor and essential influence in my career.

During my Ph.D., I have been fortunate to have the support of all my peers and colleagues in the Electrical Engineering and Computer Science Department. I am especially grateful to Abhilasha Bajracharya, Andre Luna, Dipesh Shrestha, Prajina Tandukar, Manisha Maharjan, Fernando Bereta dos Reis, and Jyotshna Pokharel. I would also like to thank Dan Flaskey for all the help in setting up lab experiments throughout my Ph.D. program.

I am thankful for my wife, Jharna Pokhrel, who stayed by my side with words of patience and encouragement through every step of this journey. I would like to thank my father Dr. Indraman Tamrakar who has guided me to achieve my professional and personal goals. I am also thankful to my mother, Pabitra Tamrakar, and my sister, Elisha Tamrakar, for their unconditional love, motivation, and support.

The research in this dissertation was supported by the South Dakota Board of

Regents (SDBoR) Ph.D. funds, the National Science Foundation under grant number MRI-1726964 and U.S. Department of Energy under grant number DE-SC0020281. I am thankful to Sandia National Laboratories (SNL) and the U.S. Department of Energy's Energy Storage Program for hosting me as an intern during my Ph.D. I am grateful to Dr. Ray Byrne and Dr. Babu Chalamala for their help at SNL for completing this work.

CONTENTS

ABBREVIATIONS	ix
LIST OF FIGURES	xi
ABSTRACT	xv
CHAPTER 1 INTRODUCTION	1
1.1 Multi-timescale Frequency Control in Power Systems	2
1.2 Recent Trends and Frequency Events Due to Low Inertia	4
1.3 Frequency Limits in Low Inertia Power Systems	6
1.4 Energy Storage Systems for Fast-Frequency Support	8
1.5 Motivation and Objectives	9
1.6 Dissertation Outline and Contributions	10
CHAPTER 2 CONCEPTS OF VIRTUAL INERTIA AND CLASSIFICATION	12
2.1 Chapter Objectives and Contributions	13
2.2 First Generation of Virtual Inertia Systems	13
2.2.1 Synchronverters: A Synchronous Generator Model-based Topology	15
2.2.2 Ise Lab's Topology: A Swing Equation-based Topology	18
2.2.3 Virtual Synchronous Generators: A Frequency-Power Response- based Topology	19
2.2.4 Droop-based Approaches	22
2.3 Other Topologies	25

2.3.1	Summary of Topologies	27
2.4	Design Procedures and Simulation Results	29
2.4.1	Design of synchronverter topology	30
2.4.2	Design of Ise Lab's topology	32
2.4.3	Design of virtual synchronous generator topology	34
2.4.4	Summary of Simulations Results	36
2.5	Second Generation: Optimization of Virtual Inertia Systems	37
2.5.1	Second Generation of Synchronverters	38
2.5.2	Second Generation of Ise Lab's Topology	38
2.5.3	Second Generation of Virtual Inertia Systems	39
2.6	Third Generation of Virtual Inertia Systems	43
2.7	Chapter Conclusions	44
CHAPTER 3 INERTIA AND DAMPING CONSTANT ESTIMATION BASED ON		
MOVING HORIZON ESTIMATOR		46
3.1	Previous Work on Inertia Estimation	47
3.2	Chapter Objectives and Contributions	48
3.3	Modeling of Microgrid Frequency Dynamics	49
3.3.1	Frequency Event Characterization	50
3.3.2	Inertia and Damping Constant	51
3.3.3	Modeling of the Frequency Control Loops	52
3.4	Moving Horizon Estimation and Problem Formulation	54
3.4.1	Concepts of Moving Horizon Estimation	55

3.4.2	Formulation of Moving Horizon Estimator	56
3.4.3	Implementation of Moving Horizon Inertia Estimator	58
3.5	Simulation Setup	59
3.5.1	Simulation Benchmark	59
3.5.2	Setup for the MHE using ACADO	62
3.6	Results and Analysis	63
3.6.1	Estimation with Gaussian Noisy Measurements from PLL	66
3.6.2	Effect of Estimation Time Horizon on Parameter Estimates	67
3.6.3	Estimation with Non-Gaussian Noisy Measurements from PLL	68
3.7	Chapter Conclusions	71
CHAPTER 4 OPTIMIZATION-BASED FAST-FREQUENCY ESTIMATION AND SUPPORT OF LOW INERTIA MICROGRIDS		72
4.1	Previous Work on Optimal Fast-Frequency Support Strategies	72
4.2	Chapter Objectives and Contributions	74
4.3	Proposed MHE-MPC Framework	75
4.3.1	Formulation of Moving Horizon Estimation	77
4.3.2	Formulation of Model Predictive Control	78
4.4	Simulation Setup	79
4.4.1	Benchmark	79
4.4.2	Configuration for the MHE-MPC Framework	81
4.5	Results and Analysis	82
4.5.1	Performance of the MHE	83

- 4.5.2 Performance: Operational Flexibility 84
- 4.5.3 Performance: Constraints Handling 88
- 4.5.4 Performance: Stability Improvement 90
- 4.6 Computational Tractability 93
- 4.7 Chapter Conclusions 94

- CHAPTER 5 CONCLUSIONS AND FUTURE WORK 95
- 5.1 Conclusions 95
- 5.2 Future Work 98

- REFERENCES 100

- LIST OF PUBLICATIONS DURING PH.D. 114

ABBREVIATIONS

ADP	Adaptive Dynamic Programming
AGC	Automatic Generation Control
DER	Distributed Energy Resource
ENTSO-E	European Network of Transmission System Operators for Electricity
ERCOT	Electric Reliability Council of Texas
ESS	Energy Storage System
FERC	Federal Energy Regulatory Commission
IEPE	Institute of Electrical Power Engineering
ISO	Independent System Operator
KHI	Kawasaki Heavy Industries
LPF	Low-Pass Filter
LQR	Linear Quadratic Regulator
MHE	Moving Horizon Estimation
MPC	Model Predictive Control
MPP	Maximum Power Point
NERC	North American Electric Reliability Corporation
PDF	Probability Density Function
PI	Proportional-Integral
PLL	Phase Locked Loop
PMU	Phasor Measurement Unit

PV	Photo-Voltaic
PWM	Pulse Width Modulator
QoS	Quality of Service
RES	Renewable Energy Sources
ROCOF	Rate of Change of Frequency
SG	Synchronous Generator
SNR	Signal-to-Noise-Ratio
SPC	Synchronous Power Controllers
STATCOM	Synchronous Compensator
UFLS	Under Frequency Load Shedding
VISMA	Virtual Synchronous Machine
VOC	Virtual Oscillator Controller
VSG	Virtual Synchronous Generators
ZOH	Zero Order Hold

LIST OF FIGURES

Figure 1.1.	Evolution towards an inverter-dominated power system.	2
Figure 1.2.	Multi-timescale frequency control in power systems.	3
Figure 1.3.	Increase in frequency changes in ERCOT connection due to generation loss.	5
Figure 1.4.	Frequency standards for microgrid systems [21], [22], [27].	8
Figure 1.5.	Grid ancillary service from ESSs.	9
Figure 2.1.	Concept of virtual inertia.	12
Figure 2.2.	Classification of different topologies used for virtual inertia implemen- tation.	14
Figure 2.3.	Synchronverter Topology: (a) Overall schematic showing operating principle. (b) Detailed control diagram showing the modeling equations.	17
Figure 2.4.	Ise Lab's Topology: (a) Overall schematic showing operating princi- ple. (b)The governor model to compute input power.	19
Figure 2.5.	Virtual synchronous generator topology.	20
Figure 2.6.	Schematic for frequency droop control.	23
Figure 2.7.	Schematic diagram of the virtual inertia simulation benchmark.	30
Figure 2.8.	Simulation results from a Synchronverter: (a) System frequency after a step-increase of 2 kW load. (b) ROCOF after a step-increase of 2 kW load. (c) Increase in inverter power in response to system frequency decrease.	32

Figure 2.9.	Simulation results from ISE lab’s topology: (a) System frequency after a step-increase of 2 kW load. (b) ROCOF after a step-increase of 2 kW load. (c) Increase in inverter power as a response to system frequency decrease.	33
Figure 2.10.	Simulation results from a Virtual Synchronous Generator: (a) System frequency after a step-increase of 2 kW load. (b) ROCOF after a step-increase of 2 kW load. (c) Increase in inverter power as a response to system frequency decrease.	35
Figure 2.11.	Modified Virtual Synchronous Generator using Adaptive Dynamic Programming (a) Overall schematic of the controller. (b) The action and critic neural network-based structure.	41
Figure 2.12.	Comparison of traditional VSG controller with the online learning based controller: (a) Frequency of the system for step load changes. (b) Power exchange with the system [24].	42
Figure 2.13.	Generations of virtual inertia systems.	44
Figure 3.1.	Characterization of power system frequency after an event.	51
Figure 3.2.	Block diagram of the isolated power system.	53
Figure 3.3.	Basic concept of moving horizon estimation.	56
Figure 3.4.	Flowchart representing the procedures for online moving horizon estimation with ACADO Toolbox.	59
Figure 3.5.	Simulation setup used in MATLAB/Simulink. The moving horizon estimator is implemented using ACADO Toolkit.	60

Figure 3.6.	A snapshot of the excitation signals used to perturb the system frequency along with corresponding changes in frequency and ROCOF. The inertia constant of the system is assumed to change from 10 s to 5 s at a simulation time of 25 s.	61
Figure 3.7.	Inertia constant and damping constant estimate along with the true values for different levels of measurement noise. The noise distribution is assumed to be Gaussian.	65
Figure 3.8.	Improvement in inertia constant and damping constant estimate along with an increase in the prediction horizon.	68
Figure 3.9.	Estimates with a non-Gaussian distribution (Mean = 0, Co-variance=1e-7, Skewness = +1, Kurtosis = 7. (a) The pdf of the measurement noise. (b) Inertia constant estimate. (c) Damping constant estimate.	70
Figure 3.10.	Estimates with a non-Gaussian distribution (Mean = 0, Co-variance=1e-7, Skewness = -1, Kurtosis = 7. (a) The pdf of the measurement noise. (b) Inertia constant estimate. (c) Damping constant estimate.	70
Figure 4.1.	Proposed MHE-MPC framework for fast-frequency support. The MHE provides state estimates for the frequency and ROCOF from noisy PLL measurements while the MPC provides ESS control signals to provide fast-frequency support.	76
Figure 4.2.	Modified test system of Cordova, Alaska.	81
Figure 4.3.	Frequency and ROCOF of the microgrid system estimated using the MHE. The estimates are compared against the noisy PLL measurements and the measurement from LPFs.	83

Figure 4.4.	Heatmaps illustrating the variation of different system parameters based on the selection of Q_{11} and Q_{22} . (a) Maximum frequency change. (b) Maximum ROCOF. (c) Peak power output from ESS.	85
Figure 4.5.	Frequency, ROCOF, and peak power output of ESS for different values of Q . (a) Change in system frequency. (b) System ROCOF. (c) Power output from ESS.	86
Figure 4.6.	Frequency, ROCOF, and peak power output of ESS for different values of R . (a) Change in system frequency. (b) System ROCOF. (c) Power output from ESS.	87
Figure 4.7.	Comparison of constrained versus unconstrained system operation. The peak-power output is constrained to 0.1 p.u. in this case.	89
Figure 4.8.	Simulation setups to analyze the advantage of the MHE module. (a) MPC with measurements from PLL with LPF. (b) Proposed combined MHE-MPC. (c) Traditional virtual-inertia controller with measurements from PLL with LPF.	91
Figure 4.9.	Frequency, ROCOF and peak power output of ESS with and without the MHE module for the same weighting parameters.	91
Figure 4.10.	Frequency, ROCOF and peak power output of ESS when using a traditional virtual inertia controller versus the proposed MHE-MPC framework.	92

ABSTRACT

OPTIMIZATION-BASED FAST-FREQUENCY SUPPORT IN LOW INERTIA POWER
SYSTEMS

UJJWOL TAMRAKAR

2020

The future electrical energy demand will largely be met by non-synchronous renewable energy sources (RESs) in the form of photovoltaics and wind energy. The lack of inertial response from these non-synchronous, inverter-based generation in microgrids makes the system vulnerable to large rate-of-change-of-frequency (ROCOF) and frequency excursions. This can trigger under frequency load shedding and cause cascaded outages which may ultimately lead to total blackouts. To limit the ROCOF and the frequency excursions, fast-frequency support can be provided through appropriate control of energy storage systems (ESSs). For proper deployment of such fast-frequency control strategies, accurate information regarding the inertial response of the microgrid is required.

In this dissertation, a moving horizon estimation (MHE)-based approach is first proposed for online estimation of inertia and damping constants of a low-inertia microgrid. The MHE also provides real estimates of the noisy frequency and ROCOF measurements. The estimates are employed by a model predictive control (MPC) algorithm that computes control actions to provide fast-frequency support by solving a finite-horizon, online optimization problem. The combined MHE-MPC framework allows an ESS operator to provide near-optimal *fast-frequency support as a service*. The framework maintains the

desired quality-of-service (limiting the ROCOF and frequency) while taking into account the ESS lifetime and physical limits. Additionally, this approach avoids oscillatory behavior induced by delays that are common when using low pass filter and traditional derivative-based (virtual inertia) controllers with high gains. Through simulation results, it has been shown that the proposed framework can provide near-optimal fast-frequency support while incorporating the physical limits of the ESS. The MHE estimator provides accurate state and parameter estimates that help in improving the dynamic performance of the controller compared to traditional derivative-based controllers. Furthermore, the flexibility of the proposed approach to achieve desired system dynamics based on the desired *quality-of-service* has also been demonstrated.

CHAPTER 1 INTRODUCTION

The demand for clean energy in the modern power system is on the rise, driven by factors such as fuel prices, grid codes, laws, and regulations. Renewable energy sources (RESs) like photovoltaic (PV) and wind energy are now gradually starting to dominate the energy generation mix, replacing traditional generation sources, such as coal and nuclear [1]. The popularity of distributed PV plants further escalates the penetration of renewables in the modern power system. The global installation of wind and PV generation exceeded 400 GW and 200 GW, respectively, by the end of 2015 [2]. Countries like Ireland and Germany already have annual RES penetrations of more than 20% [3]. In Denmark, wind power alone can meet 40% of the country's instantaneous electricity demand, which is the highest among all countries. The rapid development of RES is causing the modern power grid to gravitate towards an inverter-dominated system from a rotational generator-dominated system, as illustrated in Figure 1.1. PV systems and most modern wind turbines are interfaced through inverters. Although this is advantageous from the point-of-view of harvesting RES, the inverter-based generation does not provide any mechanical inertial response and hence compromises frequency stability [3]–[5].

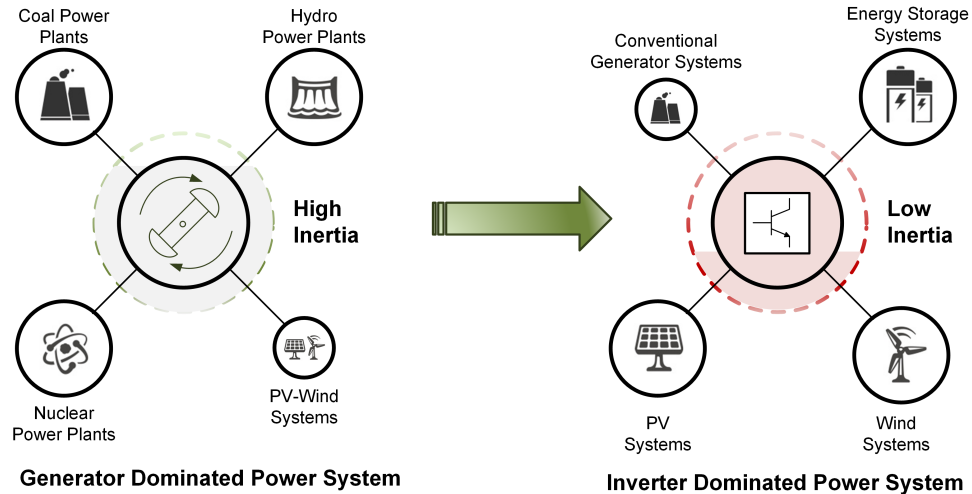


Figure 1.1. Evolution towards an inverter-dominated power system.

1.1 Multi-timescale Frequency Control in Power Systems

To maintain the power generation and load balance, various control actions are implemented in a power system over multiple time-frames as illustrated in Figure 1.2. The governor response is the primary control action which takes place within the first few seconds (typically 1–30 s) of a frequency event and aims at reducing the frequency deviation. The automatic generation control (AGC) is the secondary control action that takes place within minutes (typically 1–30 minutes) and restores the system frequency to the nominal value. The tertiary control action is the reserve deployment when actions are taken to get the resources in place to handle present or future disturbances in the system. Whenever there is an imbalance between the generation and consumption in a power system, the generators cannot respond instantaneously to balance the system. The kinetic energy stored in the rotors is responsible for counteracting this imbalance through inertial response until the primary frequency control has been activated.

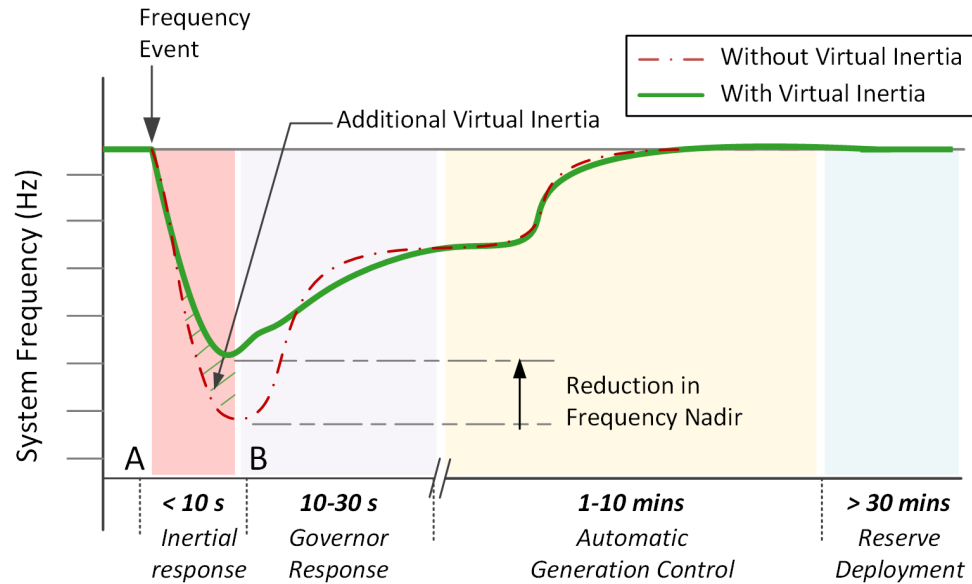


Figure 1.2. Multi-timescale frequency control in power systems.

As conventional generators are displaced by RES, the inertial response also decreases. This leads to an increased rate-of-change-of-frequency (ROCOF), and a low-frequency nadir (minimum frequency point) in a very short time. The primary frequency control cannot respond within the small time frame (typically less than 10 s) to arrest the system frequency change. This period is highlighted as section AB in Figure 1.2. It is clear from the figure that in systems with lower inertia, the frequency nadir is considerably lower along with a high ROCOF. Such situations can lead to tripping of frequency relays (causing under-frequency load shedding (UFLS)) and, in the worst case, may lead to cascaded outages [6], [7]. The solution to such scenarios is to provide fast-frequency support through *virtual inertia* in the system. The basic requirements of a virtual inertia system are that it has to operate in a very short time interval (typically less than 10 s) and in an autonomous fashion. Deployed appropriately, virtual inertia systems would enhance system stability and enable greater penetration of RESs.

1.2 Recent Trends and Frequency Events Due to Low Inertia

Recent reports and studies have shown frequency stability to be a matter of significant concern due to the lack of inertial response from RESs. The independent system operator (ISO), Electricity of Reliability Council of Texas (ERCOT) has reported a continuous decline in the inertial response of its system and recommends additional inertial response [8], [9]. Figure 1.3 illustrates the change in frequency in the ERCOT interconnection for two time periods for the same amount of generation loss. The change in frequency per generation loss is increasing yearly, and this trend is highly correlated with the increased RES penetration over the same time period. ERCOT has also implemented an inertia monitoring and forecasting tool to manage inertia in the ERCOT system. The tool uses the inertia parameter of each synchronous generator and its ON/OFF status to estimate the current inertia in the ERCOT system [10]. This allows the ERCOT's system operators to plan and procure fast-frequency services. Similarly, the European Network of Transmission System Operators for Electricity (ENTSO-E) has reported increased frequency violations in the Nordic grid correlated with increased RES penetration [11]. As a consequence, the inertial response from wind turbines is now mandatory in many countries [12], [13] and the trend is extending towards PV plants as well.

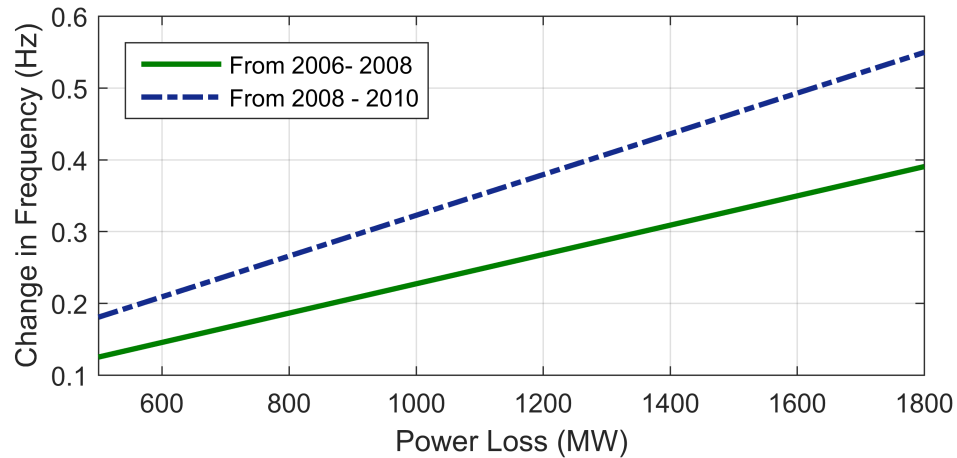


Figure 1.3. Increase in frequency changes in ERCOT connection due to generation loss.

Recently, there have been several power system outages that have been reported due to frequency events in the power system. For example, on August 9th, 2019 a power outage in Great Britain affected around 1 million people for 15 -45 minutes [14]. Two subsequent large generation losses caused the frequency of the system to dip below the UFLS setting of 48.8 Hz. This led to the shedding of critical infrastructures such as rail-transit systems and hospitals. The non-synchronous generation at the time of the event was around 50%. Reports concluded that the lack of inertial response to the frequency event was the main cause of the outage and the Great Britain power system did not have enough fast-frequency services procured. Similarly, in September 2018 there was a major power outage in Southern Australia which affected around 850,000 people. In this case, multiple wind-farms tripped due to severe storm resulting in loss of more than 450 MW in less than 7 s. The frequency of the system thus plummeted in absence of fast-frequency support which led to a cascaded outage in the system [15]. Thus there is a strong practical relevance to research on fast-frequency support mechanisms through virtual inertia systems which were academic in the past.

1.3 Frequency Limits in Low Inertia Power Systems

Microgrids have been identified as the best option to integrate RESs in terms of flexibility and reliability [16]–[18]. The microgrids can be operated in three possible modes: grid-connected, islanded or isolated. A microgrid is said to have been islanded when a microgrid that is grid-connected disconnects from the grid, either in a planned fashion or due to a fault/disturbance in the main grid. In the isolated mode of operation, the microgrid is designed such that it is never connected to the grid. Regardless, these microgrid systems represent weak power systems and the high penetration of inertia-less PV and wind energy systems has a severe effect on the frequency stability [19]. The rapid changes in the generation can cause frequency variations in the system that are outside standard limits and compromise the stability of the system.

Figure 1.4 shows the recommended standard frequency range for grid-connected and isolated/islanded microgrids. In the grid-connected mode, the frequency is controlled by the main grid and the frequency deviations are relatively small. However, this scenario is slowly changing with increased integration of large-scale inertia-less generation. IEEE recommends a tight frequency operating standard of $\pm 0.036\text{Hz}$ for grid-connected systems. The North American Reliability Corporation (NERC) recommends triggering the first level of UFLS when the system frequency drops below 59.3 Hz (for a nominal frequency of 60 Hz for the US power grid). The activation of UFLS is the last automated reliability measure to counteract frequency drop and re-balance the system [20]. NERC recommended control actions that include disconnecting the generator if the frequency drops below 57 Hz or rises above 61.8 Hz [21]. The European Norm EN50160 also

imposes similar tight ranges for grid-connected microgrid systems. There are no specific standards defined for frequency limits for isolated microgrid systems. This is highly dependent on the generation and the load mix in a particular microgrid system. From a generator point-of-view, frequency standards like the ISO 8528-5 standard [22] can provide a guideline for the frequency limits. With the small amount of SG in isolated microgrids, the frequency excursions and ROCOF are greater and the need for virtual inertia is of high importance. In such isolated microgrids, to implement virtual inertia either dedicated energy storage systems (ESS) can be used [23], [24], or inertia can be emulated by operating PV/wind below their maximum power point (MPP) [25], [26]. However, the allowable frequency nadirs and ROCOFs in the microgrids in islanded/isolated conditions may be relaxed compared to grid-connected operation. This will be especially vital for the design of virtual inertia systems for isolated microgrids as these microgrids often have limited energy resources and relaxing the frequency operating region would result in significant energy savings, lower ESS lifetime degradation, and reduction in power ratings of power electronic systems.

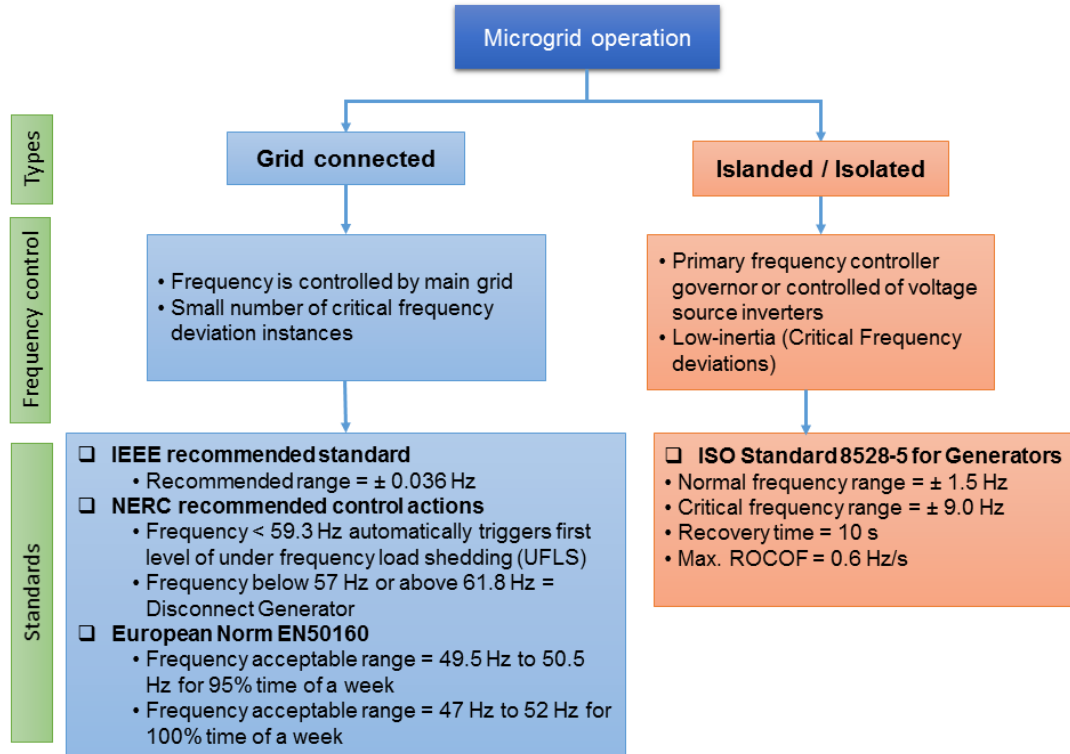


Figure 1.4. Frequency standards for microgrid systems [21], [22], [27].

1.4 Energy Storage Systems for Fast-Frequency Support

Numerous ancillary services can be provided to the grid through ESSs. Figure 1.5 summarizes the major services showing the power range and the time-scale of the service. Frequency regulation, load leveling, and energy arbitrage are some of the main applications. Apart from this, other applications such as RES forming, RES following and volt/var support have also been discussed in the literature [28]. In the shorter time-scale applications like fast-frequency support through virtual inertia, frequency/watt function and frequency regulation the high rate of power exchange in short intervals (high ramp-rates) will have a higher impact on the ESS lifetime [29]. Similarly, when ESSs are used for a longer-scale application like load leveling and/or arbitrage the

depth-of-discharge or overcharging may have a more significant impact on the ESS lifetime rather than the ramp-rates [30]. To maintain power quality in the present scenario, the Federal Energy Regulatory Commission (FERC) issues different orders such as the FERC Order No. 755, 784 and 890 which allow ESS participation in ancillary services. Such mandates allow for a market structure that compensates these fast-frequency services. The participation of ESSs in such services, however, imparts large stresses on the storage medium due to high charging/discharging currents, which can degrade both the power and capacity of ESSs over their lifetime.

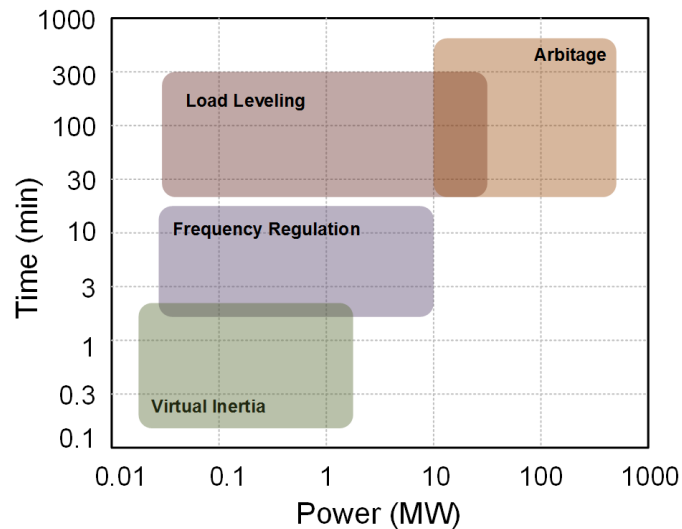


Figure 1.5. Grid ancillary service from ESSs.

1.5 Motivation and Objectives

Fast-frequency support is a power-intensive service and can result in large power demands and ramp-rates from the energy medium, which can have a substantial negative impact on the ESS lifetime [29]. The ESS operator needs to provide frequency support to minimize the ROCOF and the frequency deviation while minimizing the impact on the ESS. Furthermore, there are ESS physical constraints to be considered, such as limits on

peak power and/or ramp-rates. This motivates the need to design a framework for an ESS operator to be able to dispatch the ESS unit based on the desired frequency *quality-of-service* (QoS) required in the microgrid (reduction in ROCOF and frequency deviation) and the incentives required to provide the QoS for such a frequency-as-a-service in the market.

The objective of this dissertation is to develop a near-optimal fast-frequency support framework for low-inertia microgrids through the use of ESSs. The developed framework should be:

- *Flexible* to change performance based on resources available to the ESS operator and the desired level QoS.
- *Able to incorporate physical constraints* of the ESS such as peak-power limits and ramp-rate limits.
- *Adaptable* to change in system inertia and damping constants.

1.6 Dissertation Outline and Contributions

The dissertation is divided into three major chapters. **Chapter 2** introduces the basic concepts of fast-frequency support and virtual inertia. A brief review of existing trends and techniques in emulating virtual inertia and fast-frequency support is presented. This is followed by a detailed comparison between the different techniques and a method to achieve similar dynamic performance from the described techniques using common time-constants is proposed. **Chapter 3** introduces a novel mechanism for online estimation of the inertia and damping constant of a microgrid system using local measurements. The inertia of the system can change based on the number of synchronous

generators that are online which in turn depends on renewable energy penetration. Thus an estimate of the inertia constant of the system will allow for improved control strategy and protection schemes. Finally, in **Chapter 4** a model predictive fast-frequency support mechanism combined with a moving horizon estimation is presented. The model predictive control performs near-optimal control actions based on a defined cost-function. The conclusions of the dissertation are summarized in **Chapter 5**.

The main contributions of this dissertation are as follows:

- Reviewed and compared existing techniques and trends for virtual inertia and fast-frequency support.
- Developed a moving horizon estimation (MHE) based approach for online estimation of inertia and damping constant of a microgrid system using local measurements from a phase-locked-loop (PLL).
- Developed a model predictive control (MPC) approach to provide near-optimal fast-frequency support. The mechanism provides flexibility to control the frequency dynamics as desired and incorporate the physical constraints of the system within the control formulation.

This dissertation provides a summary of the research performed during the Ph.D. program. A listing of all the publications during the Ph.D. program is presented at the end of this dissertation.

CHAPTER 2 CONCEPTS OF VIRTUAL INERTIA AND CLASSIFICATION

Virtual inertia is a combination of control algorithms, RESs, ESSs, and power electronics that emulates the inertia of a conventional power system. The concept of virtual inertia is summarized in Figure 2.1. The core of the system is the virtual inertia algorithm that presents the various energy sources interfaced to the grid through power electronics converters as synchronous generators. Most modern wind turbines are operated as variable speed wind turbines and interfaced through back-to-back converters, completely decoupling the inertia from the grid. Similarly, PV systems and ESSs have a DC-DC converter and an inverter in the front-end and do not contribute to the inertial response by default [31]. Virtual inertia systems based on current/voltage feedback from the inverter output generate appropriate gating signals to present these resources as synchronous generators from the point-of-view of the grid [32].

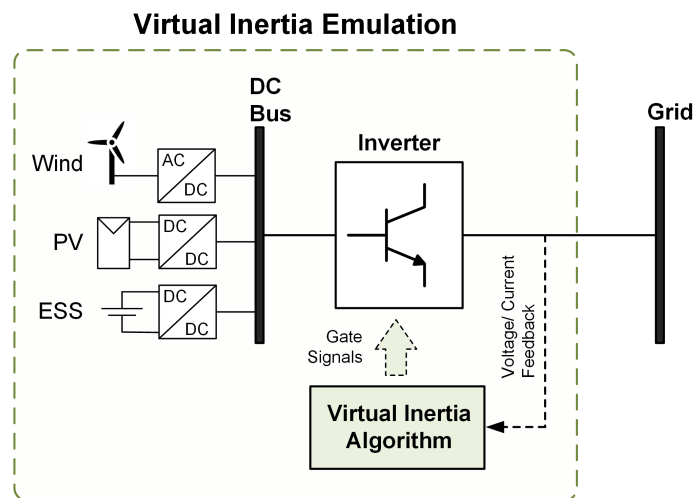


Figure 2.1. Concept of virtual inertia.

2.1 Chapter Objectives and Contributions

The main objective of this chapter is to provide a detailed literature review on the current state-of-the-art of fast-frequency support in power system through the use of virtual inertia. The specific contributions are:

1. Proposed a classification for the various fast-frequency support topologies in the literature.
2. Developed a framework to design and analyze different fast-frequency support topologies through common time-constants and inertia constants.

2.2 First Generation of Virtual Inertia Systems

Although the basic underlying concepts are similar among the various topologies in the literature, the implementation is quite varied based on the application and desired level of model sophistication. Some topologies try to mimic the exact behavior of the synchronous generators through a detailed mathematical model that represents their dynamics. Other approaches try to simplify this by using the simplified swing equation to approximate the behavior of synchronous generators, while others employ an approach that makes the inverter units responsive to frequency changes in the power system. This chapter discusses the various topologies that have been proposed in the literature.

Figure 2.2 shows a general classification of various topologies that are available in the literature for virtual inertia implementation. The most relevant literature related to topologies is also listed. Among the listed topologies, the synchronverter, the Ise lab's topology, the virtual synchronous generator (most popular in literature from each

classification), and the droop control were selected for a detailed description. A brief description of the remaining topologies is also provided.

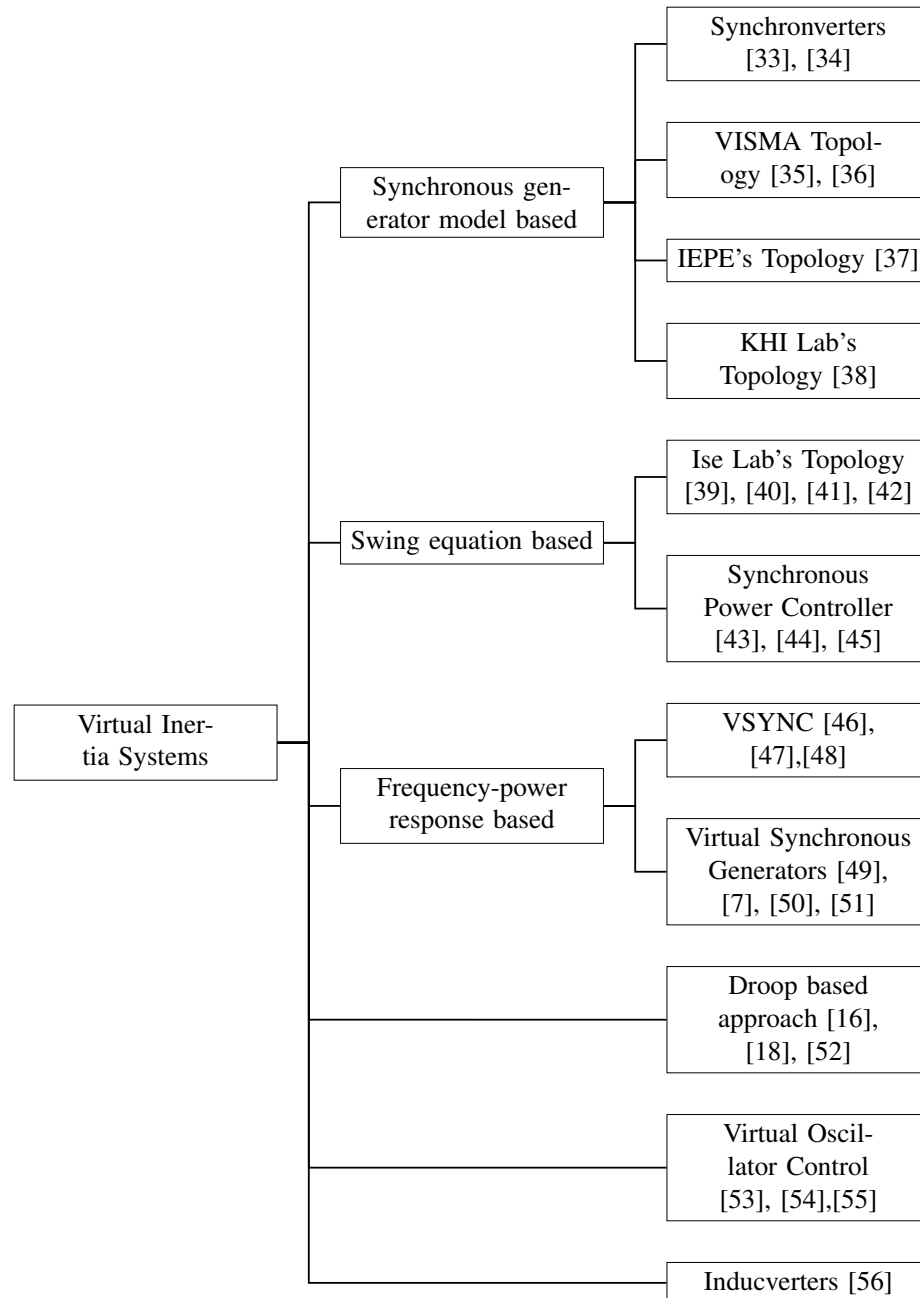


Figure 2.2. Classification of different topologies used for virtual inertia implementation.

2.2.1 Synchronverters: A Synchronous Generator Model-based Topology

Synchronverters operate the inverter-based units as synchronous generators (SGs) representing the same dynamics from the point-of-view of the grid [33]. This is based on the notion that such a strategy allows traditional operation of the power system to be continued without major changes in the operational structure. The topology is well developed in the literature by Q.C. Zhong [57]. A frequency drooping mechanism is used to regulate the power output from the inverter similar to how the SG regulates its power output [58]. The following basic equations are used to capture the dynamics of the SG:

$$T_e = M_f i_f \langle i, \widetilde{\sin\theta} \rangle \quad (2.1)$$

$$e = \dot{\theta} M_f i_f \widetilde{\sin\theta} \quad (2.2)$$

$$Q = -\dot{\theta} M_f i_f \langle i, \widetilde{\cos\theta} \rangle \quad (2.3)$$

where T_e is the electromagnetic torque of the synchronverter, M_f is the magnitude of the mutual inductance between the field coil and the stator coil, i_f is the field excitation current, θ is the angle between the rotor axis and one of the phases of the stator winding, e is the no load voltage generated, and Q is the generated reactive power. In Equations (2.1) and (2.3), $\langle \cdot, \cdot \rangle$ represents the standard inner product of two vectors in \mathbb{R}^3 . The three-phase

stator current, i , $\widetilde{\sin\theta}$, and $\widetilde{\cos\theta}$ are vectors defined as follows:

$$i = \begin{bmatrix} i_a \\ i_b \\ i_c \end{bmatrix}; \widetilde{\sin\theta} = \begin{bmatrix} \sin\theta \\ \sin(\theta - \frac{2\pi}{3}) \\ \sin(\theta - \frac{4\pi}{3}) \end{bmatrix}; \widetilde{\cos\theta} = \begin{bmatrix} \cos\theta \\ \cos(\theta - \frac{2\pi}{3}) \\ \cos(\theta - \frac{4\pi}{3}) \end{bmatrix} \quad (2.4)$$

Equations (2.1), (2.2), and (2.3) are first discretized and then solved in each control cycle in a digital controller to generate the gating signals for the distributed energy resource (DER) unit under consideration. Figure 2.3a shows the basic schematic of the synchronverter. The dashed box represents the control part of the synchronverter, the details of which are illustrated in Figure 2.3b. The inverter output current and grid voltage are the feedback signals utilized to solve the differential equations within the controller. Additionally, the continuous reference active and reactive power that the synchronverter needs to inject/absorb to/from the DC bus can be set along with desired moment of inertia J and damping factor D_p . The selection of these parameters is crucial from the point-of-view of the stability of the system as shown in [59]. The control inputs are the mechanical torque, T_m and $M_f I_f$, which can be generated through the reference active and reactive power, respectively. The frequency and voltage loops, as indicated in Figure 2.3b, are used to generate the control inputs. The outputs of the controller are the voltage amplitude e and the phase command θ for the pulse width modulator (PWM).

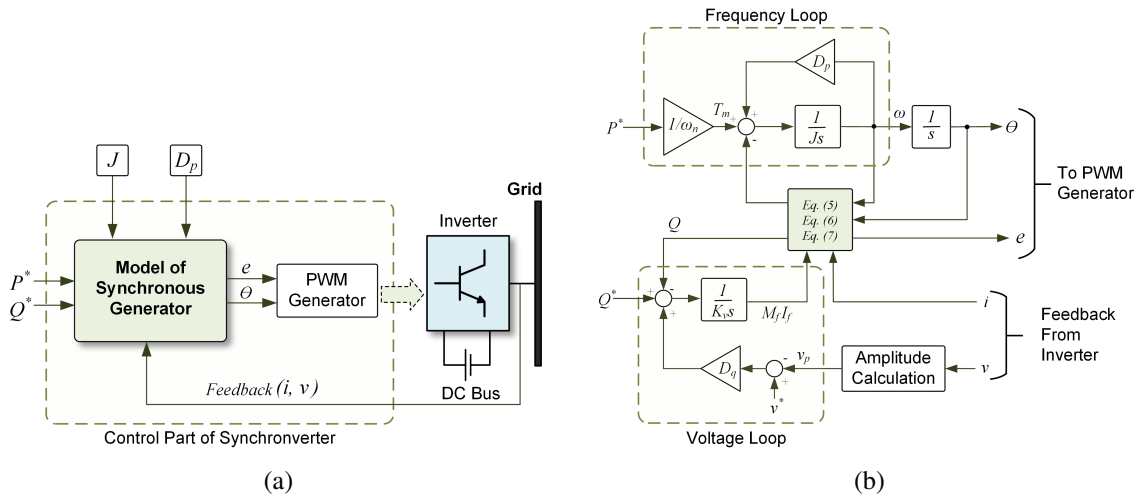


Figure 2.3. Synchronverter Topology: (a) Overall schematic showing operating principle. (b) Detailed control diagram showing the modeling equations.

The underlying equations of a synchronverter topology form an enhanced PLL (sinusoid-locked loop), making it inherently capable of maintaining synchronism with the terminal voltage [60]. Single-phase variants of the synchronverter have also been designed in [61]. The basic version of synchronverter requires a PLL to initially synchronize with the grid, however, the use of PLLs in weak grids is known to be prone to instabilities [62]–[64]. To counteract this, self-synchronized synchronverters are introduced in [34]. The synchronverter topology has also inspired the operations of rectifiers as synchronous motors [65] which helps in obtaining an inertial response from the load side of the power system. Moreover, the voltage-source based implementation means that synchronverters can be operated as grid forming units, and ideally suited for inertia emulation from inverter units that are not connected with the main grid. The fact that the frequency derivative is not required for the implementation is a major advantage as derivative terms often induce noise in the system. Although the synchronverter can

replicate the exact dynamics of an SG, the complexity of the differential equations used can result in numerical instability. Moreover, a voltage-source based implementation means there is no inherent protection against severe grid transients, which may result in need of external protection systems for safe operation.

2.2.2 Ise Lab's Topology: A Swing Equation-based Topology

The topology developed by Ise lab for virtual inertia implementation is similar to the synchronverter approach described previously, but instead of using a full detailed model of the SG, the topology solves the power-frequency swing equation every control cycle to emulate inertia [39]. The schematic diagram of the topology illustrating the operating principle is shown in Figure 2.4a. The controller senses the inverter output current i and the voltage of the point of connection v , and computes the grid frequency ω_g and active power output of the inverter P_{out} . These two parameters are inputs to the main control algorithm block along with P_{in} which is the prime mover input power [40]. Within the control algorithm, the swing equation given by Equation (2.5) is solved every control cycle thus generating the phase command θ for the PWM generator. The typical swing equation of an SG is:

$$P_{in} - P_{out} = J\omega_m \left(\frac{d\omega_m}{dt} \right) + D_p \Delta\omega \quad (2.5)$$

$$\Delta\omega = \omega_m - \omega_g \quad (2.6)$$

where P_{in} , P_{out} , ω_m , ω_g , J , and D_p are the input power (similar to the prime mover input power in a SG), the output power of the inverter, virtual angular frequency, grid/reference angular frequency, moment of inertia, and the damping factor, respectively. A model of

the governor, as shown in Figure 2.4b, is utilized to compute the input power P_{in} based on the frequency deviation. The governor is modeled as a first-order lag element with gain K and time-constant T_d . P_0 represents continuous power reference for the inverter unit. The delay in the governor model leads to higher ROCOF and thus higher frequency nadirs as a consequence. The voltage reference e can be generated through $Q - v$ droop approach as described in [41].

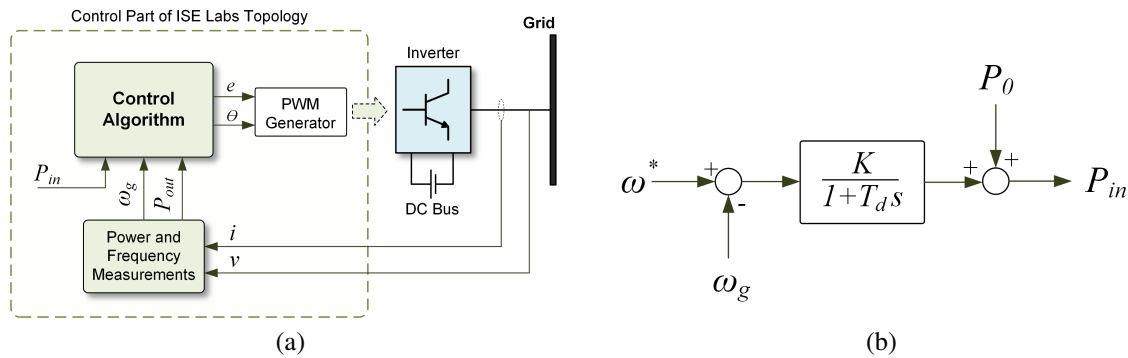


Figure 2.4. Ise Lab's Topology: (a) Overall schematic showing operating principle. (b) The governor model to compute input power.

Similar to the synchronverter, the derivative of frequency is not needed to implement the control algorithm. This is highly beneficial as frequency derivatives are known to introduce noise in the system which makes the system difficult to control. Additionally, this topology can be used to operate inverters as grid forming units. However, problems related to numerical instability remain, which along with improper tuning of parameters J and D_p , can lead to oscillatory system behavior [40].

2.2.3 Virtual Synchronous Generators: A Frequency-Power Response-based Topology

The main idea behind virtual synchronous generators (VSG) is to emulate the inertial response characteristics of an SG in an inverter system, specifically the ability to respond to frequency changes [51], [66]. This emulates the release/absorption of kinetic

energy similar to that of an SG, thus presenting the inverter as a dispatchable source [67], [68]. This dynamic control is based on the derivative of the frequency measurement and behaves similarly to inertial power release/absorption by an SG during a power imbalance. Thus, the VSG is a dispatchable current source that regulates its output based on system frequency changes. This is one of the simplest approaches to implement virtual inertia in inverters as it does not incorporate all the detailed equations involved in an SG. However, operating multiple inverter units as current sources are known to result in instability [69].

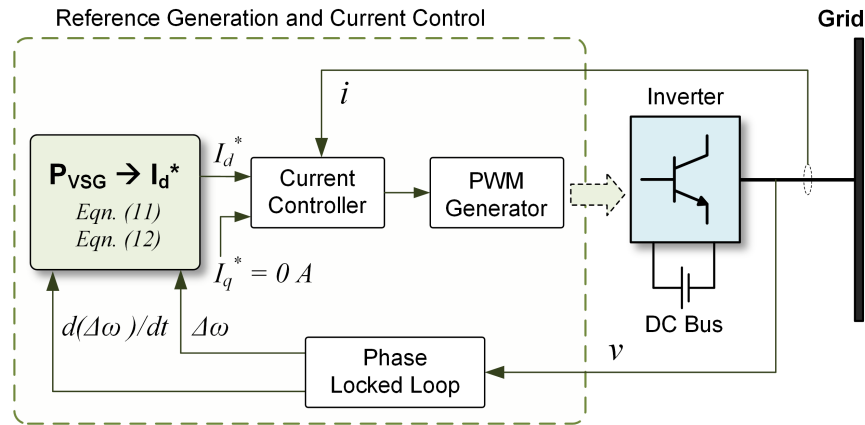


Figure 2.5. Virtual synchronous generator topology.

The output power of the VSG converter is controlled using Equation (2.7):

$$P_{VSG} = K_D \Delta\omega + K_I \frac{d\Delta\omega}{dt} \quad (2.7)$$

where $\Delta\omega$ and $\frac{d\Delta\omega}{dt}$ represent the change in angular frequency and the corresponding rate-of-change. K_D and K_I represent the damping and the inertial constant, respectively.

The damping constant is similar to the frequency droop and helps return the frequency to a steady-state value and reduce the frequency nadir. The inertial constant arrests the ROCOF by providing fast dynamic frequency response based on the frequency derivative.

This feature is especially important in an isolated grid where the initial ROCOF can be very high, leading to unnecessary triggering of protection relays. The VSG topology is illustrated in Figure 2.5. A PLL is used to measure the change in system frequency and ROCOF [67]. Then, using Equation (2.7), the active power reference for the inverter is computed. The current references are then generated for the current controller based on this reference power. The topology illustrated here assumes a direct-quadrature (d - q) based current control approach, but any other current control techniques ([70]) may be used. For d - q control, d -axis current reference can be calculated as [71]:

$$I_d^* = \frac{2}{3} \left(\frac{V_d P_{VSG} - V_q Q}{V_d^2 + V_q^2} \right) \quad (2.8)$$

The q -axis current reference is set to zero as it is assumed that only the active power is being controlled. The current controller based on the grid current feedback generates the gate signals to drive the inverter. Thus, the inverter behaves as a current-controlled voltage source inverter [7], [70].

This topology is used by the European VSYNC research group [48], [67] and has demonstrated the effectiveness of inertia emulation using VSG topology through real-time simulations [46] and several field tests [72]. In [71], experimental verification of the topology is presented for remote microgrid applications. The VSG topology has also been widely employed for virtual inertia emulation from wind systems as reported in [47], [73]. The main drawback of this topology is that it may not be suitable to be implemented in islanded modes where the virtual inertia unit has to operate as a grid forming unit.

Accurate measurement of the frequency derivative through PLLs can be challenging for

this kind of implementation [74]. The performance of PLLs can degrade and compete against each other, especially in weak grids [56], [75]. PLL systems are known to show steady-state errors and instability especially in weak grids with frequency variations, harmonic distortions, and voltage sags/swells [62]–[64]. With traditional virtual inertia controllers, a low pass filter (LPF) is used to filter out PLL measurement noise. The delay caused by the LPF is known to cause instability, especially under high controller gain values [76]. Thus, using an LPF with low cut-off frequencies limits the controller gains and the effectiveness of the controller in providing fast-frequency support. In [77], it was shown that the problems with instability are even more pronounced when a proportional-integral (PI) controller is used to implement the inner-current control loop of the inverter. Accordingly, a VSG requires a robust and sophisticated PLL for a successful implementation [78]. Another disadvantage of the VSG approach is that the derivative term used to compute the ROCOF makes the VSG sensitive to noise which can lead to unstable operation.

2.2.4 Droop-based Approaches

The approaches described so far try to mimic or approximate the behavior of SGs to improve the inertial response of inverter-dominated power systems. Different from these techniques, the frequency-droop based controllers that have been developed for autonomous operation of isolated microgrid systems [79], [80]. Based on the assumption that the impedance of the grid is inductive, the frequency droop is implemented as:

$$\omega_g = \omega^* - m_p(P_{out} - P_{in}) \quad (2.9)$$

where ω^* is the reference frequency, ω_g is the local grid frequency, P_{in} is the reference set active power, P_{out} is the measured active power output from the DER unit, and m_p is the active power droop. Similarly, the voltage-droop is implemented as:

$$v_g = v^* - m_q(Q_{out} - Q_{in}) \quad (2.10)$$

where v^* is the reference voltage, v_g is the local grid voltage, Q_{in} is the reference set reactive power, Q_{out} is the measured reactive power output from the DER unit, and m_q is the reactive power droop.

The schematic of a frequency-droop controller based on Equation (2.9) is shown in Figure 2.6. Often a low pass filter is used when measuring the output power to filter out high-frequency components from the inverter [16]. In the literature [75], [81], it has already been shown that the use of this filter makes the droop-based control approximate the behavior of virtual inertia systems. The proof was first presented by Arco et al. [75] and is repeated here for convenience.

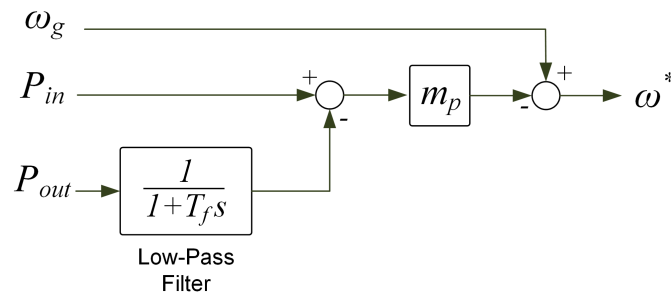


Figure 2.6. Schematic for frequency droop control.

Based on the schematic of Figure 2.6:

$$P_{out} = (1 + T_f s) \left\{ \frac{1}{m_p} (\omega_g - \omega^*) + P_{in} \right\} \quad (2.11)$$

Rearranging,

$$P_{in} - P_{out} = \frac{1}{m_p} (\omega^* - \omega_g) + T_f \cdot \frac{1}{m_p} \cdot s \cdot \omega^* \quad (2.12)$$

This equation is of a similar form of the virtual synchronous generator described in

Equation (2.7). The exact approximation is as follows:

$$K_I = T_f \cdot \frac{1}{m_p} \quad (2.13)$$

$$K_D = \frac{1}{m_p} \quad (2.14)$$

Hence, the filters used for power measurements in these controllers constitute a delay which is mathematically equivalent to virtual inertia, while the droop gain is equivalent to damping. However, the traditional droop-based systems described by Equations (2.9) and (2.10) are known to have slow transient response. Moreover, the inductive grid assumption may not always be valid. Methods to improve the droop controllers, such as using virtual output impedance [16] or improving dynamic behavior of the droop scheme, have been proposed. In [12] and [82], a technique to emulate virtual inertia by a modified droop approach was also presented.

2.3 Other Topologies

Some other topologies that have been proposed in the literature are — virtual synchronous machine, referred to as “VISMA” in the literature, Institute of Electrical Power Engineering (IEPE’s) topology, Kawasaki Heavy Industries (KHI) lab’s topology, synchronous power controllers (SPC), virtual oscillators, inducverters, etc. The basic concept of inertia emulation remains the same in all these techniques. The VISMA topology as proposed in [35] uses $d - q$ (synchronous reference frame) based mathematical model of a synchronous machine in a digital controller. Instantaneous measurements of the grid voltage are used to compute the stator currents of the virtual machine and these currents are injected through a hysteresis current control approach using a power inverter. To improve robustness, a three-phase model has been proposed in [36] over a $d - q$ based model. This is especially effective under unsymmetrical load conditions or rapid disturbances in the grid. A comparison between the VISMA algorithm implemented as a current source versus a voltage source has also been performed in [37]. The VISMA model implemented as a voltage source is referred to as IEPE’s topology in the literature [32]. Instead of using voltage as input as with the VISMA topology, IEPE’s topology uses the DER output current as input and generates reference voltages for the virtual machine. The IEPE topology is better suited for islanded operation, but transient currents, particularly during the synchronization processes when operated in grid connected mode, can be difficult to deal with. In the KHI topology, instead of using a detailed dynamic model of SG an equivalent governor and automatic voltage regulator (AVR) model are implemented in a digital controller to generate voltage amplitude and

phase reference for the virtual machine [38]. The reference is then used to generate current references based on an algebraic-phasor representation of the SGs.

Another popular topology for virtual inertia implementation is the SPC as proposed in [43]. The general structure of the control algorithm is similar to the structure proposed in the Ise lab's topology, but instead of operating the converter as a voltage-controlled system or a current-controlled system, it implements a cascaded control system, with an outer voltage loop and an inner current control loop through the use of a virtual admittance. In general, such a cascaded control structure provides inherent over-current protection during severe transient operating conditions. This is lacking in other open-loop approaches such as synchronverters or the Ise lab's topology [83] described previously. SPC also avoids the discontinuities encountered in solving the mathematical models, thus making the system more robust against numerical instabilities. The nested loop structure, however, does entail complexity in tuning the control system parameters. Furthermore, at its core instead of using the swing equation for inertia emulation, a second-order model with an over-damped response is proposed. This helps to reduce the oscillations in the system [45]. Improved forms of this second-order model were presented in [44], [45].

Inducverters [56] are one of the recent topologies that have been proposed which tries to mimic the behavior of induction generators instead of SGs. This method has the advantage of auto-synchronization without a PLL [84]. A virtual-inertia based static synchronous compensator (STATCOM) controller was proposed in [81] which behaves like a synchronous condenser. The virtual inertia controller was used to exploit the fact that no PLL is required, hence providing improved voltage regulation compared to traditional STATCOMs with PLL units. Virtual oscillator controller (VOC) is another

approach where, instead of mimicking synchronous/induction generators, a non-linear oscillator is implemented within the controller to synchronize DER units without any form of communication [53], [54]. This approach is particularly beneficial for a grid largely dominated with DERs, as the controller is intrinsically able to maintain synchronism and share the total system load [55].

2.3.1 Summary of Topologies

A summary table which highlights the key features and weakness of various virtual inertia control topologies is presented in Table 2.1.

Table 2.1. Summary of Virtual Inertia Control Topologies

Control Technique	Key Features	Weaknesses
Synchronous generator model based	<ul style="list-style-type: none"> • Accurate replication of SG dynamics • Frequency derivative not required • PLL used only for synchronization 	<ul style="list-style-type: none"> • Numerical instability concerns • Typically voltage-source implementation; no over-current protection

Table 2.1. Summary of Virtual Inertia Control Topologies

Control Technique	Key Features	Weaknesses
Swing equation based	<ul style="list-style-type: none"> • Simpler model compared to SG based model • Frequency derivative not required • PLL used only for synchronization 	<ul style="list-style-type: none"> • Power and frequency oscillations • Typically voltage-source implementation; no over-current protection
Frequency-power response based	<ul style="list-style-type: none"> • Straightforward implementation • Typically current-source implementation; inherent over-current protection 	<ul style="list-style-type: none"> • Instability due to PLL, particularly in weak grids • Frequency derivative required, system susceptible to noise

Table 2.1. Summary of Virtual Inertia Control Topologies

Control Technique	Key Features	Weaknesses
Droop-based approach	<ul style="list-style-type: none"> • Communication-less • Concepts similar to traditional droop control in SGs 	<ul style="list-style-type: none"> • Slow transient response • Improper transient active power sharing

2.4 Design Procedures and Simulation Results

In this section, three of the major virtual inertia topologies were simulated in a diesel generator based remote microgrid system. The design procedures and simulation results presented are aimed to supplement the concepts of virtual inertia topologies. Three of the topologies — the synchronverter, the Ise lab’s topology, and the VSG — were implemented and their performance was studied in a common benchmark. Moreover, a procedure is provided to choose appropriate parameters for the virtual inertia systems. The three virtual inertia systems were designed in a common framework so that the different parameters used are more relatable to each other. To this end, constants in each topology were selected such that the virtual inertia system injects/absorbs the same amount of active power for a given frequency change. Moreover, the inertial constant and the damping constant have the same proportion and were related through a time constant T_f of 0.01 s in all the simulations. This led to inertia constant H of 1 s in all simulation cases for the virtual inertia unit. The schematic used for the virtual inertia simulation

benchmark is shown in Figure 2.7. The generator was rated at 13 kVA, while the PV unit was rated at 6 kWp [71]. A separate, dedicated inverter unit rated at 10 kW was used as the virtual inertia unit. In all the cases, the steady-state power output from the inverter was set to 1000 W. It was assumed that the DC side of the inverter was connected to a 400 V DC source which remained constant in all the simulations.

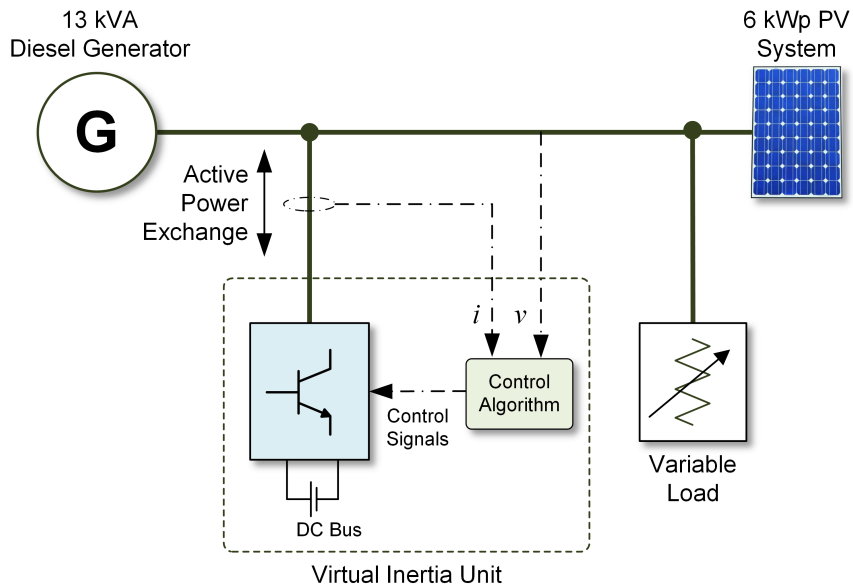


Figure 2.7. Schematic diagram of the virtual inertia simulation benchmark.

2.4.1 Design of synchronverter topology

The main parameters to be computed to implement a synchronverter are the moment of inertia J and the damping factor D_p . The parameter D_p can be calculated using Equation (2.15) from [33].

$$D_p = -\frac{\Delta T}{\Delta \omega} = -\frac{\Delta P}{\omega_g \Delta \omega} \quad (2.15)$$

Once D_p was calculated, the moment inertia J was computed using the desired time constant for the system, τ_f :

$$\tau_f = \frac{J}{D_p} \quad (2.16)$$

In this case, D_p was calculated to be 14.072 assuming ΔP of 100% (10 kW) for 0.5% change in the angular frequency (1.885 rad/s). Then for a time-constant of 0.01 s, the J value was calculated to be 0.140. The inertia constant from the synchronverter is:

$$H = \frac{J\omega_g^2}{2P_{rated}} = 1s \quad (2.17)$$

The frequency and ROCOF of the system after a step-increase of 2 kW on the load, with and without the synchronverter, are presented in Figure 2.8a and 2.8b, respectively. The dip in frequency and the ROCOF of the system were reduced with the addition of the synchronverter, as expected. The additional inertia from the synchronverter increased the settling time for the frequency compared to when there was no synchronverter in the system. As shown in Figure 2.8c, the synchronverter increases its active power output in response to the frequency event much like the behavior of an SG.

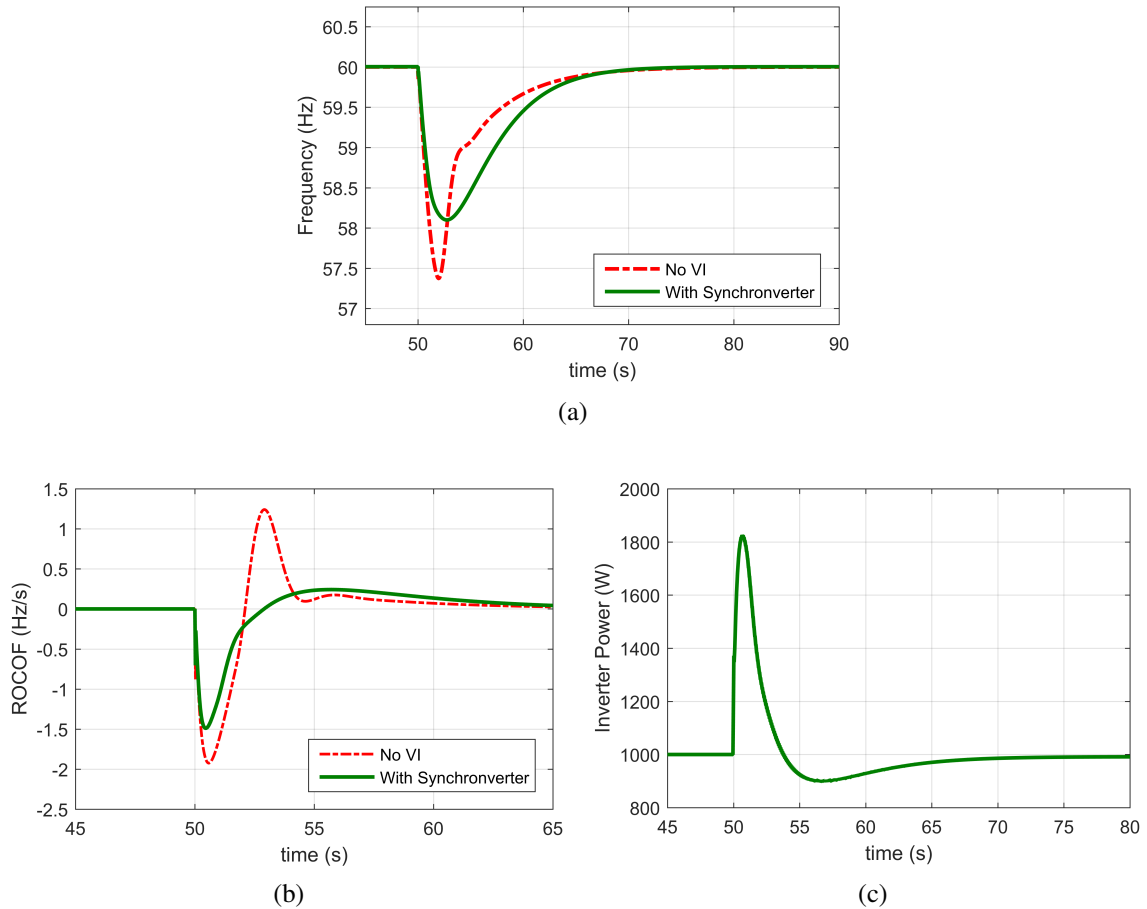


Figure 2.8. Simulation results from a Synchronverter: (a) System frequency after a step-increase of 2 kW load. (b) ROCOF after a step-increase of 2 kW load. (c) Increase in inverter power in response to system frequency decrease.

2.4.2 Design of Ise Lab's topology

For the design of the Ise lab's topology, the same values for the constants J and D_p that were calculated for synchronverter in Section 2.4.1 were used. For the implementation of the governor model, a K value of 0.01 with a time delay T_d of 0.16 s was used. The frequency and ROCOF of the system after a step-increase of 2 kW on the load, with and without the Ise lab's system, is presented in Figure 2.9a and 2.9b, respectively. The dip in the frequency and the ROCOF of the system was reduced with the addition of the virtual inertia unit, as expected. The additional inertia from the virtual

inertia system increased frequency settling time compared to the case without the virtual inertia system. The settling time, however, was higher than with the synchronverter.

Figure 2.9c shows the power injected by the inverter during the step-load increase. There is a short transient at 50 s, which was a consequence of numerical oscillation in solving the swing equation. The peak-power injected was similar to that of the synchronverter, but the time taken for the power to return to the steady-state value of 1000 W was much longer, leading to a larger energy usage from the DC side.

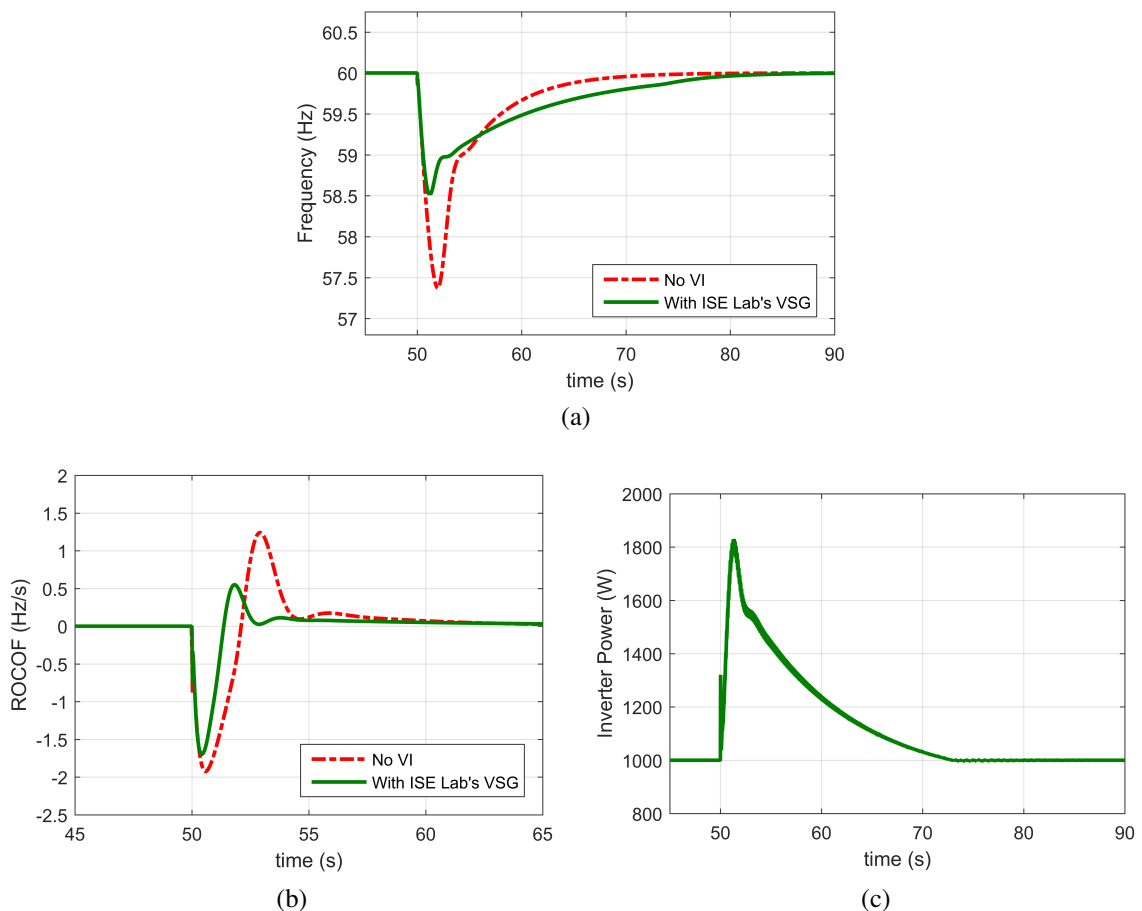


Figure 2.9. Simulation results from ISE lab's topology: (a) System frequency after a step-increase of 2 kW load. (b) ROCOF after a step-increase of 2 kW load. (c) Increase in inverter power as a response to system frequency decrease.

2.4.3 Design of virtual synchronous generator topology

For implementing the VSG topology, the main parameters to be designed are the inertia constant K_I and the damping constant K_D . The parameter K_D can be calculated using:

$$K_D = \frac{\Delta P}{\omega_g \Delta \omega} \quad (2.18)$$

Once K_D was calculated, the inertia constant K_I was computed using the desired time constant for the system, τ_f :

$$\tau_f = \frac{K_I}{K_D} \quad (2.19)$$

In this case, the damping constant, K_D , was calculated to be 14.07, assuming ΔP of 100% (10 kW) for 0.5% change in the angular frequency (1.885 rad/s). Then, for a time-constant of 0.01 s, the K_I value was calculated to be 0.14. The inertia constant from the VSG is:

$$H = \frac{K_I \omega_g^2}{2P_{rated}} = 1s \quad (2.20)$$

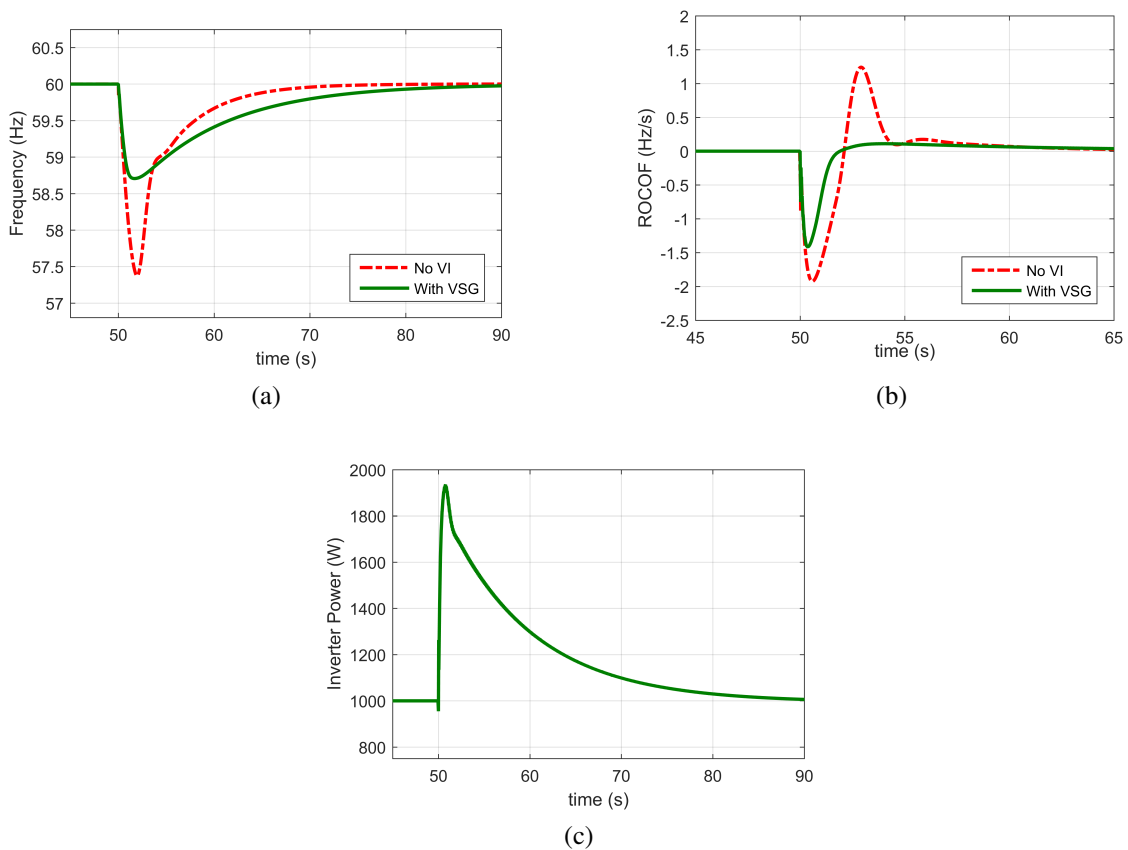


Figure 2.10. Simulation results from a Virtual Synchronous Generator: (a) System frequency after a step-increase of 2 kW load. (b) ROCOF after a step-increase of 2 kW load. (c) Increase in inverter power as a response to system frequency decrease.

The frequency and ROCOF of the system after a step-increase of 2 kW on the load, with and without the VSG, is presented in Figure 2.10a and 2.10b, respectively. The dip in frequency and the ROCOF of the system were reduced with the addition of the VSG, as expected. As with the previous cases, the additional inertia from the VSG slowed the system down, and the settling time for the frequency was increased compared to the case without virtual inertia. The peak-power injected was slightly higher than that of the synchronverter and Ise lab's topology. However, the time taken for the power to return to the steady value of 1000 W was much longer than for the synchronverter leading to a

larger energy usage from the DC side.

2.4.4 Summary of Simulations Results

The simulation results are summarized in Table 2.2 in terms of parameters like the minimum frequency, maximum ROCOF, settling time, peak power, and energy exchange. The settling time is defined here as the time required for the frequency to return to and stay within ± 0.25 Hz of the final steady-state frequency after a disturbance. The energy exchange was calculated over the time period where the inverter exchanges power with the system. With all three topologies, the minimum frequency and ROCOF were reduced by similar amounts. The peak power delivered by the inverter varied slightly, with the highest value of 1929 W for the VSG topology. The most pronounced differences were in the settling time for the frequency and the energy exchange. Compared to systems with no virtual inertia, the settling time has increased in all three cases. This was expected as adding virtual inertia slows down the frequency dynamics. The ISO8528-5 standard for generators sets recommends a settling time of 10 s [22]. The settling time, however, increased to 13.2 s with synchronverter and an even higher value of 17.7 s and 17.9 s with the Ise lab's and VSG respectively. This led to a relatively higher energy exchange in these two topologies of 3.8 Wh and 4.9 Wh compared to that 0.8 Wh with the synchronverter. Moreover, there was a short-energy recovery period in the power plot of the synchronverter as seen in Figure 2.8c which led to a lower energy exchange estimate for the synchronverter.

Table 2.2. Performance comparison of synchronverter, Ise lab's and virtual synchronous generator topologies.

Parameter	No VI	Synchronverter	Ise Lab	VSG
Minimum Frequency	57.3 Hz	58.1 Hz	58.6 Hz	58.3 Hz
Maximum ROCOF	1.9 Hz/s	1.5 Hz/s	1.6 Hz/s	1.7 Hz/s
Settling time	11.3 s	13.2 s	17.7 s	17.9 s
Peak power delivered	0W	1825 W	1800 W	1929 W
Energy exchanged	0 Wh	0.8 Wh	3.8 Wh	4.9 Wh

Therefore, by appropriate selection of the parameters for the topologies through the time constant T_f and/or the inertia constant H , similar inertial response can be achieved in terms of frequency deviation reduction and power exchange from the inverter. Based on the topology, the exact dynamics represented by the system may vary. The selection of a particular topology depends on the application and the desired level of replication of the dynamics of the SG. Topologies like the synchronverter and the Ise lab's topology may be more suitable for isolated power systems as they can operate autonomously as grid forming units. The VSG topology, on the other hand, behaves more like a grid following unit with added inertial response capabilities and is more suited towards interconnected operations. The synchronverter or Ise lab's topology is more suitable for a closer approximation of SG dynamics. If the main aim, however, is to make the DER unit responsive to frequency changes, the VSG approach provides a far simpler implementation.

2.5 Second Generation: Optimization of Virtual Inertia Systems

The first generation of virtual inertia systems in the literature focused on developing novel topologies for emulation of inertia using power electronic converters. These topologies have matured since and recently the field is more focused on improving and

optimizing the performance of these topologies from the point-of-view of enhanced dynamics, stability, and minimizing energy storage requirements.

2.5.1 Second Generation of Synchronverters

Improved versions of the synchronverter have been proposed in [81, 82] which makes the synchronverter more robust and allows for a more accurate dynamic representation of SGs. One of the main improvements (among others) in [85] is virtually increasing the filter inductance of the synchronverter, which improved the stability compared to the original synchronverter. This modification allowed for improved control over the response speed of the frequency loop proposed in [33]. In a similar theme, an auxiliary loop around the frequency-loop was proposed in [86] which allowed for free control of the response speed of synchronverter. This auxiliary loop did not affect the steady-state drooping mechanism of the synchronverter which is very desirable. By changing the inertia constant J and a different tunable constant D_f , the desired response speed was achieved. In [87], a synchronverter with analytically determined bounds for frequency and voltage was introduced. In traditional synchronverters, saturation units were employed for this purpose, but such an approach can lead to instability due to wind-up. Instead, analytically determined bounds based on the system parameters were proposed to improve stability.

2.5.2 Second Generation of Ise Lab's Topology

In the traditional Ise lab's topology, active power oscillation during the inertia emulation has been identified as one of the major concerns [40]. Typically, during a frequency event, the DER unit needs to release/absorb a high amount of power, which

may exceed their power ratings. This is not a problem for conventional SGs as they have inherently overrated operation capabilities. But in the case of inverters, the switches have to be over-sized to handle such peak power, leading to an increase in inverter size and, consequently, cost [63]. In [40], an alternating moment of inertia emulation approach was proposed to make the system less susceptible to such oscillations. The J parameter was changed based on the relative “virtual angular velocity” and its rate of change. The proposed alternating moment of inertia approach not only stabilized the system under consideration but other nearby virtual inertia units as well. Similarly, in [87] another technique of adjusting the “virtual stator reactance” of the virtual inertia unit has also been proposed to reduce such active power oscillations. This approach was somewhat similar to the approach described for synchronverters in [85]. The technique was also found to aid in proper transient active power-sharing when operating multiple virtual inertia units in a microgrid environment. In [88], a particle swarm optimization technique was developed to properly tune the parameters of the system and achieve smooth transitions after a disturbance when operating multiple virtual inertia units. article swarm optimization technique was developed to properly tune the parameters of the system and achieve smooth transitions after a disturbance when operating multiple virtual inertia units.

2.5.3 Second Generation of Virtual Inertia Systems

In terms of improvement in VSG topologies, some researchers have developed techniques to try to minimize the frequency nadirs/peaks in the system at the expense of higher energy usage and peak transient power exchange through the virtual inertia systems [87, 88]. Other researchers, meanwhile, have focused on reducing the energy storage

requirements and limiting peak transient power in virtual inertia systems even though it leads to slightly higher frequency nadirs/peaks [24], [49]. A self-tuning VSG was developed in [49] using an online optimization technique to tune the K_I and K_D parameters of the VSG control algorithm to minimize the frequency excursions, the ROCOF, and the power flow through the ESS. Although the frequency excursions were slightly higher in the case of the self-tuning algorithm, the power flow through the ESS was reduced by 58%. Moreover, the technique used less energy per Hz of frequency reduction than a constant parameter VSG.

On a similar note of energy-saving, an online neural-network-based controller was proposed in [24]. It used adaptive dynamic programming (ADP) based approach to optimize the system and minimize energy usage while limiting transient power. The controller supplemented the power references generated by the main VSG algorithm to improve the dynamics of virtual inertia as shown in Figure 2.11a. The proposed ADP controller used a neural network structure with two different networks — an action network and a critic network as shown in Figure 2.11b. The idea behind the design of the critic network was to adapt its weight such that the optimal cost function $J^*(X(t))$ satisfies the Bellman principle of optimality as given by:

$$J^*(X(t)) = \min_{u(t)} \{J^*(X(t+1)) + r(X(t)) - U_c\} \quad (2.21)$$

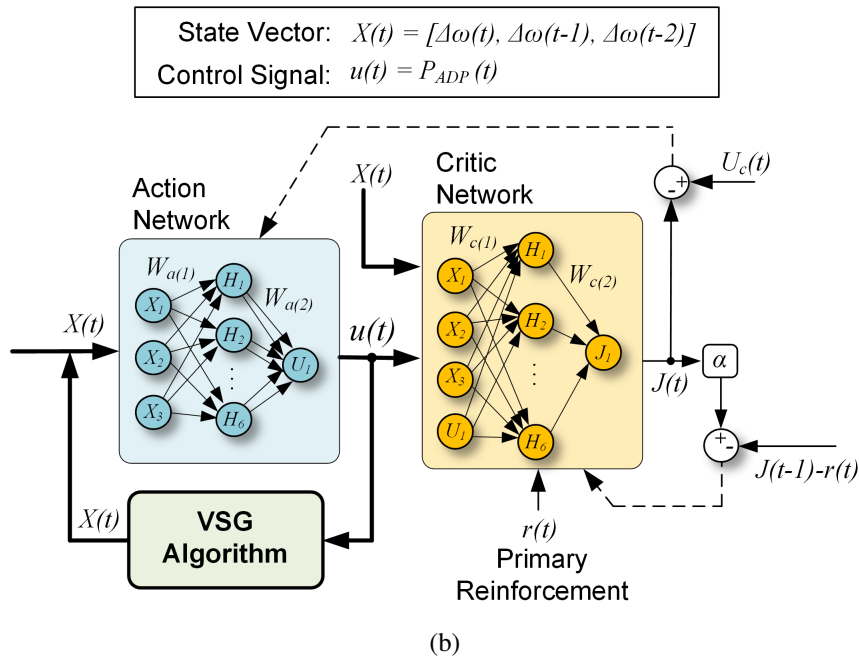
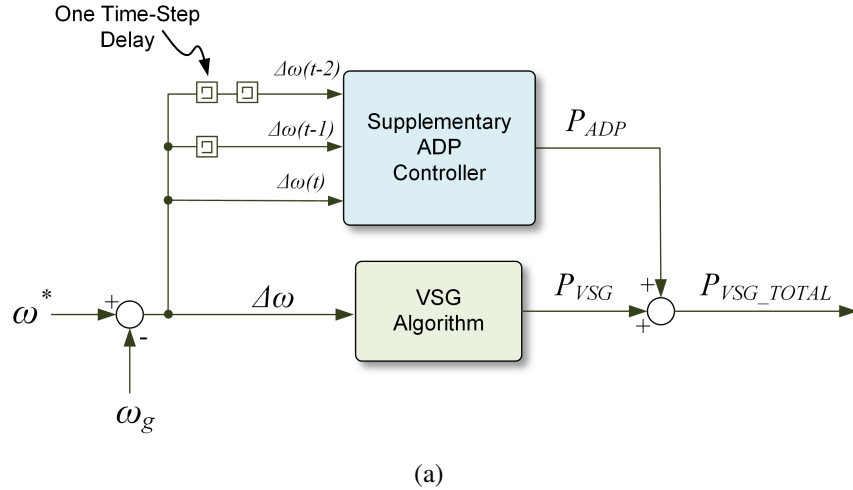


Figure 2.11. Modified Virtual Synchronous Generator using Adaptive Dynamic Programming (a) Overall schematic of the controller. (b) The action and critic neural network-based structure.

where $r(t)$ is the reinforcement signal for the critic network and U_c is a heuristic term used to balance. The input to the supplementary ADP controller was the state vector $X(t)$ where the elements were the frequency error and the one and two time-step delayed frequency error signals. Based on a reinforcement learning approach, the ADP controller

generated auxiliary power reference signals P_{ADP} to return the frequency to its steady-state value faster and as a consequence reduced the energy exchange as explained in [24]. The main concern with adding virtual inertia to the system is that it can increase the frequency settling time, leading to increased energy exchange from the ESS, which subsequently shortens the life of the ESS. The online controller was able to reduce the frequency settling time and the transient peak power. Figure 2.12a (extracted from the paper [24]) shows the frequency of a PV-hydro system under step load changes with and without the ADP controller. The frequency excursion was slightly higher than using constant parameter VSG, but there was a reduction in the frequency settling time. This led to lower energy usage and lower transient power as observable in Figure 2.12b. Table 2.3 summarizes the improvement achieved in [24] through ADP-based virtual inertia controller.

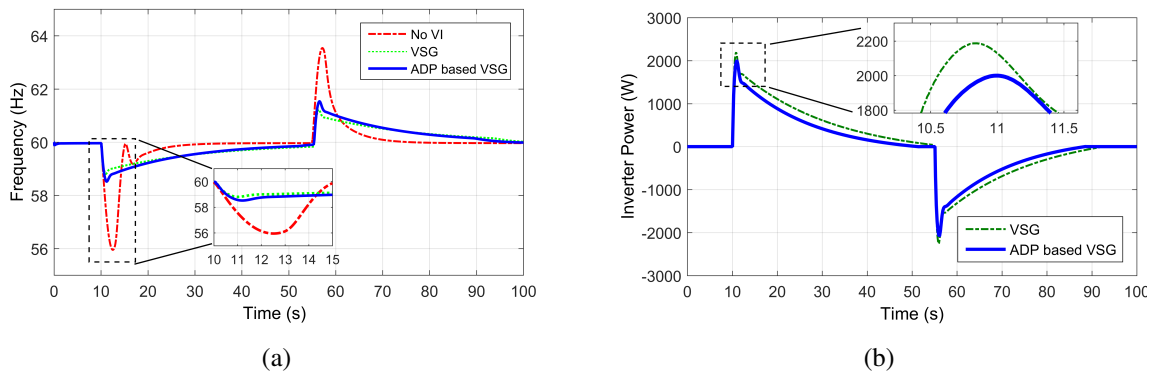


Figure 2.12. Comparison of traditional VSG controller with the online learning based controller: (a) Frequency of the system for step load changes. (b) Power exchange with the system [24].

Table 2.3. Performance comparison of the system without VI, simple VSG based and ADP based VSG [24]

Parameter	No VI	Simple VSG	ADP based VSG
Peak Power for Event A	0 W	2184 W	1979 W
Settling time for Event A	12.6s	35.1s	31.3 s
Peak Power for Event B	0 W	-2235 W	-2029 W
Settling time for Event B	11.1 s	29.1 s	26.6 s
Energy delivered (Wh)	0 Wh	8.2 Wh	6.2 Wh
Net energy exchanged (Wh)	0 Wh	1.6 Wh	0.9 Wh

A similar online learning controller was proposed for virtual inertia implementation in a double fed induction generator based system in [89]. In this case, the controller was trained to restrict the frequency excursions to a minimum while maintaining the rotor speed of the double fed induction generator within a safe operating range, rather than saving the energy flow from ESS. Other techniques to optimize the virtual inertia have been proposed in [90] using Linear-quadratic-regulator (LQR) and in [91] using fuzzy logic to minimize frequency deviations and ROCOF.

2.6 Third Generation of Virtual Inertia Systems

The three distinct generations of research focus and trends in virtual inertia are summarized in Fig. 2.13. The first generation of research was focused on the development of novel topologies and the second generation was focused on improving the existing topologies as discussed in detail in Sections 2.4 and 2.5. In the third generation, the research focus has shifted towards system-level coordination. Various aspects of deployment ranging from inertia estimation, coordination of multiple units with virtual inertia and optimal placement are being studied. As the penetration of RESs increases the inertia of a power system, which in the past was assumed to be constant, will become

time-variant. System inertia estimation will be critical for planning purposes and deployment of adaptive frequency support strategies and protection schemes. Several research has also been proposed which study the optimal placement of virtual inertia in a power system and developing market mechanisms for fast-frequency support through virtual inertia [11], [92].

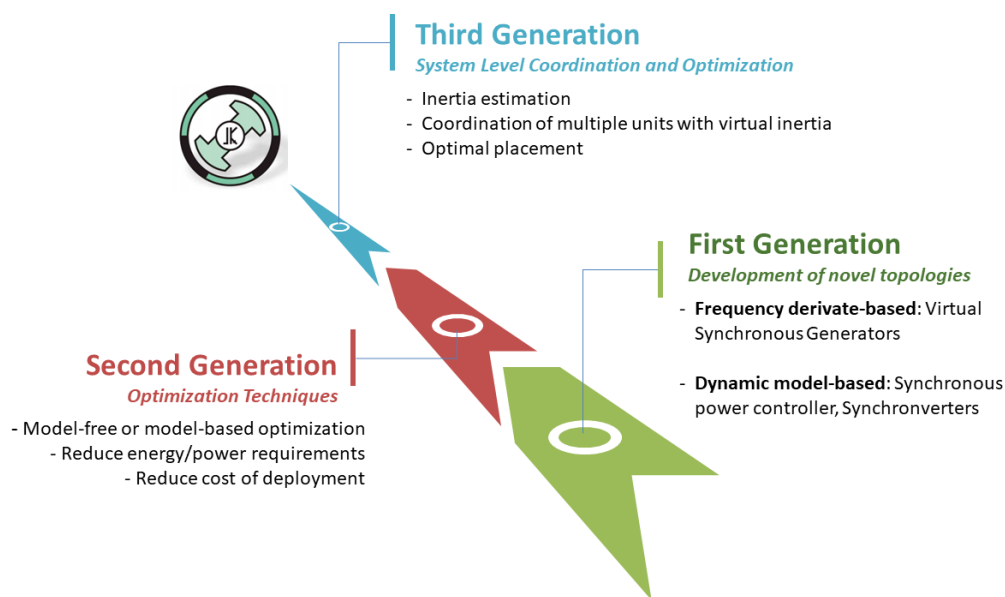


Figure 2.13. Generations of virtual inertia systems.

2.7 Chapter Conclusions

Numerous topologies for virtual inertia implementation which constitutes the “first generation” of virtual inertia systems were identified. It was shown that fundamentally the objective of all the topologies is to provide fast-frequency support through power electronic converters which are in a continuous decline in low-inertia power systems. The appropriate topology can be selected based on the required architecture (current source or voltage source implementation) and the desired level of sophistication in emulating the exact behavior of SGs. For example, for replication of the exact dynamics of SGs,

topologies such as the synchronverter, VISMA and inducverters can be used. More simplistic topologies like Ise lab's topology, SPC can be used if an approximate replication is sufficient. The VSG approach, on the other hand, is more suitable when the objective is to provide just the fast-frequency support without emulating the exact behavior of SGs. An important takeaway through the literature review was that the droop based controllers, which were regarded as a separate control method for inverter systems, are fundamentally similar to virtual inertia systems as formalized by the literature pointed out.

Next, the second generation of virtual inertia systems with a focus on the optimization of existing virtual inertia topologies was reviewed. Such algorithms can prevent degradation of ESS lifetime and allow reduced curtailment of RES units that participate in the inertial response. Furthermore, the enhancements help in improved dynamics and overall stability.

CHAPTER 3 INERTIA AND DAMPING CONSTANT ESTIMATION BASED ON MOVING HORIZON ESTIMATOR

The inertia of modern power systems is in continuous decline due to the increased utilization of RESs displacing traditional rotational synchronous generation. Low inertia power systems are prone to large ROCOF following a power imbalance, causing large frequency deviations as a result. Proper assessment of the system inertia is of critical importance for system operators to deploy effective strategies to supplement the lost inertia. The inertial response of a power system is the product of instantaneous release/absorption of power, typically from synchronous generators in response to a power imbalance (measured as the deviation in frequency from nominal). The inertia of a power system is thus dependent on the synchronous generators that are online at any given time. With non-synchronous generation sources such as PVs and wind continuously displacing the traditional generators, it is challenging to estimate the inertia of a power system at any given time [93]. The variable nature of these RESs adds another degree of uncertainty as the inertia constant of the power system becomes time-varying [94]. Furthermore, recently RESs have been deployed with characteristics that can emulate inertia as well [95], [96]. Hence, the inertial response from RESs also needs to be accounted for when estimating the system inertia.

To counteract the decline in system inertia, fast-frequency support through virtual inertia emulation has been proposed. These strategies use ESSs to inject/absorb power into/from the power system in response to a frequency event much like the inertial response from a synchronous generator. When deploying such strategies, an energy

reserve is required to emulate the inertial behavior. This could come in the form of ESSs and/or curtailed operation of RESs [97]. For a system operator, accurate knowledge of the inertial and damping behavior of the system is required to coordinate appropriate control strategies and protection schemes. Furthermore, it is also imperative for the system operator to have enough reserves in place for any plausible contingency in the system [98]. Situational awareness regarding the inertial response available in the system is critical information for the system operator.

3.1 Previous Work on Inertia Estimation

Most methods proposed in the literature for inertia estimation are offline (post-event), developed for large interconnected power systems [93], [99]–[102]. In these methods, the data from large disturbances in a power system are logged and, after significant signal-processing used to estimate the inertia constant. For example in [99], the inertia constant of the system is estimated by solving the swing equation based on the frequency transient measurements. A polynomial approximation with respect to time is applied to the transient frequency measurements to isolate the oscillations and noise in the measurement. The damping of the system has been neglected in this approach. Furthermore, these techniques are known to be susceptible to the identification of the exact time of frequency event onset and the order of the polynomial approximation [100]. System identification approaches using ambient frequency measurements have also been developed [93], however, these techniques require computationally expensive offline processing to extract the explicit value of the inertia constant. Although beneficial in traditional-synchronous generation based power systems, offline estimation approaches

are not suitable for real-time adaptive control systems/protection schemes as the information may arrive late. Furthermore, there may be cases where the system operator does not provide enough visibility/information regarding the inertial response of all the sources in the power system. For the stochastic and low-inertia nature of future power systems, online estimation of system inertia and damping constants is essential.

Several online approaches have been presented in the literature. Online estimation of system parameters such as inertia and damping of the power system provides insights into designing adaptive control systems and protection systems, such as UFLS [103]. Moreover, this allows system operators to optimize the resources to maintain the reliability and resiliency of the power system [98]. An online technique using frequency measurements from phasor measurement units (PMUs) was proposed in [104]. The proposed method again uses the swing equation as the basis to determine the inertia constant. A sliding window-based approach is utilized to filter the noisy measurements. In [105], online identification of inertia response of a system is performed using a system identification approach on PMU recordings. Statistical methods based on Markov Gaussian models have also been explored, but they require significant offline training and calibration [94].

3.2 Chapter Objectives and Contributions

In the case of microgrids, PMU measurements may not be readily available; hence, a technique that depends on local measurements is required. The main contribution of this chapter is the design of an online inertia estimation technique for ESSs deployed in low inertia microgrids to provide the ESS system operator with situational awareness of the

inertial response of the microgrid. The proposed technique utilizes an MHE approach that relies only on local measurements from a PLL of an ESS. A non-intrusive active power excitation signal is used to induce small changes in the frequency of the microgrid. Even under significantly noisy PLL measurements, it is demonstrated that the proposed technique can estimate the time-varying system inertia and damping constant. Inertia estimation using the proposed technique may have wide applications in –

- Adaptive frequency support mechanisms and protection system design,
- Offline tuning of existing control strategies,
- Design of novel control strategies for fast-frequency support, and
- Stability analysis of low inertia power systems.

3.3 Modeling of Microgrid Frequency Dynamics

The objective of this section is to develop a simple-predictive model that defines the microgrid system dynamics due to changes in the ESS power output. The simplified model makes several simplifying assumptions and is not a comprehensive representation of microgrid system dynamics. Such an approximate model is desired for the MHE/MPC to reduce computational cost and ensure optimization convergence. Both the MHE and the MPC are formulated as quadratic programs (QP) which ensures convexity and allows the use of an efficient solver for the optimization problems [106]. All the simulation results are later validated using the detailed microgrid system dynamic models.

We consider that rotational generation is the main power source and the renewable generators supplement the power demand. This allows the frequency dynamics to be

modeled using the swing equations based on the concept of an *equivalent generator* [107]. The frequency dynamics of the entire microgrid (possibly with several generators) can thus be represented with a single *equivalent generator* with appropriate parameter approximation. One can then estimate the inertia and damping constant of this equivalent generator to estimate the overall inertia and damping constant of the microgrid.

3.3.1 Frequency Event Characterization

A power imbalance causes the system frequency to deviate from its steady-state value. Figure. 3.1 shows the typical frequency evolution of a power system in response to a frequency event. In this case, when the net electrical load in the system increases (or a loss of generation occurs), the frequency drops as the mechanical power from generators takes time to counteract the imbalance. The initial ROCOF depends on the inertial response of the system [108]. In isolated power systems, the system inertia can be particularly low and cause large ROCOF that may trigger frequency relays, which can cut-off power system components [96]. Based on the magnitude of the initial ROCOF, the frequency reaches a nadir ω_{nadir} after time t_n from the start of the frequency event. The maximum ROCOF is denoted by $\dot{\omega}_{max}$ in Figure. 3.1. Hence, during the initial few seconds, the inertial response of the power system is responsible for minimizing the frequency deviation in the system until the frequency control mechanisms bring the frequency back to normal values. The time taken for the frequency to return to its steady-state value is defined as the recovery/settling time.

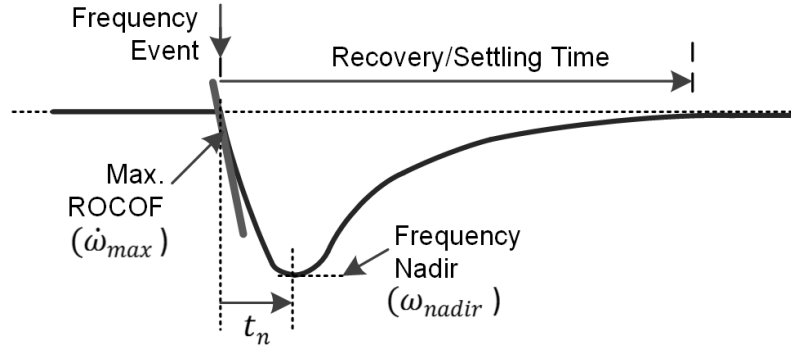


Figure 3.1. Characterization of power system frequency after an event.

3.3.2 Inertia and Damping Constant

When subjected to a disturbance, the generators in a microgrid experience small variations over an average frequency. The average frequency is defined for the center of inertia of the system as follows:

$$\omega = \frac{\sum_{i=1}^n H_i \omega_i}{\sum_{i=1}^n H_i} \quad (3.1)$$

where n represents the total number of generators in the microgrid, H_i represents the inertia constant of the i^{th} generator, and ω_i is the angular frequency of the i^{th} generator.

Similarly, the total inertia constant of the system H can be defined as:

$$H = \frac{\sum_{i=1}^n H_i S_i}{\sum_{i=1}^n S_i} \quad (3.2)$$

where S_i is the apparent power rating of the i^{th} generator. To model the frequency dynamics of an isolated microgrid system, a multi-machine system can be modeled by a single equivalent generator as shown in Fig. 3.2 [58]. The linearized swing equation of microgrid frequency dynamics is given by [58]:

$$M\Delta\dot{\omega} + D\Delta\omega = \Delta P_m - \Delta P \quad (3.3)$$

where $\Delta\dot{\omega}$ is the ROCOF, M is the equivalent system inertia constant, D is the equivalent system damping constant. Similarly, ΔP_m and ΔP are the change in the total mechanical power and the ESS power output in per unit (p.u.). The net load change ΔP_l is assumed to be a disturbance from the point-of-view of the ESS unit. Also, as this is an isolated microgrid the tie-line power flows are not modeled [20].

3.3.3 Modeling of the Frequency Control Loops

The typical frequency control loops in an isolated power system are shown in Figure. 3.2. The primary frequency control is implemented through governors in the system to stabilize the frequency change. The secondary frequency controller then removes the steady-state error as described in [58]. The type of governor and the dynamics of the turbine itself affect the dynamics of the frequency response of the system. It is assumed that in general the turbine-governor dynamics and the secondary control loop can be represented by the following set of differential equations [109]:

$$T_g\Delta\dot{P}_m + \Delta P_m = -R^{-1}\Delta\omega + \Delta P_s \quad (3.4)$$

$$\Delta P_s = -K_i\Delta\delta \quad (3.5)$$

where T_g is the turbine-governor time constant of the aggregated generators, R is the aggregated droop constant, K_i represents the integral gain of the secondary control loop, ΔP_s is the secondary power which models the equivalent effect of AGC in the system, and

$\Delta\delta$ is the integral of the rotor speed of the equivalent generator. The turbine-governor dynamics model used may be more complex if the system is dominated by other generation types. The proposed estimation technique remains equally applicable to other modeling assumptions.

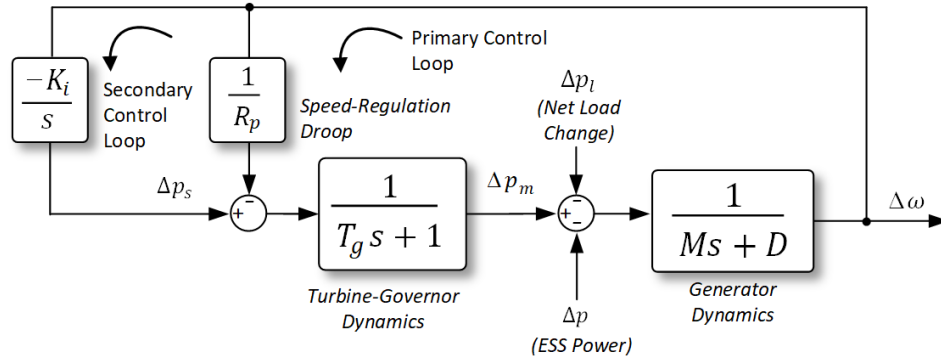


Figure 3.2. Block diagram of the isolated power system.

Based on (3.3), (3.4), and (3.5) the following differential equation describing the overall frequency dynamics of the isolated power system can then be derived:

$$\Delta\ddot{\delta} = -\left(\frac{D}{M} + \frac{1}{T_g}\right)\Delta\ddot{\delta} - \left(\frac{D}{MT_g} + \frac{1}{R_p MT_g}\right)\Delta\dot{\delta} - \frac{K_i}{MT_g}\Delta\delta - \frac{1}{MT_g}\Delta P - \frac{\Delta\dot{P}}{M} \quad (3.6)$$

If the derivative term of the input $\Delta\dot{P}_e$ is neglected, the state-space representation of the differential equation is given by:

$$\dot{x} = Ax + Bu \quad (3.7)$$

$$y = Cx + \eta \quad (3.8)$$

where

$$\dot{x} = \begin{bmatrix} \Delta \dot{\delta} \\ \Delta \dot{\omega} \\ \Delta \dot{\omega} \end{bmatrix}, \Delta u = \Delta P$$

and,

$$A = \begin{bmatrix} 0 & 1 & 0 \\ 0 & 0 & 1 \\ -\frac{K_i}{MT_g} & -\left(\frac{D}{MT_g} + \frac{1}{R_p MT_g}\right) & -\left(\frac{D}{M} + \frac{1}{T_g}\right) \end{bmatrix}$$

$$B = \begin{bmatrix} 0 \\ 0 \\ \frac{-1}{MT_g} \end{bmatrix} \quad C = \begin{bmatrix} 1 & 0 & 0 \\ 0 & 1 & 0 \\ 0 & 0 & 1 \end{bmatrix}$$

The measurement noise is represented by η . The derivative term in (3.6) is neglected to simplify the predictive model to be used by the MHE and the MPC framework. As only an approximate predictive model is required, this assumption does not significantly impact the performance of the proposed control framework.

3.4 Moving Horizon Estimation and Problem Formulation

In this chapter, the *a priori* model described in Equation (3.8) is used, combined with online measurements for frequency and ROCOF from a PLL of an ESS to identify the equivalent inertia and damping constant of the system. There are various approaches to perform state and parameter estimation of dynamic systems such as Kalman filters and extended/unscented Kalman filters [110], [111]. Most of these techniques make an assumption on the noise distribution of the measurement signals. Particle filters have also

been widely discussed for online state and parameter estimation of dynamic systems. Particle filters are known to be sensitive to errors in the initial guess, and thus may have larger convergence times [112]. Furthermore, if there are physical constraints on the estimated parameters these techniques lose their theoretical framework [113]. In this section, the fundamental concept of MHE is first introduced. This is followed by the problem formulation when implementing MHE for inertia and damping constant estimation.

3.4.1 Concepts of Moving Horizon Estimation

MHE is an online optimization-based estimation technique. In MHE, past measurements are collected over a finite horizon and then the state and parameters at the current sampling time are estimated based on minimizing a cost-function while satisfying the constraints on the states and the parameters. Several related work [112], [114]–[117] show the wide applicability of MHE in linear and non-linear systems. Recent advances in efficient algorithms and computational advances have made real-time implementation of these dynamic optimization problems feasible [113], [118], making MHE suitable for embedded applications. The concept of MHE is illustrated in Figure. 3.3. The crosses (\times) represent the measurements taken from the system while the circles (\circ) are the predicted system output based on a predictive model. A measurement window of fixed length L is shifted one-step ahead in each sample time. At the initialization stage, the window is initially empty so the window starts to move once the appropriate amount of data is collected. Now, in each sample time, an optimization problem is solved to estimate the state and parameters at the current sampling time. This is done by minimizing a

cost-function that is formulated to minimize the error between the measurements and the predicted output. As the window moves forward, the newest measurement is incorporated into the estimation window while the oldest measurements are removed. The moving window allows the MHE to approximate a full-information estimator [113] while maintaining computational tractability.

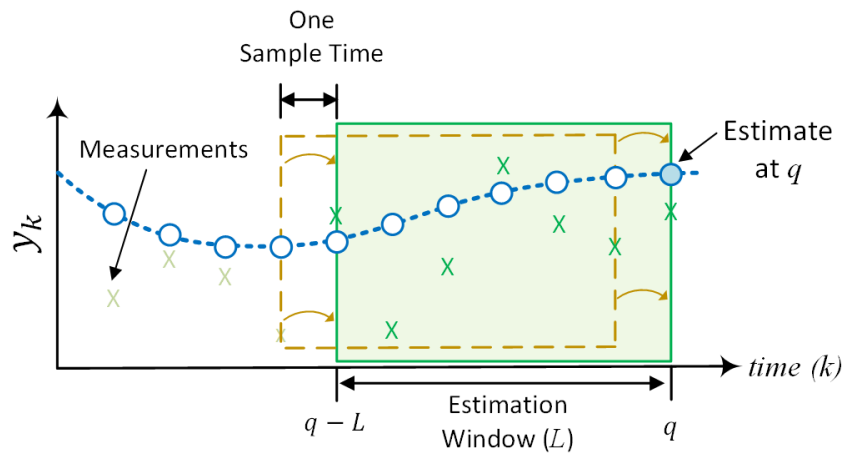


Figure 3.3. Basic concept of moving horizon estimation.

3.4.2 Formulation of Moving Horizon Estimator

The MHE which will be implemented in an ESS is formulated in this section. Let us define L as the backward time-horizon and $x_k = [\Delta\delta_k \ \Delta\omega_k \ \Delta\dot{\omega}_k]^\top$ as the states of the system and y_k as the measured output at the discrete-time instant k , the MHE problem will take the following form:

$$\underset{\hat{x}, \Delta \hat{p}, \hat{M}, \hat{D}}{\text{minimize}} J_L := \sum_{k=q-L}^q (C_d \hat{x}_k - y_k)^\top V (C_d \hat{x}_k - y_k) + \sum_{k=q-L}^{q-1} (\Delta \hat{p}_k - \Delta p_k)^\top W (\Delta \hat{p}_k - \Delta p_k) \quad (3.9a)$$

subject to

$$\hat{x}_{k+1} = A_d \hat{x}_k + B_d \Delta \hat{p}_k \quad \forall k \in \{q-L, \dots, q-1\} \quad (3.9b)$$

$$M^{\min} \leq \hat{M} \leq M^{\max} \quad (3.9c)$$

$$D^{\min} \leq \hat{D} \leq D^{\max} \quad (3.9d)$$

where J_L is the cost-function to minimized, y_k is a vector representing the measured states. The measured power output (the excitation signal injected by ESS) is denoted by \tilde{p}_k while $\Delta \hat{p}_k$ represents the estimated power output from the ESS unit. The discretized state-space matrices A_d , B_d , and C_d are obtained using the Zero-Order Hold (ZOH) method. The output matrix is defined as $C_d = \text{diag}(1, 1, 1)$. Constraint (4.2b) defines the predictive model used by the MHE while constraints (4.2c) and (4.2d) limits the search range of the estimates to realistic values.

The cost function consists of two terms weighted by matrices V and W . The matrix V is defined as follows:

$$V = \begin{bmatrix} 0 & 0 & 0 \\ 0 & V_{22} & 0 \\ 0 & 0 & V_{33} \end{bmatrix} \quad (3.10)$$

The matrix W has only one term as there is only a single input. The first term in the cost

function J_L penalizes the difference between the measured outputs and the predicted outputs using the elements V_{22} and V_{33} of the weighting matrix V . Similarly, the second term accounts for actuation errors [119]. Solving this optimization problem at each sampling time yields the state estimates \hat{x}_k and parameter estimates \hat{M} and \hat{D} . The MHE estimator also yields $\Delta\hat{p}_k$ which is the estimated power output from the ESS.

3.4.3 Implementation of Moving Horizon Inertia Estimator

The MHE is implemented using the ACADO Toolkit for MATLAB [120]. ACADO for MATLAB is an open-source toolbox that provides a general framework to implement dynamic optimization problems such as MHE. The flowchart presenting the online estimation procedure is shown in Figure. 3.4. Every time a new estimate is desired the microgrid frequency dynamics are excited using an excitation signal Δp_k (a pulse train signal). The frequency of acquiring these new estimates will depend on the application. Once the time horizon L and the sampling time is defined, the MHE samples the frequency and ROCOF measurements from the PLL of the ESS at each sampling instant during excitation. The MHE does not produce an estimate until the first L data points are collected. After the first L data-points, any new subsequent data point is fed into the estimator while the oldest measurement is neglected. The MHE solver is then implemented to estimate the true states (the frequency and the ROCOF) and the parameters (the inertia and the damping constant). In subsequent iterations, the latest estimate is used as the initial guess of the state and the parameters for that particular time instant. This is done as ACADO uses an iterative solver that converges faster with an accurate initial guess.

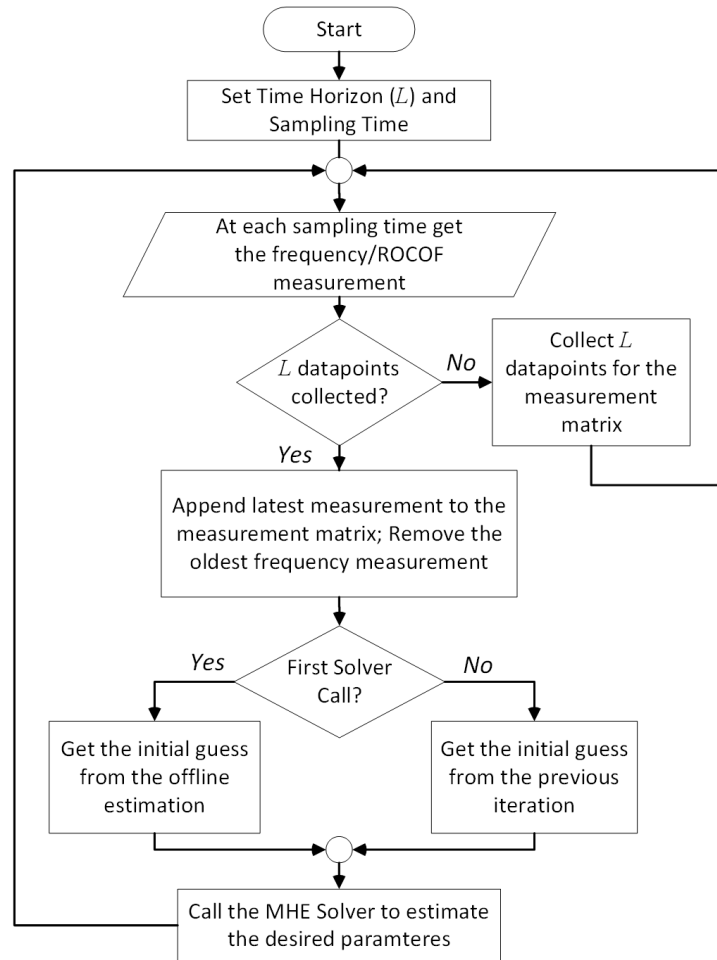


Figure 3.4. Flowchart representing the procedures for online moving horizon estimation with ACADO Toolbox.

3.5 Simulation Setup

3.5.1 Simulation Benchmark

We consider a power system that is modeled based on the description provided in Section 3.3. The setup used for the simulation case study is shown in Figure. 3.5 and was implemented in MATLAB/Simulink. Table 3.1 specifies the parameters that were used for the simulation. These are typical parameters for a power system as described in [58]. An excitation signal Δp_k is used to perturb the frequency of the system. A pulse train with an amplitude of 0.1 p.u and a frequency of 0.5 Hz is used as shown in Figure. 3.6. This

excitation signal can be generated from the ESS where the proposed estimator will be implemented. The amplitude of the excitation signals also has an impact on the performance of the estimator. In this case, for the level of noise considered in the measurements, a pulse train of amplitude 0.1 p.u. (i.e., 10% of the total size of the system) was found to be sufficient. Reducing the amplitude below 10% of the microgrid size deteriorates the parameter estimates, especially as the noise on the measurement increases. This pulse train limited the frequency deviations to 4×10^{-3} p.u. (0.240 Hz) and the maximum ROCOF to 0.012 p.u./s (0.72 Hz/s) as shown in the bottom two plots of Figure. 3.6. These variations under a controlled environment are acceptable in microgrids [22].

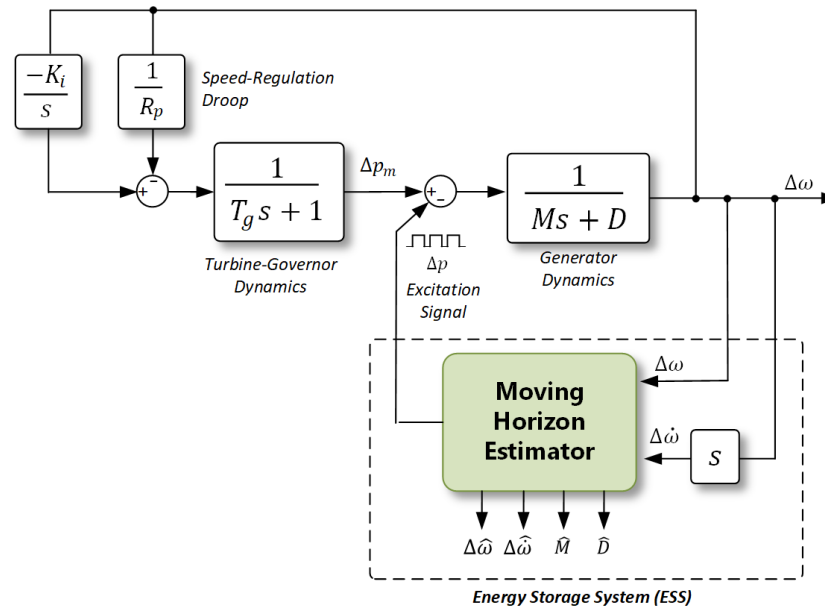


Figure 3.5. Simulation setup used in MATLAB/Simulink. The moving horizon estimator is implemented using ACADO Toolkit.

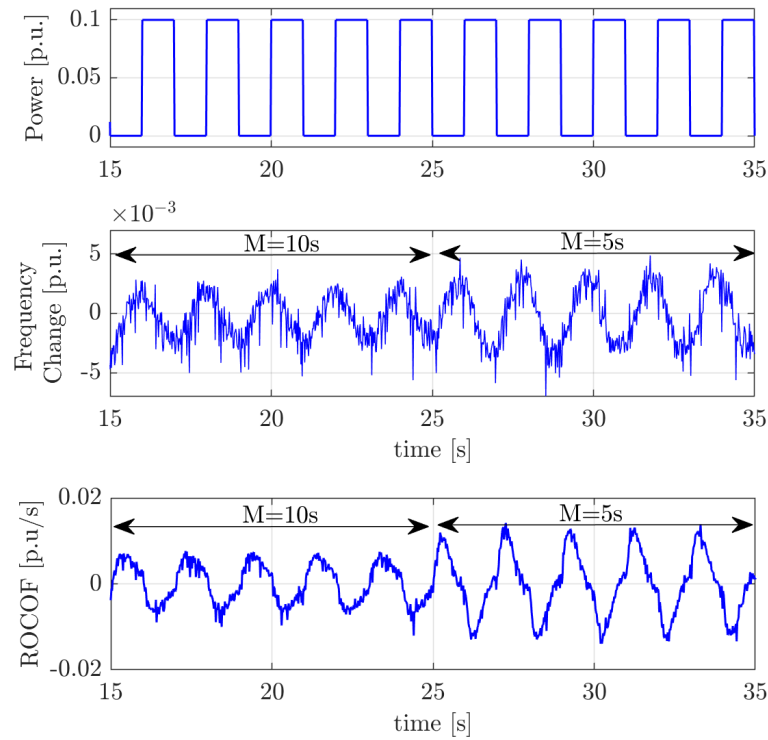


Figure 3.6. A snapshot of the excitation signals used to perturb the system frequency along with corresponding changes in frequency and ROCOF. The inertia constant of the system is assumed to change from 10 s to 5 s at a simulation time of 25 s.

It is assumed that a PLL is used to measure the signals $\Delta\omega_k$ and $\Delta\dot{\omega}_k$. For the size of the power systems considered, the measurements at any one location are sufficient as the observed inertia constant would remain relatively the same regardless of the measurement point. The measurements from the PLL are typically quite noisy especially in low-voltage microgrid systems due to factors such as unbalanced operations, harmonics. Hence, to check the performance of the MHE under noisy measurement conditions, different types of measurement noise are added to these signals. There has been no consensus on the measurement noise distribution of PLLs and PMUs in the literature. Different studies provide inconclusive evidence on the suitable distribution to be used for estimation approaches [121], [122]. Thus, the proposed technique is tested under different noise

characteristics. First, the performance of the algorithm is validated when there is no measurement noise. Then, the performance of the technique is also tested for noise with different amplitudes and distribution characteristics. The signals $\Delta\omega_k$ and $\Delta\dot{\omega}_k$ are the inputs to the MHE solver along with the excitation signal Δp_k . Based on these local measurements from the PLL the MHE solver generates the frequency estimate $\Delta\hat{\omega}_k$, the ROCOF estimates $\Delta\hat{\dot{\omega}}_k$ along with estimates for the inertia constant \hat{M} and damping constant \hat{D} of the power system.

Table 3.1. Summary of Simulation Parameters

Parameter	Values
Inertia constant (M)	10 s
Damping coefficient (D)	1.5%
Speed regulation droop (R_p)	5%
Turbine-Governor time constant (T_g)	0.2 s
Sample time	0.02 s

3.5.2 Setup for the MHE using ACADO

The MHE was implemented using the ACADO toolkit. The ACADO toolkit generates a MEX (Matlab Executable File) that can be used to call the MHE solver at every sampling instant within the Simulink environment. The following setting was used when implementing the MHE solver based on the formulation described in Equation (4.1). The matrices defining the system dynamics A_d and B_d in constraint (4.2b) are obtained based on the system parameters defined in Table 3.1. These are discretized matrices obtained by applying a zero-order hold method on the A and B matrices described in Equation (3.8) and using a sampling time of 0.02 s. The dynamics of the parameters are assumed to be constant within a relatively short sampling time of 0.02 s as defined by

constraint (4.2c). Finally, constraint (4.2d) is used to limit the search range of the parameter estimates to realistic values. In the particular case, it is assumed that the inertia constant m lies between 1 s and 20 s while the damping constant d can vary between 0.5% and 2%. The weighting matrix V is set based on the co-variance of the measurement noise. If g represents the co-variance of the measurement noise on the states, the weighting matrix is to $V = \text{diag}(0, g^{-0.5}, g^{-0.5})$. The weighting matrix W , is set to a value of 1000 as excitation signal is not expected to have significant actuation errors. This ensures that there is a relatively higher weight on the noise that is expected to be small in the cost-function. This ensures that all the terms in the cost-function contribute relatively equally to the optimal value and badly scaled problems can be avoided. The final parameter that needs to be set is the backward time-horizon L . The selection of this parameter depends on the time-scale of the dynamics of interest (in this case the inertial response of the system) and the amount of noise in the measured signals, which will be discussed in the subsequent sections.

3.6 Results and Analysis

The performance of the MHE is first evaluated assuming that there is no noise in the measurement signals. Figure. 3.7 shows the performance of the MHE when estimating the inertia and the damping constant of the system. Initially, the inertia constant of the system is 10 s and the damping constant is 1.5%. It is assumed that these are unknown quantities. The inertia constant of the system is changed from 10 s to 5 s at a simulation time of 25 s while the damping constant remains constant throughout the simulation. The change in inertia could be a result of a generation loss in the microgrid or a rotational generator

going off and being supplemented by a PV system without any inertial response. The initial guesses supplied to the online estimator were -2 s for \hat{M} and 2% for \hat{D} . The backward time-horizon L was set to 25 samples (0.5 s) in this case. Once initialized, the MHE waits for 25 samples before providing the first estimate. The MHE then estimates the true value within 3–4s. The MHE was able to estimate both the inertia and damping constant accurately when there was no measurement noise involved. When the inertia constant of the system changes to 5 s at the simulation time of 25 s, the MHE estimates the new value fairly quickly within 2-3 s. During this time, there is a slight error in the damping constant, but the MHE converges back to the true estimate within 3 s. Thus the MHE was able to estimate a drastic change in the inertia constant within 3 s. This illustrates the applicability of the proposed method in real-time control of ESS for fast-frequency services.

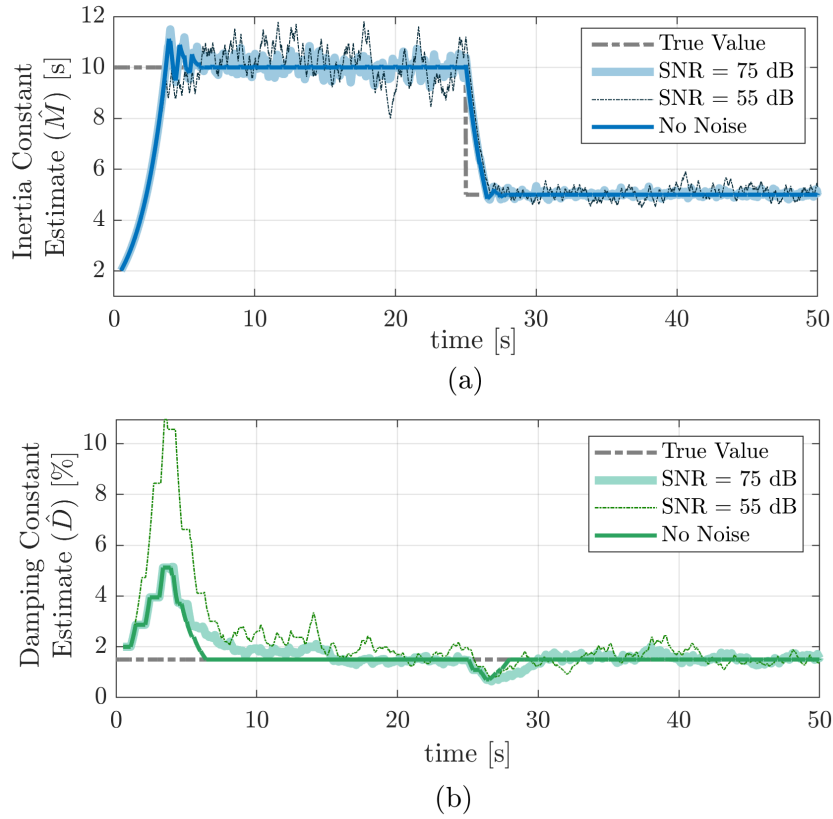


Figure 3.7. Inertia constant and damping constant estimate along with the true values for different levels of measurement noise. The noise distribution is assumed to be Gaussian.

The root mean square error (RMSE) is calculated to quantify the accuracy of the estimates. The RMSE is computed as follows:

$$RMSE = \sqrt{\frac{1}{n} \sum_{i=1}^n (\gamma_i - \hat{\gamma}_i)^2} \quad (3.11)$$

where n denotes the total number of data-points, γ_i and $\hat{\gamma}_i$ are the true and estimated values of the parameters. For the different simulation cases illustrated in Figure 3.7 the RMSE is listed in Table 3.2. For both parameter estimates \hat{M} and \hat{D} , two sets of RMSE values are reported (first when $M = 10s$ and second when $M = 5s$). In the first case (Set 1), the

RMSE is calculated between a simulation time of 10 s and 20 s. Similarly in the second case (Set 2), the RMSE is calculated over the data between 30 s and 40 s. The RMSE increases when there is an increase in the noise levels (decrease in the signal-to-noise ratio (SNR)). For $SNR = 55dB$, increasing the time-horizon to 50 resulted in a significant reduction in RMSE. In all three cases, the RMSE is reduced (indicating improved estimates) for Set 2 compared to Set 1. This is because when the inertia constant of the system was reduced to 5s the excitation signal caused larger changes in the frequency and ROCOF.

Table 3.2. RMSE for Different Noise Levels

Simulation Cases	Set 1: 10 s- 20 s		Set 2: 30 s- 40 s	
	\hat{M}	\hat{D}	\hat{M}	\hat{D}
SNR = 75 dB (L = 25)	0.255	0.272	0.079	0.162
SNR = 55 dB (L = 25)	0.819	1.523	0.227	0.471
SNR = 55 dB (L = 50)	0.715	0.739	0.179	0.391

3.6.1 Estimation with Gaussian Noisy Measurements from PLL

In this case, the performance of the MHE is evaluated in the presence of measurement noise from the PLL. Initially, it is assumed that the measurement noise has a Gaussian distribution. The performance was evaluated for different noise levels. Measurement noise that had a mean of 0 and different levels of co-variance was added to the measurements. The performance of the estimator was tested for co-variance of $1e-8$, $1e-7$, and $1e-6$ corresponding to SNR of 75, 65, and 55 dB, respectively. These are typical SNR metrics found for PLL measurements in the literature [123]. Figure. 3.7 shows the performance of the estimator when the measurement noises correspond to SNR of 75 dB and 55 db. The estimates are compared against the case when there was no measurement

noise in the system.

In both cases, the MHE was able to track the true inertia constant of the system although with small variations around the true value. However, the variations are small and provide sufficient accuracy to be used with adaptive control and protection schemes. A closer inspection shows that increasing the noise in the measurements offsets the estimates especially in the case of the damping constant estimate. It should be noted here that the horizon time had to be increased from 25 to 50 samples when the measurement noise was increased from a SNR of 75 dB to 55 dB.

3.6.2 Effect of Estimation Time Horizon on Parameter Estimates

Next, the effect of increasing the estimation time horizon on the parameter estimates is analyzed. For this, the measurement noise from PLL was assumed to have a co-variance of $1e-7$ (SNR = 65 dB). Again, we assume the measurement noise has a Gaussian distribution. Using $L < 25$ did not provide good parameter estimates resulting in large deviations from the true values. Hence, Figure 3.8 shows the inertia and damping constant estimate starting from $L = 25$. Increasing the time horizon greatly improves the accuracy of the estimates. For instance, with $L = 25$ there are large variations in the inertia constant estimate around the true value. The damping constant estimate shows significant deviations compared to the true value. However, increasing the time horizon to 50 and 75 samples significantly improves both the inertia and the damping constant estimates. The RMSE for different time-horizons discussed in Figure 3.8 is summarized in Table 3.3. Increasing the time horizon however, increases the computation cost of the estimator. Thus a balance needs to be found on the length of the selected prediction horizon based on

the level of measurement noise and computation resources available.

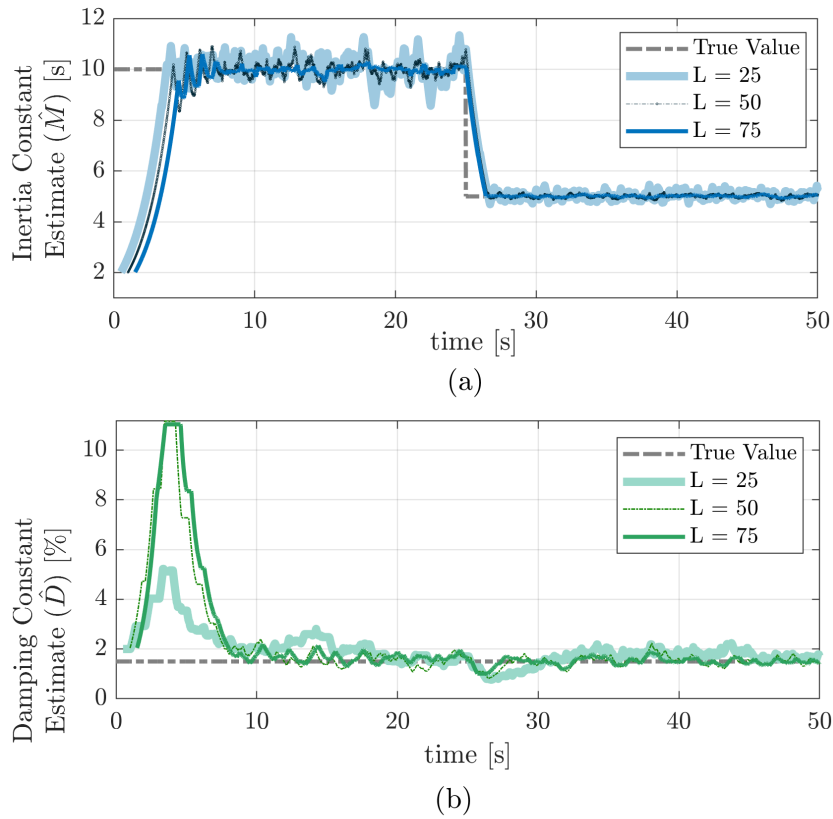


Figure 3.8. Improvement in inertia constant and damping constant estimate along with an increase in the prediction horizon.

Table 3.3. RMSE for Different Time Horizons (The SNR is 65 dB in the all cases and the measurement noise distribution is assumed to be Gaussian.)

Simulation Cases	Set 1: 10 s- 20 s		Set 2: 30 s- 40 s	
	\hat{M}	\hat{D}	\hat{M}	\hat{D}
L = 25	0.485	0.661	0.142	0.335
L = 50	0.273	0.285	0.062	0.229
L = 75	0.121	0.271	0.035	0.163

3.6.3 Estimation with Non-Gaussian Noisy Measurements from PLL

Contradicting conclusions have been made in the literature in regards to the distribution of the measurement noise from PLLs and PMUs. Furthermore, measurement

error distribution can vary through time with changes/deterioration of PTs, CTs, and change in communication channels [122]. This is where traditional estimation techniques such as Kalman filters and/or extended Kalman filters may fail. The deviation of the measurement noise distribution is characterized using the skewness and kurtosis metrics. The skewness of a dataset is defined as the measure of the lack of symmetry. A Gaussian distribution whose probability density function (pdf) is perfectly symmetrical will have a skewness of 0. If the right-hand tail of a dataset (when analyzing its pdf) is longer than the left-hand tail, then skewness is positive and negative otherwise. Similarly, kurtosis measures the combined weight of the tails relative to the rest of the distribution. Kurtosis for a Gaussian distribution is equal to 3.

In this case, the performance of the proposed estimator is evaluated for different measurement noise distributions. Figure 3.9 shows the inertia and the damping constant estimates with skewness of +1 and kurtosis of 7. The measurement noise distribution compared against a Gaussian distribution of the same mean and covariance is shown in Figure 3.9 (a). Figures. 3.9(b) and (c) show the inertia and damping constant estimation, respectively. The estimation is also compared when the estimation was performed with Gaussian distributed measurement noise. Although the MHE can still estimate the inertia and the damping constant, there is an increase in the variation in both estimates. A similar observation can be made when the measurement noise has a negative skewness in Figure 3.10. These results illustrate that the MHE performs well regardless of the distribution in the measurement noise. The RMSE for these two cases are listed in Table 3.4.

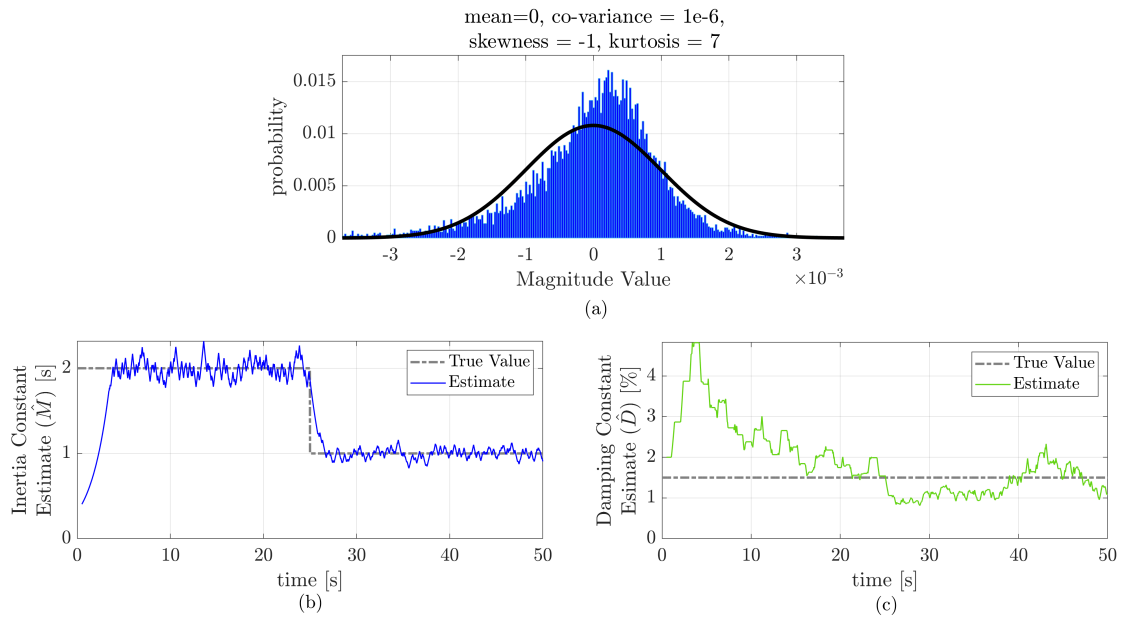


Figure 3.9. Estimates with a non-Gaussian distribution (Mean = 0, Co-variance= $1e-7$, Skewness = +1, Kurtosis = 7). (a) The pdf of the measurement noise. (b) Inertia constant estimate. (c) Damping constant estimate.

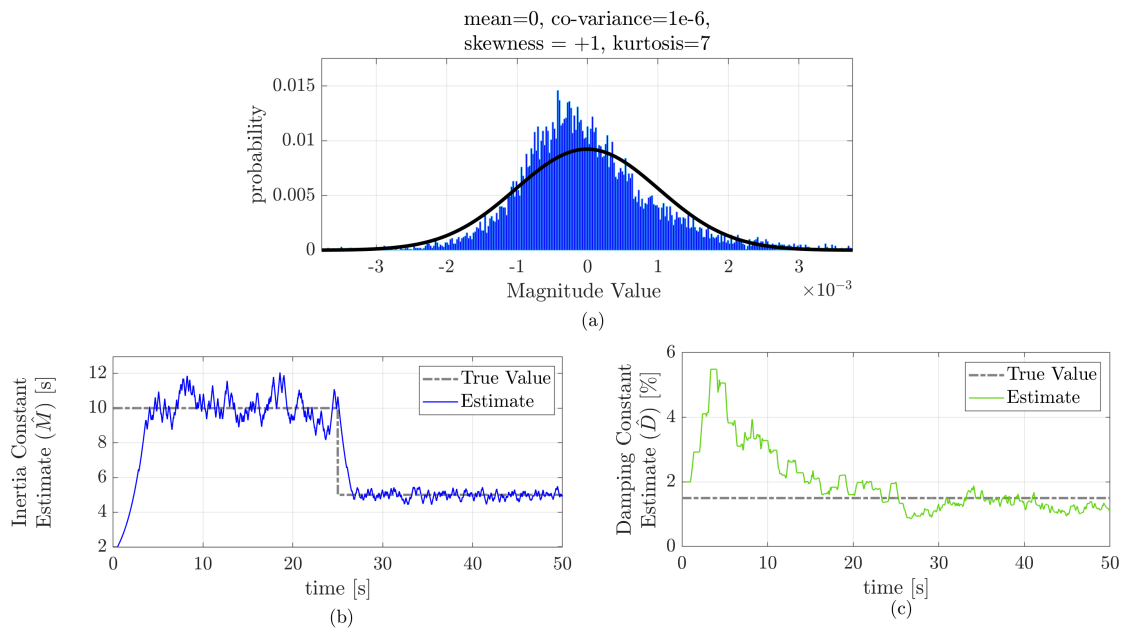


Figure 3.10. Estimates with a non-Gaussian distribution (Mean = 0, Co-variance= $1e-7$, Skewness = -1, Kurtosis = 7). (a) The pdf of the measurement noise. (b) Inertia constant estimate. (c) Damping constant estimate.

Table 3.4. RMSE when the measurement noise is assumed to be non-Gaussian

Simulation Cases	Set 1: 10 s- 20 s		Set 2: 30 s- 40 s	
	\hat{M}	\hat{D}	\hat{M}	\hat{D}
Skewness = +1, Kurtosis = 7 (SNR = 55 dB)	0.516	0.749	0.314	0.375
Skewness = -1, Kurtosis = 7 (SNR = 55 dB)	0.702	0.801	0.230	0.158

3.7 Chapter Conclusions

A technique to estimate the inertia and the damping constant of the system using a MHE was introduced. The proposed technique was able to provide the estimate in real-time for an ESS to facilitate the deployment of fast-frequency support strategies. The estimates were obtained from local noise PLL measurements. A non-intrusive excitation signal was used to perturb the frequency of the system to perform the estimates. The MHE showed good performance under typical PLL measurement noise amplitudes and distributions. Since there has not been a clear consensus on the measurement noise distribution for frequency measurements the ability of the estimator to work on different noise distributions is a major contribution. In the future, the proposed technique will be tested in a realistic benchmark. The proposed framework lays a basis for implementing adaptive frequency support which will be explored in the future.

CHAPTER 4 OPTIMIZATION-BASED FAST-FREQUENCY ESTIMATION AND SUPPORT OF LOW INERTIA MICROGRIDS

Modern microgrids are incorporating a large share of inverter-based renewable generation that in general do not provide any inertial response. As large amounts of PV and/or wind generation are integrated through power electronic inverters, the traditional rotational generation-based microgrids are being transformed into inverter-based systems [7], [124]. As a result, fast-frequency dynamics are more prevalent in such low-inertia microgrids. During frequency events, the ROCOF are large causing significant frequency deviations. This can trigger protection systems, such as UFLS, and can lead to cascaded outages throughout the system and eventually cause a total blackout. Control strategies deployed using ESSs interfaced through power electronic inverters can provide fast-frequency support for these low-inertia microgrids to maintain stability and reliability.

4.1 Previous Work on Optimal Fast-Frequency Support Strategies

Traditionally to provide fast-frequency support in low-inertia microgrids, techniques based on the derivative of the measured frequency have been proposed [108], [125]. More specifically, the power output of the ESS inverter is controlled based on the derivative of the frequency. This is referred to as *virtual inertia* in the literature as it replicates the inertial response from rotational generators in a power system. As has been shown in [97], [126], these controllers are difficult to tune and susceptible to instability due to noisy frequency measurements from PLLs. To address this issue, a number of optimal frequency control techniques have been proposed in the literature. These control techniques provide fast-frequency support by reducing frequency deviations and the ROCOF, while

minimizing the energy/power consumption.

Numerous fast-frequency support mechanisms for low-inertia power systems have been proposed in the literature [127], [128]. Techniques to optimize the performance in terms of reducing energy/power requirements for frequency support have been widely studied. Different machine learning/black-box approaches have been proposed to optimize the performance of the fast-frequency controllers. The main objective of these approaches are to reduce the frequency deviations and the ROCOF while minimizing the peak power and/or the energy usage. Several methods based on fuzzy logic [129], [130], neural networks [131], and reinforcement learning [24], [89] have been proposed. These methods can be computationally expensive and as the system parameters change, require complex re-training.

Approaches based on predictive models of the system have also been proposed, using the *swing equation* of the power system as the predictive model. A predictive controller was developed in [49] to provide dynamic frequency support using an ESS. However, the method was limited to one-sample time ahead predictions which limited the performance as the system dynamics were not captured over a longer time horizon. A technique using explicit MPC was proposed in [132] to provide frequency support. In this approach, the control actions were analytically computed offline and the control actions were limited to a lookup table, reducing the flexibility of the controller to changing system conditions. LQR techniques have also been developed in the literature [90], [109], but these approaches are limited as they do not provide the flexibility to be reconfigured online as needed and cannot handle physical system constraints.

Other techniques to improve performance use a heuristic “alternate/flexible inertia”

method where the gains of the controller are adjusted based on the acceleration of the frequency [133], [134]. Although such techniques have been shown to achieve faster settling times and reduced energy usage, they are also known to be prone to oscillations [134]. Hence, most techniques in the literature rely on black-box models or short-horizon predictions with limited flexibility to optimize the fast-frequency support mechanism. The proposed MHE-MPC framework allows for improved control flexibility and optimization over longer prediction horizons.

4.2 Chapter Objectives and Contributions

In this chapter, a flexible approach that uses MPC and MHE is formulated to enable an ESS to provide fast-frequency support. MPC allows the system operator to achieve near-optimal control actions (based on a defined cost-function) while having the ability to incorporate ESS constraints into the control framework. Additionally, the ESS operator has the flexibility to change dynamic behavior of the system by intuitive adjustment of the weighting parameters. For instance, if there are sufficient incentives in the market mechanisms, the ESS operator can select weighting parameters such that significant reduction in ROCOF is provided even at the expense of battery degradation.

MHE provides the MPC algorithm accurate estimates of the frequency and ROCOF of the system (i.e., *state*), given noisy measurements. These real-estimates facilitate control actions that avoid the oscillatory behavior observed with traditional derivative-based (virtual inertia) controllers due to interaction with PLLs. With traditional virtual inertia controllers, a LPF is used to filter out PLL measurement noise. The delay caused by the LPF is known to cause instability, especially under high controller gain

values [76]. Thus, using a LPF with low cut-off frequencies limits the controller gains and the effectiveness of the controller in providing fast-frequency support. In the proposed framework, a PLL without a LPF is used as the MHE performs the necessary filtering and prevents the aforementioned oscillatory behavior when providing fast-frequency support.

This chapter is an extension of MPC-based fast-frequency support presented in [96]. In this chapter, this framework is extended framework with MHE, and the combined framework is tested in a realistic test system from Cordova, Alaska. The contributions of the chapter are as follows:

1. Designed a fast-frequency support framework that achieves the required performance while incorporating physical constraints of the ESS.
2. Developed a flexible mechanism for an ESS operator to change fast-frequency performance based on available reserves and market requirements/incentives.
3. Improved stability performance compared to traditional virtual inertia controllers through the use of MHE.

4.3 Proposed MHE-MPC Framework

The proposed MHE-MPC framework is shown in Figure 4.1. The proposed framework consists of two distinct modules – the MHE and the MPC. The MHE performs state estimation based on noisy frequency and ROCOF measurements from a PLL. The state estimates are then used in the model of the MPC to generate control signals for the ESS. The MPC uses an approximate predictive model representing the system's frequency dynamics and generates near-optimal ESS control actions based on a defined

cost-function. The cost-function typically consists of several terms that penalize the states (frequency and ROCOF) and/or the ESS power output. By tuning weights in the cost-function, a system operator can change the dynamic performance of the controller based on the desired QoS. Additionally, physical constraints of the ESS such as peak-power limits and/or ramp-rate limits can be formulated within the MPC framework. One of the main challenges with existing fast-frequency support techniques is that a PLL must be supplemented with a LPF to account for measurement noise. The dynamics of such PLLs with LPFs can cause oscillatory behavior, especially at higher control gains, as illustrated in a number of relevant work in the literature [76], [97], [126]. The MHE module allows the use of a PLL without a LPF, thus the combined framework can prevent oscillatory response in the system.

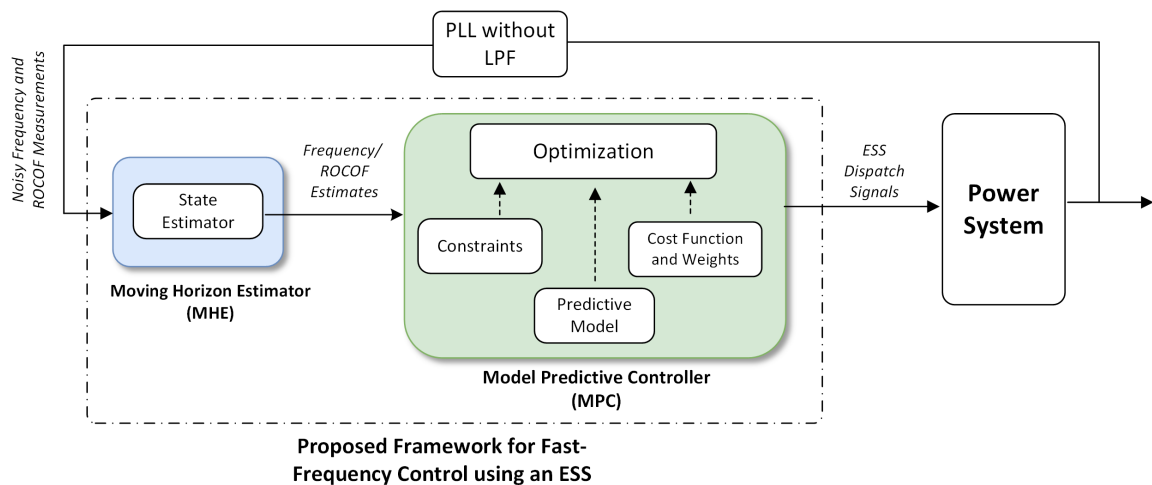


Figure 4.1. Proposed MHE-MPC framework for fast-frequency support. The MHE provides state estimates for the frequency and ROCOF from noisy PLL measurements while the MPC provides ESS control signals to provide fast-frequency support.

The frequency dynamics model derived in Section 3.3.3 will be used as the predictive model. Both the MHE and the MPC is formulated as a quadratic program (QP) problem which ensures convexity and allows the use of a simple solver for the

optimization problem [106].

4.3.1 Formulation of Moving Horizon Estimation

Let us define L as the length of the backward time horizon. Also, at a discrete time instant k , $x_k = [\Delta\delta_k \ \Delta\omega_k \ \Delta\dot{\omega}_k]^\top$ defines the states of the system and y_k is the measured output. The MHE problem then takes the following form:

$$\min_{\hat{x}, \Delta\hat{p}} J_L := \sum_{k=q-L}^q (C_d \hat{x}_k - y_k)^\top V (C_d \hat{x}_k - y_k) + \sum_{k=q-L}^{q-1} (\Delta\hat{p}_k - \Delta p_k)^\top W (\Delta\hat{p}_k - \Delta p_k) \quad (4.1a)$$

subject to

$$\hat{x}_{k+1} = A_d \hat{x}_k + B_d \Delta\hat{p}_k \quad \forall k \in \{q-L, \dots, q-1\} \quad (4.1b)$$

The measured power output from the ESS unit is denoted by Δp_k . The discretized state-space matrices A_d , B_d , and C_d are obtained using the Zero-Order Hold (ZOH) method. The cost function to be minimized is J_L while V and W are the weighting matrices. The matrix V is defined as $V = \text{diag}(0, V_{22}, V_{33})$ (the element associated with the $\Delta\delta_k$ is set to zero as this is not used). The matrix W has only one term as there is only a single control signal. The first term in the cost function J_L penalizes the difference between the measured outputs and the predicted outputs using the elements V_{22} and V_{33} of the weighting matrix V . Similarly, the second term accounts for actuation errors [119] which is achieved by proper selection of the weighting matrix W . Solving this optimization problem at each sampling time yields the state estimates \hat{x}_k and the estimate

of the applied control signal $\Delta \hat{p}_k$.

4.3.2 Formulation of Model Predictive Control

Let us define T as the length of the forward time-horizon. For the MPC formulation, since the objective is to minimize the $\Delta \omega$ and $\Delta \dot{\omega}$, the states of the system for a given time instant k is re-defined as $x_k = [\Delta \omega_k \ \Delta \dot{\omega}_k]^\top$ and the matrices A_d , B_d and C_d are redefined accordingly. The proposed MPC formulation will then take the following form:

$$\min_{\Delta p} J_T := \sum_{k=q}^{q+T-1} \left(x_k^\top Q x_k + \Delta p_k^\top R \Delta p_k \right) + x_{q+T}^\top Q^f x_{q+T} \quad (4.2a)$$

subject to

$$x_{k+1} = A_d x_k + B_d \Delta p_k \quad \forall k \in \{q, \dots, q+T-1\} \quad (4.2b)$$

$$|\Delta p_k| \leq P_{max} \quad \forall k \in \{q, \dots, q+T-1\} \quad (4.2c)$$

$$\|\Delta p_{k+1} - \Delta p_k\|_\infty \leq E \quad \forall k \in \{q, \dots, q+T-1\} \quad (4.2d)$$

where J_T is the cost-function to be minimized, and Q and R are the weighting matrices corresponding to the state estimates and the control signal respectively. The weighting matrix Q is defined as $Q = \text{diag}(Q_{11}, Q_{22})$. The element Q_{11} is used to penalize change in frequency, and the element Q_{22} is used to penalize the ROCOF. The matrix R is used to penalize the control effort (i.e., the power output from the ESS). The R matrix in this case has only a single element as ESS output power is the only control action. Similarly, Q^f is a terminal cost weighting matrix. We assume that Q^f is equal to Q throughout the chapter. More details on the choice of the terminal cost and time-horizon can be found in [135]. At

each discrete time instant k , the first element obtained from solving the optimal control problem over the forward time-horizon is applied to the system. The system dynamics are incorporated within the constraint (4.2b) of the above MPC formulation. Similarly, (4.2c) limits the power output of the ESS to P_{max} . The ramp-rate of the ESS power output is limited to E by (4.2d).

4.4 Simulation Setup

4.4.1 Benchmark

To test the proposed control framework, the remote microgrid test system from Cordova, Alaska, was modified as shown in Figure 4.2(a). Only two substations are considered – the ORCA 12.47 kV substation with three diesel generators (ORCA 3, ORCA 4, and ORCA 5) and the Humpback Creek 12.47 kV substation, where a 1 MW PV system is connected. The implementation of the governor and excitation systems of the generators is shown in Figure 4.2(b). The parameters used are – $R_p = 5\%$, $K_i = 20$, $T_g = 0.2s$, $R_q = 5\%$, $k_v = 0.1$, and $T_v = 0.05s$. The same parameters are used for the controllers of all three generators. Detailed parameters used to model each generator are listed in Table 4.1. All the generators are operated in droop mode. ORCA 3 provides AGC to bring the system frequency back to the nominal value after the primary control action to automatically restore the remaining generators to their scheduled values [58].

Table 4.1. Generator Parameters

	X_d	X'_d	X''_d	X_q	X''_q	X_l	T'_{d0}	T''_{d0}	T''_{q0}
ORCA 3	1.38	0.23	0.12	0.76	0.12	0.10	3.20	0.04	0.04
ORCA 4	1.38	0.23	0.12	0.76	0.12	0.10	3.20	0.04	0.04
ORCA 5	1.76	0.46	0.25	1.06	0.25	0.05	4.34	0.04	0.06

A 3 MW ESS is connected to the ORCA substation. The proposed MHE-MPC control framework is implemented on this ESS. The ESS can be utilized to perform a wide-array of grid ancillary services in different time scales, with fast-frequency support being the application discussed in this work. The inverter in the ESS is modeled using three independent current-controlled voltage sources, which allows the system to be analyzed without modeling the DC-link dynamics and/or harmonics. These dynamics are much faster than the frequency dynamics which are the main concern of this work. A PI-type-2 controller as described in [136] is used to implement the current controllers which control the output of the current-controlled voltage sources. The ESS is interfaced through an LC filter with an inductance $L_f = 10mH$ and capacitance $C_f = 3.3\mu F$. A PLL measures the change in frequency $\Delta\omega$ and ROCOF $\Delta\dot{\omega}$ for the MHE-MPC framework which then generates the reference power/current for the current controller. The PV plant is modeled as controlled current sources and has no frequency dynamics associated with it. This reduces the overall inertial response of the microgrid system.

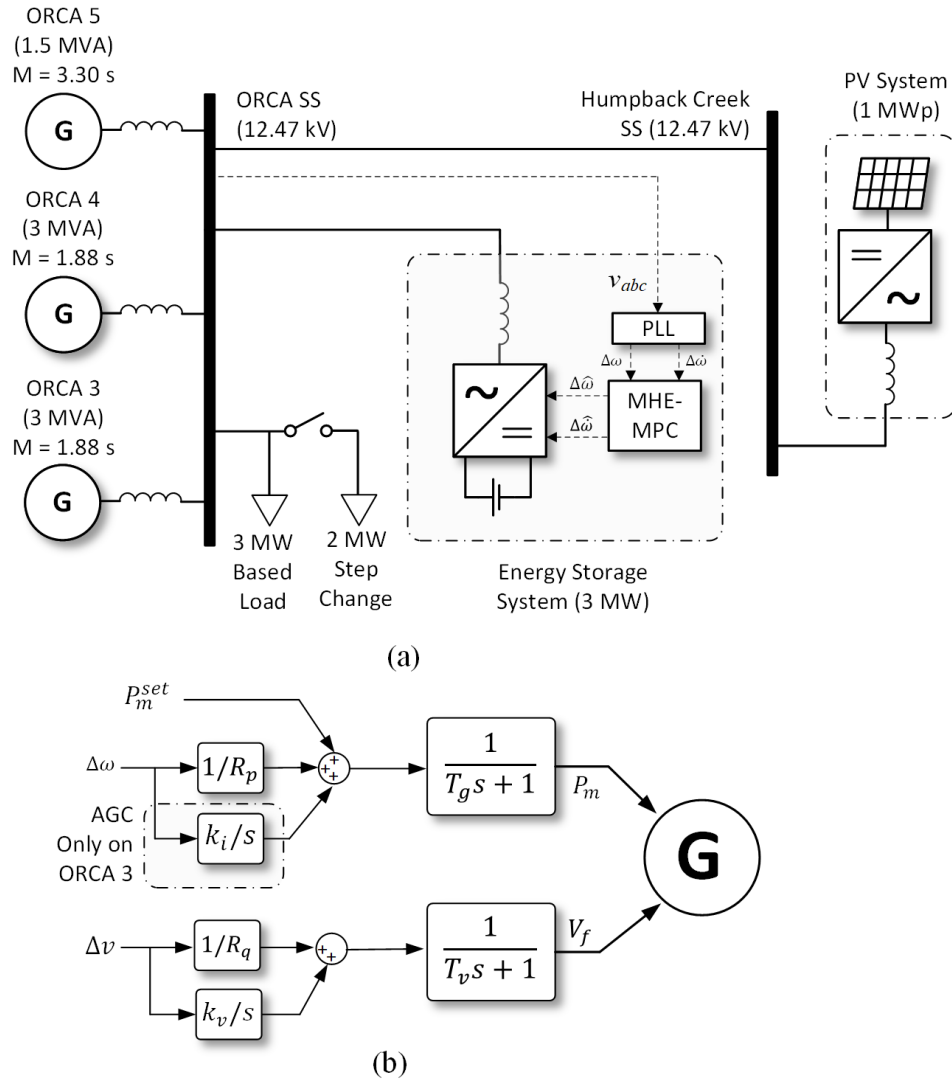


Figure 4.2. Modified test system of Cordova, Alaska.

4.4.2 Configuration for the MHE-MPC Framework

The configuration for the MHE-MPC framework is described in this section. A sampling time 0.02 s was used for both the MHE and MPC modules. For the MHE, the backward time-horizon L is set to 10 samples. This allows the MHE to track the fast changes in the ROCOF, providing accurate estimates while keeping computational cost low. It is common practice to tune the weighting matrix based on the co-variance of the

measurement noise. If g represents the co-variance of the measurement noise on the states, the weighting matrix is to $V = \text{diag}(0, g^{-0.5}, g^{-0.5})$. The weighting matrix W is set to a high value of 1000 as there is no significant difference between the control signal and the actuation signal. If there are significant actuation errors the value of W can be decreased accordingly. For the MPC module, the forward time-horizon T is set to 50 samples. For the sampling time of 0.02s, this puts the forward time-horizon at 1 s which matches the typical range of the frequency dynamics of concern in the system. The weighting matrix is varied based on the simulation analysis being performed and is described in subsequent sections.

Both the MHE and the MPC modules are formulated using the ACADO Toolkit [120] for MATLAB, which is an open-source toolbox to implement dynamic optimization problems. The test system was implemented in MATLAB/Simulink (using the Simscape Power Systems library), and the parameters for the predictive model were estimated using an offline least square estimator but could be estimated online using an approach described in Chapter 3. The ACADO Toolkit generates a MATLAB Executable file that can be called from within Simulink to implement the MHE-MPC framework to provide fast-frequency support.

4.5 Results and Analysis

In this section, the performance of the MHE in estimating the frequency deviation and ROCOF of the system is first illustrated. This is followed by analysis of the proposed combined framework, which is illustrated in terms of the operational flexibility, capability to handle ESS constraints, and performance improvement under noisy measurement

conditions. All simulation results are presented in p.u. with frequency and ROCOF normalized against a 60 Hz base while the power is normalized against a 3 MVA base. In all the cases, it is assumed that system base load is 3 MW (1 p.u.) to begin with, and there is a 2 MW (0.75 p.u.) change in the system load at 5 s.

4.5.1 Performance of the MHE

The performance of the MHE is illustrated in Figure 4.3. The measurements from the PLL are assumed to have measurement noise with a Gaussian distribution of mean 0 and co-variance 10^{-7} , equivalent to a SNR of 65 dB, which is typical for PLL measurements [123]. The PLL measurement is then fed into the MHE without any filters. The performance of the MHE is compared to the filtered frequency and ROCOF obtained from using a second-order Butterworth-type LPF with cut-off frequency f_c of 5 Hz and a damping ratio ξ of 0.707 in Figure 4.3(a).

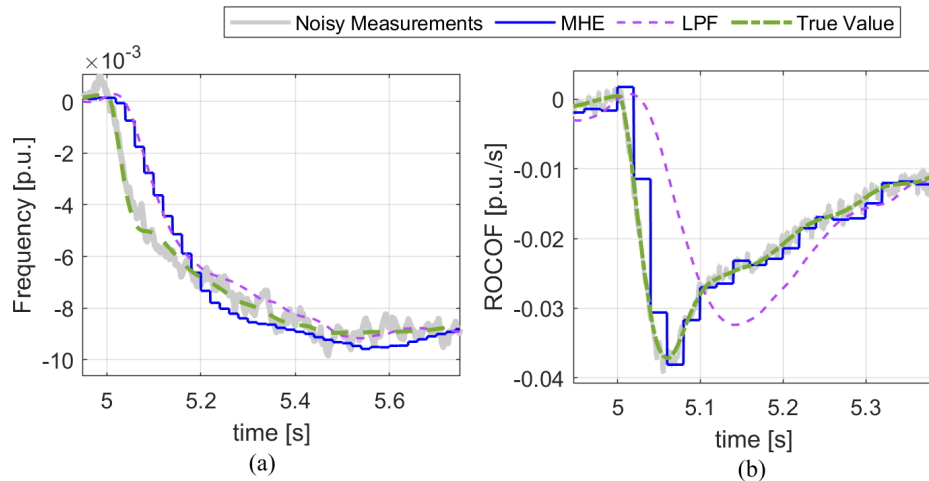


Figure 4.3. Frequency and ROCOF of the microgrid system estimated using the MHE. The estimates are compared against the noisy PLL measurements and the measurement from LPFs.

As stated earlier, a lower f_c introduces significant delay in the measurement and

makes the closed-loop system more susceptible to oscillatory behavior. This delay is critical when measuring the ROCOF, as the controller needs to detect and respond to fast changes to provide adequate fast-frequency support. A low cut-off frequency of 5 Hz is required to properly filter out noise in the frequency measurements in Figure 4.3(a), but this leads to a significant delay in the ROCOF measurement as shown in Figure 4.3(b).

The proposed MHE, however, is able to estimate both the frequency and ROCOF without significant delay. The frequency estimate has similar performance as compared to the case when using a LPF. With the ROCOF estimate, even though there is only a slight reduction in the measurement noise, the fact that there minimal delay in the estimate helps to maintain system stability. Avoiding this delay prevents oscillatory behavior in the system.

4.5.2 Performance: Operational Flexibility

The performance of the MPC in terms of providing operational flexibility for the ESS operator is illustrated here. The elements of the Q matrix, Q_{11} and Q_{22} are varied from 0.1 to 1 in steps of 0.1. Increasing Q_{11} penalizes the change in frequency $\Delta\omega$, while increasing Q_{22} penalizes the ROCOF $\Delta\dot{\omega}$. The R matrix, which penalizes the control signal, is kept constant at a low value of 0.001 so that there is only a small penalty on the control action from the MPC. The maximum frequency change, maximum ROCOF and the peak-power injected by the ESS for different weighting constants are illustrated in the heatmaps shown in Figure 4.4. Figure 4.4(a) shows that increasing Q_{11} reduces the frequency deviation in the system by a significant amount. Increasing Q_{22} at a constant value of Q_{11} , however, does not result in much variation in the frequency deviation as expected. On the other hand, increasing Q_{22} results in significant reduction in the ROCOF

as shown in Figure 4.4(b). Increasing Q_{11} and/or Q_{22} thus increases the power demand from the ESS.

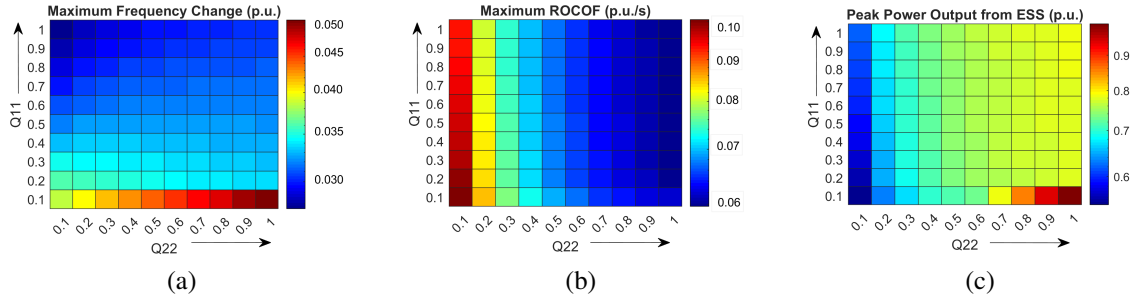


Figure 4.4. Heatmaps illustrating the variation of different system parameters based on the selection of Q_{11} and Q_{22} . (a) Maximum frequency change. (b) Maximum ROCOF. (c) Peak power output from ESS.

Figure 4.5 shows how the dynamics of the frequency, ROCOF and the ESS power outputs change depending on the selection of the weighting parameters. For the case when $Q_{11} = 0.1$ and $Q_{22} = 0.5$, since there is a higher penalty on the ROCOF deviation, a significant reduction in the system ROCOF can be observed. This, however, results in a higher peak-power output from the ESS. On the other hand, for the case when $Q_{11} = 0.5$ and $Q_{22} = 0.1$ the reduction in ROCOF is lower and thus the peak-power usage is also lower. Finally, the dynamics of the system based on variation of R is shown in Figure 4.6. When a high value of $R = 0.1$ is used, since there is a higher cost in the control, the power output from the ESS and the energy usage is limited. However, this means there is only a slight reduction in the frequency deviation and ROCOF. When the R value is reduced to 0.01 and 0.001 the power/energy usage increases and leads to higher reductions in frequency deviation and ROCOF.

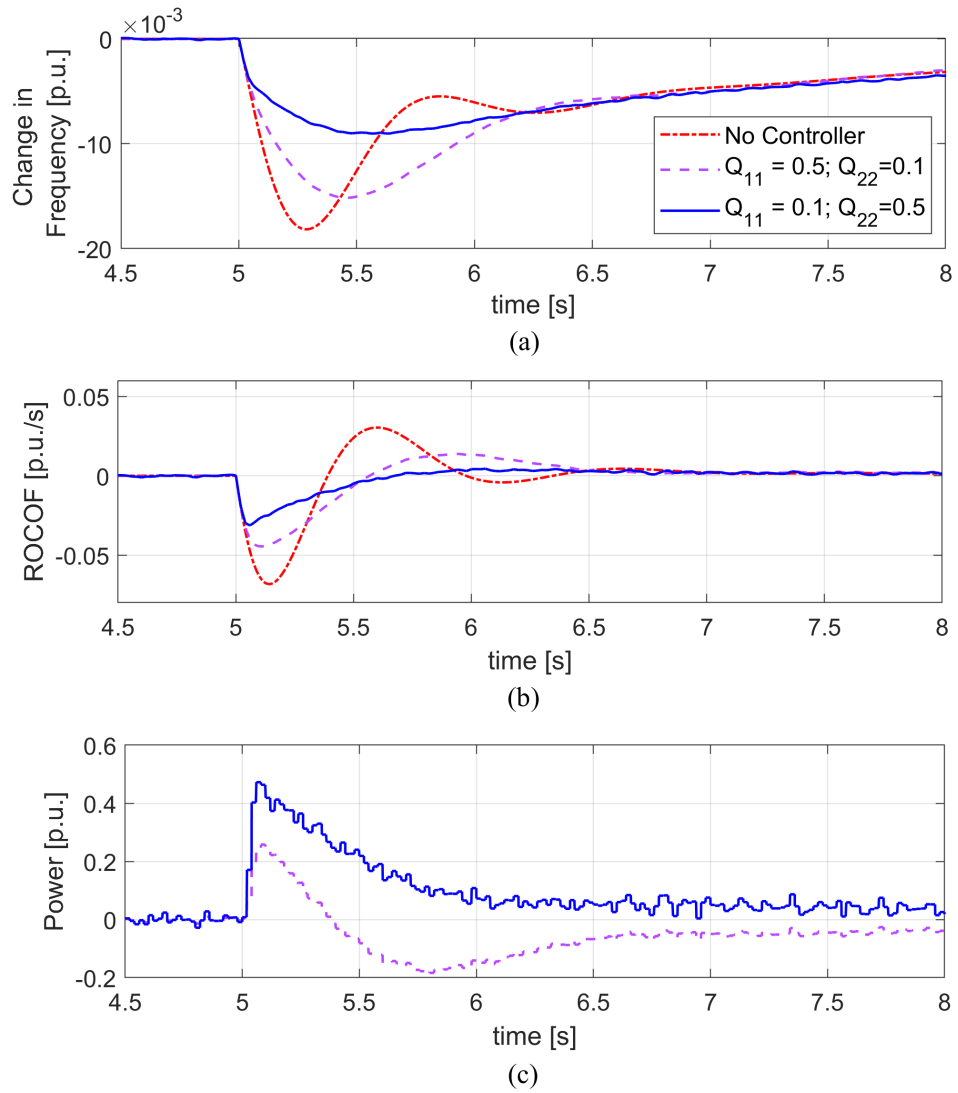


Figure 4.5. Frequency, ROCOF, and peak power output of ESS for different values of Q . (a) Change in system frequency. (b) System ROCOF. (c) Power output from ESS.

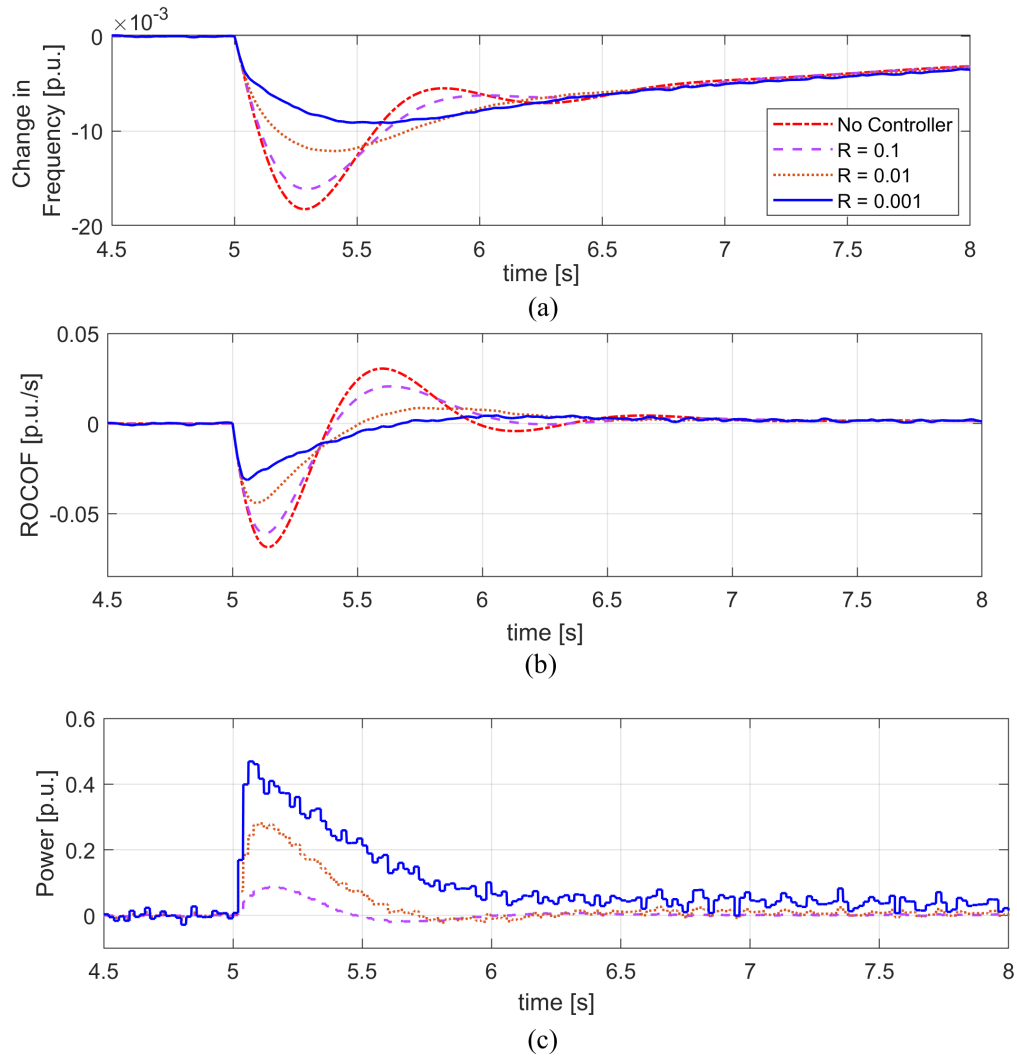


Figure 4.6. Frequency, ROCOF, and peak power output of ESS for different values of R . (a) Change in system frequency. (b) System ROCOF. (c) Power output from ESS.

The weighting parameters thus provides an intuitive mechanism for the system operator to control the frequency dynamics of the microgrid, either manually or as part of a market mechanism. Based on the ESS power availability, system inertia, and market incentives, the ESS operator can select appropriate weighting parameters. For instance, if the system inertia is particularly low at any given instance, the ESS operator can increase

Q_{22} to put more emphasis on reducing the large ROCOF that occurs in low-inertia situations to prevent large frequency transients and prevent system UFLS. Similarly, ESS operator can prevent battery degradation by controlling the R parameter. Thus, the ESS and microgrid operators can find a balance between frequency QoS (depending on the microgrid consumers) and the battery life degradation in the MHE-MPC framework. This mechanism also allows the ESS operator to deploy fast-frequency support *as a service* for the microgrid.

4.5.3 Performance: Constraints Handling

The proposed MHE-MPC framework allows the microgrid or ESS operator to impose constraints based on available resources, QoS incentives in the market, or to provide multiple market services. For this particular analysis, it is assumed that the ESS operator has limited the power output of the unit to 0.1 p.u. (0.3 MW). Figure 4.7 shows the change in frequency, ROCOF and the power output from the ESS for three cases – with no fast-frequency controller, a constrained controller, and an unconstrained controller. In all cases, the same settings were used for both the MHE and the MPC modules. For the MHE, the settings described in Section 4.4.2 are used, while for the MPC the weights are set to $Q = \text{diag}(0.1, 0.9)$.

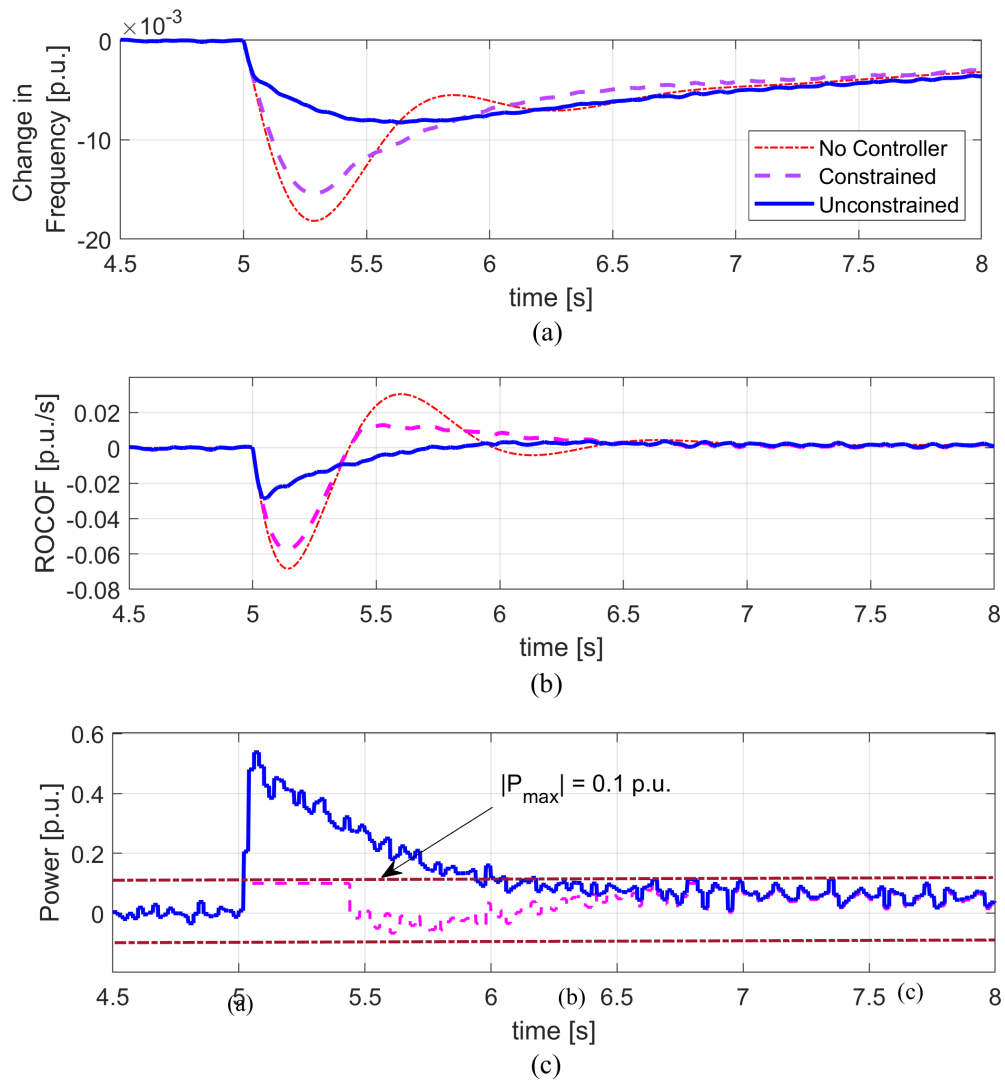


Figure 4.7. Comparison of constrained versus unconstrained system operation. The peak-power output is constrained to 0.1 p.u. in this case.

The reduction in frequency deviation is highest when there are no constraints in the formulation, as shown in Figure 4.7(a). Similarly, the ROCOF is also least for the unconstrained case as illustrated in Figure 4.7(b). However, significant reductions come at the cost of a larger peak-power injection of 0.5 p.u. (1.5 MW) from the ESS, as shown in Figure 4.7(c). Furthermore, the energy usage per frequency event is also higher. All of

these factors could degrade the ESS lifetime and impact other ESS services (e.g., arbitrage). However, with constrained operation the ESS operator can inherently include a constraint on the peak-power of the ESS within the formulation, which limits the control action generated by the MPC to 0.1 p.u. (0.3 MW) as shown in Figure 4.7(c). With peak-power limited, the reduction in frequency deviation and the ROCOF is lower compared to the unconstrained case, but this results in lower power/energy usage and longer ESS lifetime.

4.5.4 Performance: Stability Improvement

To highlight the advantage of the MHE module, two sets of simulations are carried out. In the first case shown in Figure 4.8(a) the measurements from the PLL with a LPF are used by the MPC. A second-order Butterworth-type LPF with a cut-off frequency f_c of 5 Hz is employed. The parameters of the PLL are set to $k_i^{PLL} = 92$ and $k_d^{PLL} = 4232$ [76]. In the second case, shown in Figure 4.8(b), the PLL measurements are directly fed to the proposed MHE-MPC framework. It should be noted that in Figure 4.8(b), the PLL does not include a LPF as the MHE provides the filtered estimates. For the same weighting parameters, $Q = \text{diag}(0.1, 0.9)$ and $R = 0.0001$, the frequency and the ROCOF for the two cases are shown in Figure 4.9. Due to the delay caused by the LPF, the system shows oscillatory when the MHE module is not used.

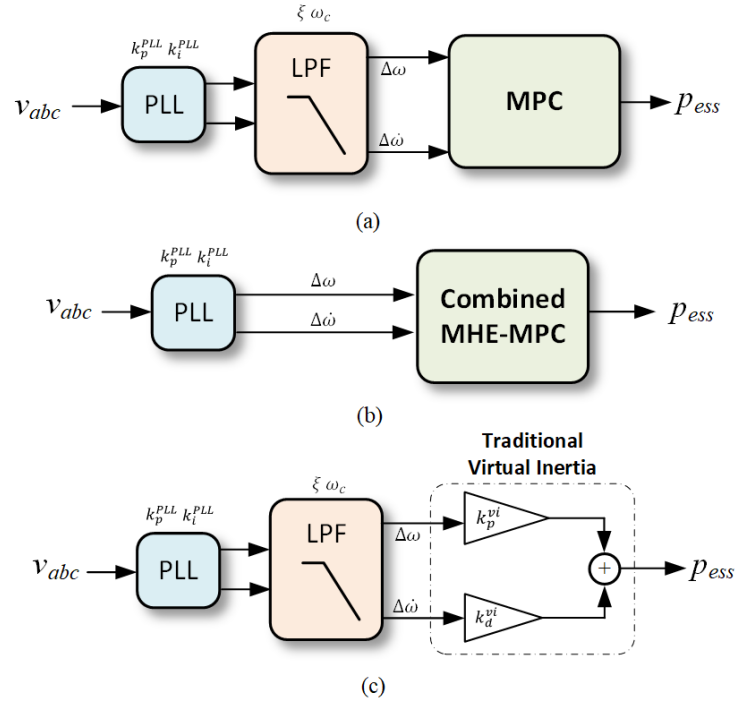


Figure 4.8. Simulation setups to analyze the advantage of the MHE module. (a) MPC with measurements from PLL with LPF. (b) Proposed combined MHE-MPC. (c) Traditional virtual-inertia controller with measurements from PLL with LPF.

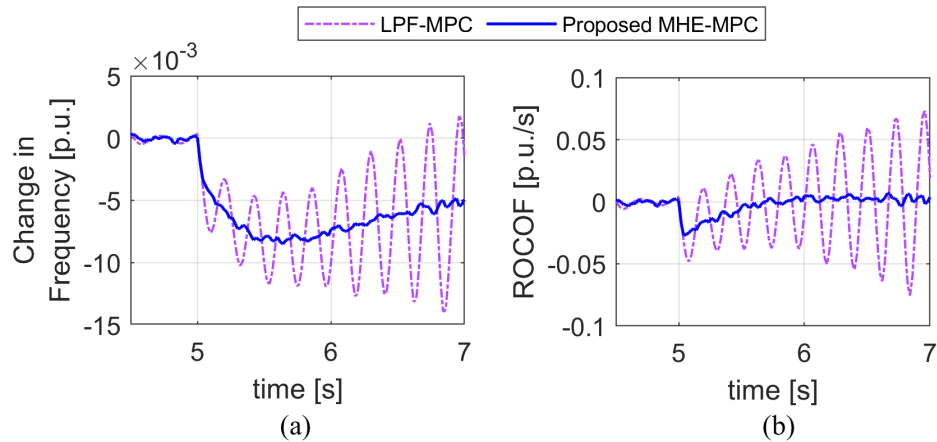


Figure 4.9. Frequency, ROCOF and peak power output of ESS with and without the MHE module for the same weighting parameters.

Next, the performance of the proposed framework is compared against a traditional VI controller with simulation setup shown in Figure 4.8(c). The same LPF with cut-off

frequency f_c of 5 Hz is employed to filter noisy measurements. As an example, the proportional gain of the controller k_i^{VI} is set to 15 while the derivative gain k_d^{VI} is set to 25. These gains are tuned such that the VI controller has a similar response as the proposed MHE-MPC framework with the weighting parameters sets to $Q = \text{diag}(0.1, 0.9)$ and $R = 0.0001$. Using the PLL with LPF under these high gains leads to oscillatory behavior in the frequency and ROCOF as shown in Figure 4.10. To further illustrate the fact that the oscillatory behavior is in fact due to the delay from LPF, the same simulation was performed without a LPF (under the assumption that there was no measurement noise). Without the LPF, the system does not show oscillatory behavior under the same gains and shows similar performance as the proposed MHE-MPC framework. These simulations highlights that the LPF delay can lead to oscillatory response and the use of MHE can enhance the system dynamic performance.

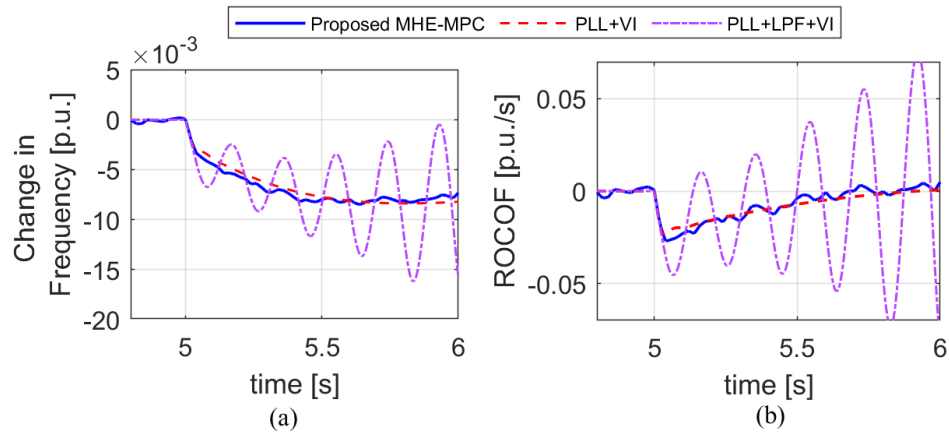


Figure 4.10. Frequency, ROCOF and peak power output of ESS when using a traditional virtual inertia controller versus the proposed MHE-MPC framework.

4.6 Computational Tractability

Although approaches such as MPC and MHE had seen limited practical applications in the past, advancements in computational capabilities of low-cost embedded controllers and significant research in development fast real-time solvers pave the path to utilize these approaches for fast-frequency support mechanisms which require fast execution times in the range of milliseconds. One of the main advancement has been the development of what is known as *real-time iteration* approach in literature to efficiently solve MHE and MPC in dynamic systems [137], [138]. This approach reduces the computational burden by limiting the sequential programming method used to solve the optimization problem to one iteration per sample [118]. Furthermore, several code-generation tools to implement these predictive control and estimation approaches on embedded hardware through efficient code-generation have received significant attention allowing milliseconds or even microseconds level implementation [139]. By optimizing aspects of memory access, cache usage and exploiting the problem's specific structure, efficient codes can be generated for embedded application. The ACADO code-generation tools, for instance, can generate highly efficient C code for embedded applications by implementing a custom real-time iteration scheme. ACADO code-generation tool has been already demonstrated in a number of real-world experiments that require execution times in the range of milliseconds or microseconds [140]–[142]. Future work should incorporate testing these in low-cost hardware.

4.7 Chapter Conclusions

A control framework for fast-frequency support in low-inertia microgrids was developed. The framework combined a MHE with MPC to achieve a flexible framework. Through simulations performed in a low-inertia test system, it was illustrated that the MHE can estimate the change in frequency and ROCOF of the system from noisy PLL measurements. This allowed the fast-frequency support to be provided in conjunction with the MPC to achieve significant reductions in frequency deviation and ROCOF without any oscillatory phenomenon as with the traditional virtual inertia controllers. The flexibility of the proposed MHE-MPC fast-frequency support framework through tuning the weighting matrices allows the ESS or microgrid operator to tune the QoS provided, allowing the trade-off between performance and battery degradation. It was also shown that the proposed framework can incorporate physical operating constraints of an ESS, such as peak-power limits. As an added benefit, properly setting this constraint, allows the ESS owner to provide stacked services to the microgrid, and maximize revenue over the battery lifetime.

CHAPTER 5 CONCLUSIONS AND FUTURE WORK

5.1 Conclusions

The rapid development of renewable energy sources (RESs) is causing the modern power grid to gravitate towards an inverter-dominated system from a rotational generator-dominated system. The inverter-based generation does not provide any mechanical inertial response, and hence compromises the frequency stability of the system. This leads to increased rate-of-change-of-frequency (ROCOF), and high-frequency nadirs in the power system. Such situations can lead to tripping of frequency relays causing under-frequency load shedding (UFLS) and, in the worst case, may lead to cascaded outages. Fast-frequency support provided by emulating virtual inertia through energy storage systems (ESSs) can limit the ROCOF and keep the frequency within safe limits.

Fast-frequency support is a power-intensive service and can result in large power demands and ramp-rates from the energy medium, which can have a substantial negative impact on the ESS lifetime. The ESS operator needs to provide fast-frequency support to minimize ROCOF and frequency deviation while minimizing the impact on the ESS. Furthermore, there are physical constraints to be considered, such as limits on peak power and/or ramp-rates. It is thus favorable for the ESS operator to be able to dispatch the ESS unit based on the desired frequency quality-of-service (QoS) required in the microgrid (limiting the ROCOF and frequency) and the incentives required to provide the QoS for such a frequency-as-a-service in the market. In this dissertation, an optimization-based fast-frequency support mechanism is developed for low inertia power systems. The

developed framework has the flexibility to change dynamic performance based on resource availability and the desired level of QoS. Furthermore, the framework can incorporate the physical constraints of the ESS such as peak-power limits and ramp-rate limits. To ensure the framework can adapt to changing system parameters (inertia and damping constant) an online estimator is also developed.

Proper assessment of the system inertia is of critical importance for system operators to deploy effective strategies to supplement the lost inertia. With non-synchronous, inverter-based generation sources as photovoltaics (PVs) and wind continuously displacing the traditional generators, it is challenging to estimate the inertia of a power system at any given time. Recently RESs have been deployed with characteristics that can emulate inertia as well. So, the inertial response from RESs also needs to be accounted for when estimating the inertia. All the aforementioned factors indicates a need for real-time inertia estimation technique. Estimating the inertia and damping constant will aid a system operator to deploy adaptive fast-frequency support strategies. Such situational awareness is imperative for the system operator to have enough reserves in place for any plausible contingency in the system.

In Chapter 2, a literature review of the current state-of-the-art of virtual inertia and fast-frequency support implementation techniques is presented. The major topologies are compared and classified. Through literature review and simulations of some selected topologies, it is shown that similar inertial response can be achieved by relating the parameters of these topologies through time constants and inertia constants, although the exact frequency dynamics may vary slightly. The suitability of a topology depends on control system architecture and the desired level of detail in the replication of the

dynamics of synchronous generators. The techniques are classified into three distinct generations which highlight the evolution and trends in the literature related to fast-frequency support mechanisms in the literature.

Next, in Chapter 3, for online estimation of inertia and damping constant of a system, an approach using moving horizon estimation (MHE) is developed. Based on the frequency measurements obtained in response to a non-intrusive excitation signal from an ESS, the two system constants are estimated using local measurements from the ESS phase-locked loop. The proposed MHE formulation is tested in a simulation model, and the technique estimated the unknown inertia and damping constant of the system within 10% of the true value under moderate measurement noise. Estimates provided by the proposed method can be utilized for applications such as fast-frequency control, adaptive protection schemes, and planning and procurement of spinning reserves.

Finally, in Chapter 4, a framework that allows the ESS operator to provide fast-frequency support as a service is proposed. The framework maintains the desired QoS while considering the ESS lifetime and physical limits. The framework utilizes MHE to estimate the frequency deviation and ROCOF from noisy PLL measurements. These estimates are employed by a model predictive control (MPC) algorithm that computes control actions by solving a finite-horizon, online optimization problem. Additionally, this approach avoids oscillatory behavior and instability induced by delays that are common when using low pass filters and traditional derivative-based (virtual inertia) controllers with high gains. MATLAB/Simulink simulations on a modified benchmark from Cordova, Alaska, shows the effectiveness of the MHE-MPC approach to reduce frequency deviations and ROCOF of a low inertia microgrid.

This dissertation was limited to developing the foundations to deploy fast-frequency support mechanisms using the concept of the QoS framework. Concepts from cloud computing can be borrowed to further expand on this framework. A possible implementation scenario can be where service level agreements specifying QoS targets (such as maximum ROCOF and minimum frequency nadir) can be developed between the service provider (the ESS) and the microgrid system operator for a given microgrid power imbalance. The ESS operator can then utilize estimates of inertia constant of the microgrid to find the right trade-off between the agreed QoS and its operational cost. The service level agreements might also include economic penalties in case the agreed QoS is violated. Further research would be required to develop appropriate mechanisms to deploy market mechanisms that will support this proposed framework.

5.2 Future Work

Future work should include testing the developed inertia and damping constant estimator in a real power system benchmark. The framework can be extended to estimate inertia and damping constant of multi-area power systems. This may require updating the underlying frequency dynamics model used. The assumption in implementing the MHE framework has been that the inertia constant and the damping constant remains constant during the MPC's control horizon. With multiple distributed units in multi-area power systems participating in fast-frequency support this assumption may not hold true and is worth investigating in future research.

The proposed optimization-based MHE-MPC framework can be validated in a realistic scenario through power-hardware-in-the-loop simulations. Currently, the

formulation does not incorporate a detailed model of an ESS. Incorporating a real model of ESS through power-hardware-in-the-loop testing while including limits of state-of-charge, peak-power limits and/or limits can further help to validate the proposed framework. Finally, long-term simulations that can highlight how the proposed framework can help in limit battery degradation will further emphasize the advantages of this proposed framework.

REFERENCES

- [1] EIA, “Annual Energy Outlook 2017 Renewable Energy Assumptions,” U.S. Department of Energy, Washington DC, USA, Tech. Rep. July, 2017, pp. 188–201. (visited on 06/21/2017).
- [2] IEA PVPS, “Trends in photovoltaic applications, Report T1-14:2005,” Tech. Rep., 2005. (visited on 06/21/2017).
- [3] B. Kroposki, B. Johnson, Y. Zhang, V. Gevorgian, P. Denholm, B. M. Hodge, and B. Hannegan, “Achieving a 100% Renewable Grid: Operating Electric Power Systems with Extremely High Levels of Variable Renewable Energy,” *IEEE Power and Energy Magazine*, vol. 15, no. 2, pp. 61–73, 2017. DOI: 10.1109/MPE.2016.2637122.
- [4] M. Hussein, T. Senjyu, M. Orabi, M. Wahab, and M. Hamada, “Control of a Stand-Alone Variable Speed Wind Energy Supply System,” *Applied Sciences*, vol. 3, no. 2, pp. 437–456, 2013. DOI: 10.3390/app3020437.
- [5] R. Yan, T. K. Saha, N. Modi, N. A. Masood, and M. Mosadeghy, “The combined effects of high penetration of wind and PV on power system frequency response,” *Applied Energy*, vol. 145, pp. 320–330, 2015. DOI: 10.1016/j.apenergy.2015.02.044.
- [6] A. Gurung, D. Galipeau, R. Tonkoski, and I. Tamrakar, “Feasibility study of Photovoltaic-hydropower microgrids,” in *Proceedings of the 5th International Conference on Power and Energy Systems (ICPS)*, Kathmandu, Nepal, 2014, 6 pp.
- [7] U. Tamrakar, D. Galipeau, R. Tonkoski, and I. Tamrakar, “Improving transient stability of photovoltaic-hydro microgrids using virtual synchronous machines,” in *IEEE Eindhoven PowerTech*, Institute of Electrical and Electronics Engineers Inc., 2015. DOI: 10.1109/PTC.2015.7232663.
- [8] “Future Ancillary Services in ERCOT,” ERCOT, Tech. Rep.
- [9] J. Matevosyan, S. Sharma, S. H. Huang, D. Woodfin, K. Ragsdale, S. Moorthy, P. Wattles, and W. Li, “Proposed future Ancillary Services in Electric Reliability Council of Texas,” in *IEEE Eindhoven PowerTech*, 2015. DOI: 10.1109/PTC.2015.7232743.
- [10] J. Matevosyan, *Implementation of Inertia Monitoring in ERCOT – What’s It All About?* 2018. [Online]. Available: <https://www.esig.energy/implementation-of-inertia-monitoring-in-ercot-whats-it-all-about/> (visited on 03/01/2020).
- [11] B. K. Poolla, S. Bolognani, and F. Dorfler, “Optimal Placement of Virtual Inertia in Power Grids,” *IEEE Transactions on Automatic Control*, vol. 62, no. 12, pp. 6209–6220, 2017. DOI: 10.1109/tac.2017.2703302.

- [12] J. Van De Vyver, J. D. De Kooning, B. Meersman, L. Vandeveldel, and T. L. Vandoorn, "Droop Control as an Alternative Inertial Response Strategy for the Synthetic Inertia on Wind Turbines," *IEEE Transactions on Power Systems*, vol. 31, no. 2, pp. 1129–1138, 2016. DOI: 10.1109/TPWRS.2015.2417758.
- [13] H. Thiesen, C. Jauch, and A. Gloe, "Design of a system substituting today's inherent inertia in the European continental synchronous area," *Energies*, vol. 9, no. 8, 2016. DOI: 10.3390/en9080582.
- [14] H. Sturgess, W. Mak, and A. Bourn, "Initial analysis and thoughts on the power outages on 9th August," Aurora Energy Research, Tech. Rep., 2019. [Online]. Available: <https://www.auroraer.com/wp-content/uploads/2019/08/Initial-Thoughts-and-Analysis-on-the-Power-Outages-on-9th-August.pdf>.
- [15] *Smart Power Electronic Converters May Help Stabilize the Grid - IEEE Spectrum*. [Online]. Available: <https://spectrum.ieee.org/energywise/energy/the-smarter-grid/can-power-electronic-converters-lead-to-grid-stability> (visited on 03/01/2020).
- [16] J. M. Guerrero, L. G. de Vicuna, J. Matas, M. Castilla, and J. Miret, "A wireless controller to enhance dynamic performance of parallel inverters in distributed generation systems," *IEEE Transactions on Power Electronics*, vol. 19, no. 5, pp. 1205–1213, 2004. DOI: 10.1109/TPEL.2004.833451.
- [17] N. Hatziargyriou, H. Asano, R. Iravani, and C. Marnay, "Microgrids," *IEEE power and energy magazine*, vol. 5, no. 4, pp. 78–94, 2007. DOI: 10.1109/MPAE.2007.376583.
- [18] J. Kim, J. M. Guerrero, P. Rodriguez, R. Teodorescu, and K. Nam, "Mode adaptive droop control with virtual output impedances for an inverter-based flexible AC microgrid," *IEEE Transactions on Power Electronics*, vol. 26, no. 3, pp. 689–701, 2011. DOI: 10.1109/TPEL.2010.2091685.
- [19] M. Farrokhhabadi, D. Lagos, R. W. Wies, M. Paolone, M. Liserre, L. Meegahapola, M. Kabalan, A. H. Hajimiragha, D. Peralta, M. A. Elizondo, K. P. Schneider, C. A. Canizares, F. K. Tuffner, J. Reilly, J. W. Simpson-Porco, E. Nasr, L. Fan, P. A. Mendoza-Araya, R. Tonkoski, U. Tamrakar, and N. Hatziargyriou, "Microgrid Stability Definitions, Analysis, and Examples," *IEEE Transactions on Power Systems*, vol. 35, no. 1, pp. 13–29, 2020. DOI: 10.1109/TPWRS.2019.2925703.
- [20] H. Bevrani, *Robust Power System Frequency Control*, ser. Power Electronics and Power Systems. Cham: Springer International Publishing, 2014. DOI: 10.1007/978-3-319-07278-4. [Online]. Available: <http://link.springer.com/10.1007/978-3-319-07278-4>.

- [21] “Frequency Response Initiative Report The Reliability Role of Frequency Response,” Tech. Rep., 2012. [Online]. Available: https://www.nerc.com/docs/pc/FRI_Report_10-30-12_Master_w-appendices.pdf.
- [22] British Standards Institute, “Reciprocating internal combustion engine driven alternating current generating sets,” Tech. Rep., 2005. [Online]. Available: <https://www.iso.org/standard/39047.html>.
- [23] M. Torres and L. A. C. Lopes, “Virtual Synchronous Generator: A Control Strategy to Improve Dynamic Frequency Control in Autonomous Power Systems,” *Energy and Power Engineering*, vol. 05, no. 02, pp. 32–38, 2013. DOI: 10.4236/epe.2013.52a005.
- [24] D. Shrestha, U. Tamrakar, N. Malla, N. Zhen, and R. Tonkoski, “Reduction of energy consumption of virtual synchronous machine using supplementary adaptive dynamic programming,” in *IEEE International Conference on Electro Information Technology*, 2016, pp. 690–694. DOI: 10.1109/EIT.2016.7535323.
- [25] C. Rahmann and A. Castillo, “Fast frequency response capability of photovoltaic power plants: The necessity of new grid requirements and definitions,” *Energies*, vol. 7, no. 10, pp. 6306–6322, 2014. DOI: 10.3390/en7106306.
- [26] L. R. Chang-Chien, W. T. Lin, and Y. C. Yin, “Enhancing frequency response control by DFIGs in the high wind penetrated power systems,” *IEEE Transactions on Power Systems*, vol. 26, no. 2, pp. 710–718, 2011. DOI: 10.1109/TPWRS.2010.2052402.
- [27] “Voltage characteristics of electricity supplied by public distribution systems,” European Standard EN50160, Tech. Rep., 1999.
- [28] D. R. Conover, S. R. Ferreira, A. J. Crawford, D. A. Schoenwald, J Fuller, D. M. Rosewater, S. N. Gourisetti, and V Viswanathan, “Protocol for Uniformly Measuring and Expressing the Performance of Energy Storage Systems,” Tech. Rep., 2016.
- [29] M. Bahloul and S. K. Khadem, “Impact of power sharing method on battery life extension in HESS for grid ancillary services,” *IEEE Transactions on Energy Conversion*, vol. 34, no. 3, pp. 1317–1327, 2018. DOI: 10.1109/TEC.2018.2886609.
- [30] S. Vazquez, S. M. Lukic, E. Galvan, L. G. Franquelo, and J. M. Carrasco, “Energy storage systems for transport and grid applications,” *IEEE Transactions on Industrial Electronics*, vol. 57, no. 12, pp. 3881–3895, 2010. DOI: 10.1109/TIE.2010.2076414.

- [31] F. Gonzalez-Longatt, "Impact of synthetic inertia from wind power on the protection/control schemes of future power systems: Simulation study," *IET Conference Publications*, vol. 2012, no. 593 CP, pp. 74–80, 2012. DOI: 10.1049/cp.2012.0030. [Online]. Available: <http://digital-library.theiet.org/content/conferences/10.1049/cp.2012.0030>.
- [32] H. Bevrani, T. Ise, and Y. Miura, "Virtual synchronous generators: A survey and new perspectives," *International Journal of Electrical Power and Energy Systems*, vol. 54, pp. 244–254, 2014. DOI: 10.1016/j.ijepes.2013.07.009.
- [33] Q. C. Zhong and G. Weiss, "Synchronverters: Inverters that mimic synchronous generators," *IEEE Transactions on Industrial Electronics*, vol. 58, no. 4, pp. 1259–1267, 2011. DOI: 10.1109/TIE.2010.2048839.
- [34] Q. C. Zhong, P. L. Nguyen, Z. Ma, and W. Sheng, "Self-synchronized synchronverters: Inverters without a dedicated synchronization unit," *IEEE Transactions on Power Electronics*, vol. 29, no. 2, pp. 617–630, 2014. DOI: 10.1109/TPEL.2013.2258684.
- [35] R. Hesse, D. Turschner, and H. P. Beck, "Micro grid stabilization using the virtual synchronous machine (VISMA)," *Renewable Energy and Power Quality Journal*, vol. 1, no. 7, pp. 676–681, 2009. DOI: 10.24084/repqj07.472.
- [36] Y. Chen, R. Hesse, D. Turschner, and H. P. Beck, "Dynamic properties of the virtual synchronous machine (VISMA)," *Renewable Energy and Power Quality Journal*, vol. 1, no. 9, pp. 755–759, 2011. DOI: 10.24084/repqj09.444.
- [37] Y. Chen, R. Hesse, D. Turschner, and H. P. Beck, "Comparison of methods for implementing virtual synchronous machine on inverters," *Renewable Energy and Power Quality Journal*, vol. 1, no. 10, pp. 734–739, 2012. DOI: 10.24084/repqj10.453.
- [38] Y. Hirase, K. Abe, K. Sugimoto, and Y. Shindo, "A grid-connected inverter with virtual synchronous generator model of algebraic type," *Electrical Engineering in Japan (English translation of Denki Gakkai Ronbunshi)*, vol. 184, no. 4, pp. 10–21, 2013. DOI: 10.1002/eej.22428.
- [39] K. Sakimoto, Y. Miura, and T. Ise, "Stabilization of a power system with a distributed generator by a Virtual Synchronous Generator function," in *8th International Conference on Power Electronics*, 2011, pp. 1498–1505. DOI: 10.1109/ICPE.2011.5944492.
- [40] J. Alipoor, Y. Miura, and T. Ise, "Power system stabilization using virtual synchronous generator with alternating moment of inertia," *IEEE Journal of Emerging and Selected Topics in Power Electronics*, vol. 3, no. 2, pp. 451–458, 2015.

- [41] K. Sakimoto, Y. Miura, and T. Ise, “Characteristics of parallel operation of inverter-type distributed generators operated by a virtual synchronous generator,” *Electrical Engineering in Japan (English translation of Denki Gakkai Ronbunshi)*, vol. 192, no. 4, pp. 9–19, 2015. DOI: 10.1002/eej.22561.
- [42] T. Shintai, Y. Miura, and T. Ise, “Reactive power control for load sharing with virtual synchronous generator control,” in *IEEE 7th International Power Electronics and Motion Control Conference*, 2012, pp. 846–853. DOI: 10.1109/IPEMC.2012.6258956.
- [43] P. Rodriguez, I. Candela, and A. Luna, “Control of PV generation systems using the synchronous power controller,” in *IEEE Energy Conversion Congress and Exposition*, 2013, pp. 993–998. DOI: 10.1109/ECCE.2013.6646811.
- [44] W. Zhang, D. Remon, A. Mir, A. Luna, J. Rocabert, I. Candela, and P. Rodriguez, “Comparison of different power loop controllers for synchronous power controlled grid-interactive converters,” in *IEEE Energy Conversion Congress and Exposition*, 2015, pp. 3780–3787. DOI: 10.1109/ECCE.2015.7310194.
- [45] W. Zhang, A. M. Cantarellas, J. Rocabert, A. Luna, and P. Rodriguez, “Synchronous Power Controller with Flexible Droop Characteristics for Renewable Power Generation Systems,” *IEEE Transactions on Sustainable Energy*, vol. 7, no. 4, pp. 1572–1582, 2016. DOI: 10.1109/TSTE.2016.2565059.
- [46] V. Karapanos, S. De Haan, and K. Zwetsloot, “Real time simulation of a power system with VSG hardware in the loop,” in *IECON Proceedings (Industrial Electronics Conference)*, 2011, pp. 3748–3754. DOI: 10.1109/IECON.2011.6119919.
- [47] J. Morren, J. Pierik, and S. W. de Haan, “Inertial response of variable speed wind turbines,” *Electric Power Systems Research*, vol. 76, no. 11, pp. 980–987, 2006. DOI: 10.1016/j.epsr.2005.12.002.
- [48] J. Driesen and K. Visscher, “Virtual synchronous generators,” in *IEEE Power and Energy Society General Meeting*, 2008. DOI: 10.1109/PES.2008.4596800.
- [49] M. Torres, L. A. Lopes, L. A. Morán T., and J. R. Espinoza C., “Self-tuning virtual synchronous machine: A control strategy for energy storage systems to support dynamic frequency control,” *IEEE Transactions on Energy Conversion*, vol. 29, no. 4, pp. 833–840, 2014. DOI: 10.1109/TEC.2014.2362577.
- [50] H. P. Beck and R. Hesse, “Virtual synchronous machine,” *2007 9th International Conference on Electrical Power Quality and Utilisation, EPQU*, 2007. DOI: 10.1109/EPQU.2007.4424220.
- [51] M. Torres and L. A. Lopes, “Virtual synchronous generator control in autonomous wind-diesel power systems,” in *IEEE Electrical Power and Energy Conference*, 2009. DOI: 10.1109/EPEC.2009.5420953.

- [52] S. D'Arco and J. A. Suul, "Equivalence of virtual synchronous machines and frequency-droops for converter-based Microgrids," *IEEE Transactions on Smart Grid*, vol. 5, no. 1, pp. 394–395, 2014. DOI: 10.1109/TSG.2013.2288000.
- [53] B. B. Johnson, S. V. Dhople, A. O. Hamadeh, and P. T. Krein, "Synchronization of parallel single-phase inverters with virtual oscillator control," *IEEE Transactions on Power Electronics*, vol. 29, no. 11, pp. 6124–6138, 2014. DOI: 10.1109/TPEL.2013.2296292.
- [54] B. B. Johnson, S. V. Dhople, J. L. Cale, A. O. Hamadeh, and P. T. Krein, "Oscillator-based inverter control for islanded three-phase microgrids," *IEEE Journal of Photovoltaics*, vol. 4, no. 1, pp. 387–395, 2014. DOI: 10.1109/JPHOTOV.2013.2280953.
- [55] S. V. Dhople, B. B. Johnson, and A. O. Hamadeh, "Virtual Oscillator Control for voltage source inverters," in *51st Annual Allerton Conference on Communication, Control, and Computing*, 2013, pp. 1359–1363. DOI: 10.1109/Allerton.2013.6736685.
- [56] M. Ashabani, F. D. Freijedo, S. Golestan, and J. M. Guerrero, "Inducverters: PLL-Less Converters With Auto-Synchronization and Emulated Inertia Capability," *IEEE Transactions on Smart Grid*, vol. 7, no. 3, pp. 1660–1674, 2016. DOI: 10.1109/TSG.2015.2468600.
- [57] Q. C. Zhong, "Virtual Synchronous Machines: A unified interface for grid integration," *IEEE Power Electronics Magazine*, vol. 3, no. 4, pp. 18–27, 2016. DOI: 10.1109/MPEL.2016.2614906.
- [58] P. Kundur, *Power System Stability and Control*. McGraw-hill New York, 1994.
- [59] P. Piya and M. Karimi-Ghartemani, "A stability analysis and efficiency improvement of synchronverter," in *Conference Proceedings - IEEE Applied Power Electronics Conference and Exposition*, 2016, pp. 3165–3171. DOI: 10.1109/APEC.2016.7468317.
- [60] Q. C. Zhong and T. Hornik, *Control of Power Inverters in Renewable Energy and Smart Grid Integration*. John Wiley & Sons, 2012. DOI: 10.1002/9781118481806.
- [61] R. V. Ferreira, S. M. Silva, D. I. Brandao, and H. M. Antunes, "Single-phase synchronverter for residential PV power systems," in *Proceedings of International Conference on Harmonics and Quality of Power*, 2016, pp. 861–866. DOI: 10.1109/ICHQP.2016.7783378.
- [62] S. Shinnaka, "A robust single-phase PLL system with stable and fast tracking," *IEEE Transactions on Industry Applications*, vol. 44, no. 2, pp. 624–633, 2008. DOI: 10.1109/TIA.2008.916750.

- [63] L. Zhang, L. Harnefors, and H. P. Nee, "Power-synchronization control of grid-connected voltage-source converters," *IEEE Transactions on Power Systems*, vol. 25, no. 2, pp. 809–820, 2010. DOI: 10.1109/TPWRS.2009.2032231.
- [64] S. Wang, J. Hu, and X. Yuan, "Virtual Synchronous Control for Grid-Connected DFIG-Based Wind Turbines," *IEEE Journal of Emerging and Selected Topics in Power Electronics*, vol. 3, no. 4, pp. 932–944, 2015. DOI: 10.1109/JESTPE.2015.2418200.
- [65] Z. Ma, Q. C. Zhong, and J. D. Yan, "Synchronverter-based control strategies for three-phase PWM rectifiers," in *7th IEEE Conference on Industrial Electronics and Applications*, 2012, pp. 225–230. DOI: 10.1109/ICIEA.2012.6360727.
- [66] P. Tielens and D. V. Hertem, "The relevance of inertia in power systems," *Renewable and Sustainable Energy Reviews*, vol. 55, pp. 999–1009, 2016. DOI: <https://doi.org/10.1016/j.rser.2015.11.016>.
- [67] M. P. Van Wesenbeeck, S. W. De Haan, P. Varela, and K. Visscher, "Grid tied converter with virtual kinetic storage," in *IEEE Bucharest PowerTech*, 2009. DOI: 10.1109/PTC.2009.5282048.
- [68] T. Vu Van, K. Visscher, J. Diaz, V. Karapanos, A. Woyte, M. Albu, J. Bozelie, T. Loix, and D. Federenciuc, "Virtual synchronous generator: An element of future grids," in *IEEE PES Innovative Smart Grid Technologies Conference Europe*, 2010. DOI: 10.1109/ISGTEUROPE.2010.5638946.
- [69] B. Wen, D. Boroyevich, R. Burgos, P. Mattavelli, and Z. Shen, "Small-Signal Stability Analysis of Three-Phase AC Systems in the Presence of Constant Power Loads Based on Measured d-q Frame Impedances," *IEEE Transactions on Power Electronics*, vol. 30, no. 10, pp. 5952–5963, 2015. DOI: 10.1109/TPEL.2014.2378731.
- [70] U. Tamrakar, R. Tonkoski, N. Zhen, T. M. Hansen, and I. Tamrakar, "Current control techniques for applications in virtual synchronous machines," in *IEEE 6th International Conference on Power Systems*, 2016, 6 pp. DOI: 10.1109/ICPES.2016.7584166.
- [71] D. Shrestha, U. Tamrakar, Z. Ni, and R. Tonkoski, "Experimental verification of virtual inertia in diesel generator based microgrids," in *Proceedings of the IEEE International Conference on Industrial Technology*, 2017, pp. 95–100. DOI: 10.1109/ICIT.2017.7913065.
- [72] V. Van Thong, A. Woyte, M. Albu, M. Van Hest, J. Bozelie, J. Diaz, T. Loix, D. Stanculescu, and K. Visscher, "Virtual synchronous generator: Laboratory scale results and field demonstration," in *IEEE Bucharest PowerTech*, 2009. DOI: 10.1109/PTC.2009.5281790.

- [73] M. F. M. Arani and E. F. El-Saadany, "Implementing virtual inertia in DFIG-based wind power generation," *IEEE Transactions on Power Systems*, vol. 28, no. 2, pp. 1373–1384, 2013. DOI: 10.1109/TPWRS.2012.2207972.
- [74] F. Blaabjerg, R. Teodorescu, M. Liserre, and A. V. Timbus, *Overview of control and grid synchronization for distributed power generation systems*, 2006. DOI: 10.1109/TIE.2006.881997.
- [75] S. D'Arco and J. A. Suul, "Virtual synchronous machines - Classification of implementations and analysis of equivalence to droop controllers for microgrids," in *IEEE Grenoble Conference PowerTech*, 2013. DOI: 10.1109/PTC.2013.6652456.
- [76] S. Khan, B. Bletterie, A. Anta, and W. Gawlik, "On Small Signal Frequency Stability under Virtual Inertia and the Role of PLLs," *Energies*, vol. 11, no. 9, p. 2372, 2018. DOI: 10.3390/en11092372. [Online]. Available: <http://www.mdpi.com/1996-1073/11/9/2372>.
- [77] T. Midtsund, J. A. Suul, and T. Undeland, "Evaluation of current controller performance and stability for voltage source converters connected to a weak grid," in *2nd International Symposium on Power Electronics for Distributed Generation Systems*, 2010, pp. 382–388. DOI: 10.1109/PEDG.2010.5545794.
- [78] J. Svensson, "Synchronisation methods for grid-connected voltage source converters," *IEE Proceedings: Generation, Transmission and Distribution*, vol. 148, no. 3, pp. 229–235, 2001. DOI: 10.1049/ip-gtd:20010101.
- [79] F. Katiraei and M. R. Iravani, "Power management strategies for a microgrid with multiple distributed generation units," *IEEE Transactions on Power Systems*, vol. 21, no. 4, pp. 1821–1831, 2006. DOI: 10.1109/TPWRS.2006.879260.
- [80] N. Pogaku, M. Prodanović, and T. C. Green, "Modeling, analysis and testing of autonomous operation of an inverter-based microgrid," *IEEE Transactions on Power Electronics*, vol. 22, no. 2, pp. 613–625, 2007. DOI: 10.1109/TPEL.2006.890003.
- [81] C. Li, R. Burgos, I. Cvetkovic, D. Boroyevich, L. Mili, and P. Rodriguez, "Analysis and design of virtual synchronous machine based STATCOM controller," in *IEEE 15th Workshop on Control and Modeling for Power Electronics*, 2014. DOI: 10.1109/COMPEL.2014.6877134.
- [82] N. Soni, S. Doolla, and M. C. Chandorkar, "Improvement of transient response in microgrids using virtual inertia," *IEEE Transactions on Power Delivery*, vol. 28, no. 3, pp. 1830–1838, 2013. DOI: 10.1109/TPWRD.2013.2264738.
- [83] ABENGOA Solar NewTechnologies, "Virtual admittance controller based on static power converters," *International patent application WO 2012/117133*, no. U.S. Patent US20140049233, 2012.

- [84] R. R. Behera and A. N. Thakur, "An overview of various grid synchronization techniques for single-phase grid integration of renewable distributed power generation systems," in *International Conference on Electrical, Electronics, and Optimization Techniques*, 2016, pp. 2876–2880. DOI: 10.1109/ICEEOT.2016.7755223.
- [85] V. Natarajan and G. Weiss, "Synchronverters with Better Stability Due to Virtual Inductors, Virtual Capacitors, and Anti-Windup," *IEEE Transactions on Industrial Electronics*, vol. 64, no. 7, pp. 5994–6004, 2017. DOI: 10.1109/TIE.2017.2674611.
- [86] S. Dong and Y. C. Chen, "Adjusting Synchronverter Dynamic Response Speed via Damping Correction Loop," *IEEE Transactions on Energy Conversion*, vol. 32, no. 2, pp. 608–619, 2017. DOI: 10.1109/TEC.2016.2645450.
- [87] Q. C. Zhong, G. C. Konstantopoulos, B. Ren, and M. Krstic, "Improved synchronverters with bounded frequency and voltage for smart grid integration," *IEEE Transactions on Smart Grid*, vol. 9, no. 2, pp. 786–796, 2018. DOI: 10.1109/TSG.2016.2565663.
- [88] J. Alipoor, Y. Miura, and T. Ise, "Stability assessment and optimization methods for microgrid with multiple VSG units," *IEEE Transactions on Smart Grid*, vol. 9, no. 2, pp. 1462–1471, 2018. DOI: 10.1109/TSG.2016.2592508.
- [89] W. Guo, F. Liu, J. Si, and S. Mei, "Incorporating approximate dynamic programming-based parameter tuning into PD-type virtual inertia control of DFIGs," in *Proceedings of the International Joint Conference on Neural Networks*, 2013. DOI: 10.1109/IJCNN.2013.6707069.
- [90] M. Torres, L. A. Lopes, and A. Load, "An optimal virtual inertia controller to support frequency regulation in autonomous diesel power systems with high penetration of renewables," *Renewable Energy and Power Quality Journal*, vol. 1, no. 9, pp. 959–964, 2011. DOI: 10.24084/repqj09.510.
- [91] M. Datta, H. Ishikawa, H. Naitoh, and T. Senjyu, "Frequency control improvement in a PV-diesel hybrid power system with a virtual inertia controller," in *7th IEEE Conference on Industrial Electronics and Applications*, 2012, pp. 1167–1172. DOI: 10.1109/ICIEA.2012.6360900.
- [92] B. K. Poolla, S. Bolognani, L. Na, and F. Dorfler, "A Market Mechanism for Virtual Inertia," *IEEE Transactions on Smart Grid*, pp. 1–1, 2020. arXiv: 1711.04874.
- [93] K. Tuttelberg, J. Kilter, D. Wilson, and K. Uhlen, "Estimation of power system inertia from ambient wide area measurements," *IEEE Transactions on Power Systems*, vol. 33, no. 6, pp. 7249–7257, 2018. DOI: 10.1109/TPWRS.2018.2843381.

- [94] X. Cao, B. Stephen, I. F. Abdulhadi, C. D. Booth, and G. M. Burt, "Switching Markov Gaussian Models for Dynamic Power System Inertia Estimation," *IEEE Transactions on Power Systems*, vol. 31, no. 5, pp. 3394–3403, 2016. DOI: 10.1109/TPWRS.2015.2501458.
- [95] D. Groß, S. Bolognani, B. K. Poolla, and F. Dörfler, "Increasing the Resilience of Low-inertia Power Systems by Virtual Inertia and Damping," *IREP Bulk Power Systems Dynamics and Control Symposium*, 2017, 12 pp. DOI: 10.3929/ethz-b-000232185.
- [96] U. Tamrakar, T. M. Hansen, R. Tonkoski, and D. A. Copp, "Model Predictive Frequency Control of Low Inertia Microgrids," in *IEEE International Symposium on Industrial Electronics*, 2019, pp. 2111–2116. DOI: 10.1109/ISIE.2019.8781263.
- [97] D. Duckwitz and B. Fischer, "Modeling and Design of df/dt -Based Inertia Control for Power Converters," *IEEE Journal of Emerging and Selected Topics in Power Electronics*, vol. 5, no. 4, pp. 1553–1564, 2017. DOI: 10.1109/JESTPE.2017.2703814.
- [98] P. M. Ashton, G. A. Taylor, A. M. Carter, M. E. Bradley, and W. Hung, "Application of phasor measurement units to estimate power system inertial frequency response," in *IEEE Power and Energy Society General Meeting*, 2013. DOI: 10.1109/PESMG.2013.6672671.
- [99] T. Inoue, H. Taniguchi, Y. Ikeguchi, and K. Yoshida, "Estimation of power system inertia constant and capacity of spinning-reserve support generators using measured frequency transients," *IEEE Transactions on Power Systems*, vol. 12, no. 1, pp. 136–143, 1997. DOI: 10.1109/59.574933.
- [100] M. Shamirzaee, H. Ayoubzadeh, D. Farokhzad, F. Aminifar, and H. Haeri, "An improved method for estimation of inertia constant of power system based on polynomial approximation," in *IEEE Smart Grid Conference*, 2014. DOI: 10.1109/SGC.2014.7090867.
- [101] P. M. Ashton, C. S. Saunders, G. A. Taylor, A. M. Carter, and M. E. Bradley, "Inertia estimation of the GB power system using synchrophasor measurements," *IEEE Transactions on Power Systems*, vol. 30, no. 2, pp. 701–709, 2015. DOI: 10.1109/TPWRS.2014.2333776.
- [102] D. Zografos, M. Ghandhari, and K. Paridari, "Estimation of power system inertia using particle swarm optimization," in *19th IEEE International Conference on Intelligent System Application to Power Systems*, 2017. DOI: 10.1109/ISAP.2017.8071383.

- [103] P. M. Anderson and M. Mirheydar, “An adaptive method for setting underfrequency load shedding relays,” *IEEE Transactions on Power Systems*, vol. 7, no. 2, pp. 647–655, 1992. DOI: 10.1109/59.141770.
- [104] P. Wall and V. Terzija, “Simultaneous estimation of the time of disturbance and inertia in power systems,” *IEEE Transactions on Power Delivery*, vol. 29, no. 4, pp. 2018–2031, 2014. DOI: 10.1109/TPWRD.2014.2306062.
- [105] J. Zhang and H. Xu, “Online Identification of Power System Equivalent Inertia Constant,” *IEEE Transactions on Industrial Electronics*, vol. 64, no. 10, pp. 8098–8107, 2017. DOI: 10.1109/TIE.2017.2698414.
- [106] S. Boyd and L. Vandenberghe, *Convex Optimization*. Cambridge University Press, 2004. DOI: 10.1017/cbo9780511804441.
- [107] J. Schiffer, P. Aristidou, and R. Ortega, “Online Estimation of Power System Inertia Using Dynamic Regressor Extension and Mixing,” *IEEE Transactions on Power Systems*, vol. 34, no. 6, pp. 4993–5001, 2019. DOI: 10.1109/TPWRS.2019.2915249.
- [108] F. Milano, F. Dorfler, G. Hug, D. J. Hill, and G. Verbič, “Foundations and challenges of low-inertia systems (Invited Paper),” in *20th IEEE Power Systems Computation Conference*, 2018. DOI: 10.23919/PSCC.2018.8450880.
- [109] U. Markovic, Z. Chu, P. Aristidou, and G. Hug, “Fast Frequency Control Scheme through Adaptive Virtual Inertia Emulation,” in *International Conference on Innovative Smart Grid Technologies*, 2018, pp. 787–792. DOI: 10.1109/ISGT-Asia.2018.8467920.
- [110] F. Auger, M. Hilairet, J. M. Guerrero, E. Monmasson, T. Orłowska-Kowalska, and S. Katsura, “Industrial applications of the kalman filter: A review,” *IEEE Transactions on Industrial Electronics*, vol. 60, no. 12, pp. 5458–5471, 2013. DOI: 10.1109/TIE.2012.2236994.
- [111] S. Aksoy, A. Mühürçü, and H. Kizmaz, “State and parameter estimation in induction motor using the Extended Kalman Filtering algorithm,” in *Proceedings - International Symposium: Modern Electric Power Systems*, Wroclaw, 2010, 5 pp.
- [112] J. B. Rawlings and B. R. Bakshi, “Particle filtering and moving horizon estimation,” *Computers and Chemical Engineering*, vol. 30, no. 10-12, pp. 1529–1541, 2006. DOI: 10.1016/j.compchemeng.2006.05.031.
- [113] H. J. Ferreau, T. Kraus, M. Vukov, W. Saeys, and M. Diehl, “High-speed moving horizon estimation based on automatic code generation,” in *Proceedings of the IEEE Conference on Decision and Control*, 2012, pp. 687–692. DOI: 10.1109/CDC.2012.6426428.
- [114] C. V. Rao, J. B. Rawlings, and J. H. Lee, “Constrained linear state estimation—a moving horizon approach,” *Automatica*, vol. 37, no. 10, pp. 1619–1628, 2001.

- [115] C. V. Rao, J. B. Rawlings, and D. Q. Mayne, "Constrained state estimation for nonlinear discrete-time systems: Stability and moving horizon approximations," *IEEE Transactions on Automatic Control*, vol. 48, no. 2, pp. 246–258, 2003.
- [116] S. A. Quintero, D. A. Copp, and J. P. Hespanha, "Robust UAV coordination for target tracking using output-feedback model predictive control with moving horizon estimation," in *Proceedings of the American Control Conference*, 2015, pp. 3758–3764. DOI: 10.1109/ACC.2015.7171914.
- [117] D. A. Copp, T. A. Nguyen, and R. H. Byrne, "Adaptive model predictive control for real-time dispatch of energy storage systems," in *Proceedings of the American Control Conference*, vol. 2019-July, 2019, pp. 3611–3616. DOI: 10.23919/acc.2019.8814902.
- [118] P. Kühn, M. Diehl, T. Kraus, J. P. Schlöder, and H. G. Bock, "A real-time algorithm for moving horizon state and parameter estimation," *Computers & chemical engineering*, vol. 35, no. 1, pp. 71–83, 2011.
- [119] M. Zanon, J. V. Frasch, and M. Diehl, "Nonlinear Moving Horizon Estimation for combined state and friction coefficient estimation in autonomous driving," in *European Control Conference*, 2013, pp. 4130–4135. DOI: 10.23919/ecc.2013.6669832.
- [120] D. Ariens, B. Houska, and H. Ferreau, "ACADO for Matlab User's Manual," Tech. Rep., 2011. [Online]. Available: <http://www.acadotoolkit.org>.
- [121] M. Brown, M. Biswal, S. Brahma, S. J. Ranade, and H. Cao, "Characterizing and quantifying noise in PMU data," in *IEEE Power and Energy Society General Meeting*, 2016. DOI: 10.1109/PESGM.2016.7741972.
- [122] S. Wang, J. Zhao, Z. Huang, and R. Diao, "Assessing Gaussian Assumption of PMU Measurement Error Using Field Data," *IEEE Transactions on Power Delivery*, vol. 33, no. 6, pp. 3233–3236, 2017. DOI: 10.1109/tpwrd.2017.2762927.
- [123] H. Karimi, M. Karimi-Ghartemani, and M. R. Iravani, "Estimation of frequency and its rate of change for applications in power systems," *IEEE Transactions on Power Delivery*, vol. 19, no. 2, pp. 472–480, 2004. DOI: 10.1109/TPWRD.2003.822957.
- [124] E. Hossain, E. Kabalci, R. Bayindir, and R. Perez, "Microgrid testbeds around the world: State of art," *Energy Conversion and Management*, vol. 86, pp. 132–153, 2014. DOI: 10.1016/j.enconman.2014.05.012.
- [125] R. H. Byrne, T. A. Nguyen, D. A. Copp, B. R. Chalamala, and I. Gyuk, "Energy Management and Optimization Methods for Grid Energy Storage Systems," *IEEE Access*, vol. 6, pp. 13 231–13 260, 2017. DOI: 10.1109/ACCESS.2017.2741578.

- [126] E. Rakhshani, D. Remon, A. M. Cantarellas, H. Mehrjerdi, and P. Rodriguez, "Derivative based inertia emulation of interconnected systems considering phase-locked loop dynamics," in *IEEE Power and Energy Society General Meeting*, 2016. DOI: 10.1109/PESGM.2016.7741705.
- [127] S. D'Arco, J. A. Suul, and O. B. Fosso, "Control system tuning and stability analysis of Virtual Synchronous Machines," in *IEEE Energy Conversion Congress and Exposition*, 2013, pp. 2664–2671. DOI: 10.1109/ECCE.2013.6647045.
- [128] U. Tamrakar, D. Shrestha, M. Maharjan, B. P. Bhattarai, T. M. Hansen, and R. Tonkoski, "Virtual inertia: Current trends and future directions," *Applied Sciences (Switzerland)*, vol. 7, no. 7, p. 654, 2017. DOI: 10.3390/app7070654. [Online]. Available: <http://www.mdpi.com/2076-3417/7/7/654>.
- [129] T. Kerdphol, F. S. Rahman, M. Watanabe, and Y. Mitani, "Robust Virtual Inertia Control of a Low Inertia Microgrid Considering Frequency Measurement Effects," *IEEE Access*, vol. 7, pp. 57 550–57 560, 2019. DOI: 10.1109/ACCESS.2019.2913042.
- [130] H. R. Chamorro, I. Riaño, R. Gerndt, I. Zelinka, F. Gonzalez-Longatt, and V. K. Sood, "Synthetic inertia control based on fuzzy adaptive differential evolution," *International Journal of Electrical Power and Energy Systems*, vol. 105, pp. 803–813, 2019. DOI: 10.1016/j.ijepes.2018.09.009.
- [131] A. S. Mir and N. Senroy, "Self-Tuning Neural Predictive Control Scheme for Ultrabattery to Emulate a Virtual Synchronous Machine in Autonomous Power Systems," *IEEE Transactions on Neural Networks and Learning Systems*, vol. 31, no. 1, pp. 136–147, 2020. DOI: 10.1109/TNNLS.2019.2899904.
- [132] A. Ulbig, T. Rinke, S. Chatzivasileiadis, and G. Andersson, "Predictive control for real-time frequency regulation and rotational inertia provision in power systems," in *Proceedings of the IEEE Conference on Decision and Control*, 2013, pp. 2946–2953. DOI: 10.1109/CDC.2013.6760331.
- [133] U. Markovic, N. Früh, P. Aristidou, and G. Hug, "Interval-based adaptive inertia and damping control of a virtual synchronous machine," in *IEEE Milan PowerTech*, 2019. DOI: 10.1109/PTC.2019.8810640.
- [134] X. Hou, Y. Sun, X. Zhang, J. Lu, P. Wang, and J. M. Guerrero, "Improvement of Frequency Regulation in VSG-Based AC Microgrid Via Adaptive Virtual Inertia," *IEEE Transactions on Power Electronics*, vol. 35, no. 2, pp. 1589–1602, 2020. DOI: 10.1109/TPEL.2019.2923734.
- [135] G. Grimm, M. J. Messina, S. E. Tuna, and A. R. Teel, "Model predictive control: For want of a local control Lyapunov function, all is not lost," *IEEE Transactions on Automatic Control*, vol. 50, no. 5, pp. 546–558, 2005.

- [136] U. Tamrakar, D. Shrestha, N. Malla, Z. Ni, T. M. Hansen, I. Tamrakar, and R. Tonkoski, “Comparative analysis of current control techniques to support virtual inertia applications,” *Applied Sciences (Switzerland)*, vol. 8, no. 12, 2018. DOI: 10.3390/app8122695.
- [137] H. Bock, M. Diehl, D. Leineweber, and J. Schlöder, “A direct multiple shooting method for real-time optimization of nonlinear dae processes,” in *Nonlinear model predictive control*, Springer, 2000, pp. 245–267.
- [138] M. Diehl, H. G. Bock, J. P. Schlöder, R. Findeisen, Z. Nagy, and F. Allgöwer, “Real-time optimization and nonlinear model predictive control of processes governed by differential-algebraic equations,” *Journal of Process Control*, vol. 12, no. 4, pp. 577–585, 2002.
- [139] R. Quirynen, M. Vukov, M. Zanon, and M. Diehl, “Autogenerating microsecond solvers for nonlinear mpc: A tutorial using acado integrators,” *Optimal Control Applications and Methods*, vol. 36, no. 5, pp. 685–704, 2015.
- [140] K. Geebelen, M. Vukov, M. Zanon, S. Gros, A. Wagner, M. Diehl, D. Vandepitte, J. Swevers, and H. Ahmad, “An experimental test setup for advanced estimation and control of an airbornewind energy system,” in *Airborne wind energy*, Springer, 2013, pp. 459–471.
- [141] T. Kraus, H. J. Ferreau, E. Kayacan, H. Ramon, J. De Baerdemaeker, M. Diehl, and W. Saeys, “Moving horizon estimation and nonlinear model predictive control for autonomous agricultural vehicles,” *Computers and electronics in agriculture*, vol. 98, pp. 25–33, 2013.
- [142] M. Vukov, W. Van Loock, B. Houska, H. J. Ferreau, J. Swevers, and M. Diehl, “Experimental validation of nonlinear mpc on an overhead crane using automatic code generation,” in *American Control Conference (ACC)*, 2012, pp. 6264–6269.

LIST OF PUBLICATIONS DURING PH.D. STUDY

Journals

1. U. Tamrakar, D. A. Copp, T. Nguyen, T. M. Hansen, and R. Tonkoski, "Optimization-based Fast-Frequency Estimation and Control of Low-Inertia Microgrids," *IEEE Transactions on Energy Conversion*, under review, 2020.
2. U. Tamrakar, D. A. Copp, T. Nguyen, T. M. Hansen, and R. Tonkoski, "Online Moving Horizon Estimation of Inertia and Damping Constant of Microgrids," *IEEE Access*, to be submitted, 2020.
3. U. Tamrakar, D. Shrestha, N. Malla, Z. Ni, T. M. Hansen, I. Tamrakar, and R. Tonkoski, "Comparative Analysis of Current Control Techniques to Support Virtual Inertia Applications," *Applied Sciences*, vol. 8, no. 7, pp. 2695, December 2018.
4. U. Tamrakar, D. Shrestha, M. Maharjan, B. P. Bhattarai, T. M. Hansen, and R. Tonkoski, "Virtual Inertia: Current Trends and Future Directions," *Applied Sciences: Advances in Integrated Energy Systems Design, Control and Optimization*, vol. 7, no. 7, pp. 654, June 2017.
5. M. Farrokhbadi, C. A. Canizares, U. Tamrakar, et al., "Microgrid Stability Definitions, Analysis, and Examples," *IEEE Transactions of Power Systems*, 2019.
6. H. Sun, Q. Guo, J. Qi, U. Tamrakar, et al., "Review of Challenges and Research Opportunities for Voltage Control in Smart Grids," *IEEE Transactions of Power Systems*, 2019.
7. B. Shrestha, U. Tamrakar, D. Shrestha, T. M. Hansen, B. P. Bhattarai, S. James, and R. Tonkoski, "Efficiency and Reliability Analyses of AC and 380 V DC Distribution in Data Centers," *IEEE Access*, vol. 6, pp. 63305-63315, 2018.
8. N. Malla, U. Tamrakar, D. Shrestha, Z. Ni and R. Tonkoski, "Online Learning Control for Harmonics Reduction based on Current Controlled Voltage Source Power Inverters," *IEEE/CAA Journal of Automatica Sinica*, vol. 4, no. 3, pp. 447-457, 2017.

Conferences

1. U. Tamrakar, N. Guruwacharya, N. Bhujel, F. Wilches-Bernal, T. M. Hansen and R. Tonkoski, "Model Predictive Frequency Control of Low Inertia Microgrids," in *IEEE Symposium on Power Electronics, Electrical Drives, Automation and Motion (SPEEDAM)*, Sorrento, Italy, 6 pages, accepted 2020, to appear.
2. U. Tamrakar, T. M. Hansen, D. Copp, and R. Tonkoski, "Model Predictive Frequency Control of Low Inertia Microgrids," in *28th IEEE International Symposium on Industrial Electronics*, Vancouver, BC, Canada, June 2019.

3. U. Tamrakar, F. B. dos Reis, A. Luna, D. Shrestha, R. Fournay, and R. Tonkoski, "Virtual Inertia Emulation using Commercial Off-The-Shelf Inverters," in *IEEE Energy Conversion Congress and Exposition (ECCE)*, Portland, OR, USA, Sept., 2018.
4. U. Tamrakar, N. Malla, D. Shrestha, Z. Ni and R. Tonkoski, "Design of Online Supplementary Adaptive Dynamic Programming for Current Control in Power Electronic Systems," in *IEEE Energy Conversion Congress and Expo (ECCE)*, Cincinnati, Ohio, USA, Oct., 2017.
5. U. Tamrakar, E. Laursen, M. Maharjan, S. Gent and R. Tonkoski, "Modeling of Photo-bioreactors for Remote Microgrids," in *IEEE Electro-Information Technology Conference*, Grand Forks, ND, USA, May, 2016.
6. N. Guruwacharya, N. Bhujel, U. Tamrakar, M. Rauniyar, S. Subedi, S. E. Berg, T. M. Hansen and R. Tonkoski, "Data-Driven Power Electronic Converter Modeling for Low Inertia Power System Dynamic Studies," in *IEEE Power and Energy Society General Meeting*, Montreal, Canada, 5 pages, accepted 2020, to appear.
7. A. Ingalalli, U. Tamrakar, T. M. Hansen, and R. Tonkoski, "Modeling Hydro Power System Frequency Dynamics for Virtual Inertia Emulation," in *28th IEEE International Symposium on Industrial Electronics*, Vancouver, BC, Canada, June, 2019 (**Received the Best Paper Award**).
8. A. Luna, U. Tamrakar, T. M. Hansen, and R. Tonkoski, "Frequency Response in Grids with High Penetration of Renewable Energy Sources," in *IEEE North American Power Symposium (NAPS)*, Fargo, ND, USA, Sept. 2018.
9. M. Ullah, S. Chalise, U. Tamrakar, and R. Tonkoski, "Impact of Battery Operating Conditions on Remote Microgrid's Energy Management System," in *IEEE Power & Energy Society General Meeting (PESGM)*, Portland, OR, USA, Aug., 2018.
10. P. Tandukar, L. Bajracharya, T. M. Hansen, R. Fournay, U. Tamrakar, and R. Tonkoski, "Real-time Operation of a Data Center as Virtual Power Plant Considering Battery Lifetime," in *International Symposium on Power Electronics, Electrical Drives, Automation and Motion (SPEEDAM)*, Amalfi, Italy, June, 2018.
11. P. Adhikari, S. Prajapati, I. Tamrakar, U. Tamrakar and R. Tonkoski, "Parallel Operation of Virtual Synchronous Machines with Frequency Droop Control," in *IEEE International Conference in Power Systems*, Pune, India, December, 2017.
12. M. Maharjan, P. Tandukar, A. Bajracharya, F.B. dos Reis, U. Tamrakar, D. Shrestha, F.S. dos Reis and R. Tonkoski, "SEPIC Converter with Wide Bandgap Semiconductor for PV Battery Charger," in *IEEE Brazilian Power Electronics Conference (COBEP)*, Juiz de Fora, Brazil, Nov., 2017.
13. M. Maharjan, U. Tamrakar, S. Bajagain, T. M. Hansen and R. Tonkoski, "A Steady-State Equivalent Model of Solid State Transformers for Voltage Regulation Studies," in *IEEE PES General Meeting*, Chicago, IL, USA, July, 2017.

14. M. Maharjan, U. Tamrakar, N. Malla, F.B. Reis, Z. Ni, T. M. Hansen and R. Tonkoski, "Adaptive Droop-Based Active Power Curtailment Method for Over-voltage Prevention in Low Voltage Distribution Network," in *IEEE International Conference on Electro-Information Technology (EIT)*, Lincoln, NE, USA, May, 2017.
15. D. Shrestha, U. Tamrakar, Z. Ni and R. Tonkoski, "Experimental Verification of Virtual Inertia in Diesel Generator based Microgrids," in *18th IEEE International Conference on Industrial Technology (ICIT)*, Toronto, Canada, Mar., 2017 **(Received the Best Paper Award)**.
16. D. Shrestha, U. Tamrakar, N. Malla, Z. Ni and R. Tonkoski, "Reduction of Energy Consumption of Virtual Synchronous Machine using Supplementary Adaptive Dynamic Programming," in *IEEE Electro Information Technology Conference*, Grand Forks, ND, USA, May, 2016.
17. H. Atia, A. Shakya, P. Tandukar, U. Tamrakar, T.M. Hansen and R. Tonkoski, "Efficiency Analysis of AC Coupled and DC Coupled Microgrids Considering Load Profile Variations," in *IEEE Electro-Information Technology Conference*, Grand Forks, ND, USA, May, 2016.